STRONG FIELD INTERACTIONS WITH ATOMS AND MOLECULES

SUSANA ARIAS LASO

A DISSERTATION SUBMITTED TO
THE FACULTY OF GRADUATE STUDIES
IN PARTIAL FULFILLMENT OF THE REQUIREMENTS
FOR THE DEGREE OF
DOCTOR OF PHILOSOPHY

GRADUATE PROGRAM IN PHYSICS AND ASTRONOMY
YORK UNIVERSITY
TORONTO, ONTARIO

April 2022

Abstract

Atoms and molecules exposed to strong fields of magnitude comparable to their internal binding forces undergo ionization. This process sets the ground for multiple strong-field ionization phenomena such as above threshold ionization (ATI). This dissertation addresses two separate ionization problems, the dc Stark ionization of H_2O valence orbitals, $1b_1$, $1b_2$, and $3a_1$, within the framework of non-Hermitian quantum mechanics, and ATI for a model-helium atom as part of a review of a previous quantitative approach based on the strong-field approximation (SFA).

Calculations of the dc ionization parameters, dc Stark shift and exponential decay rates, for the H_2O valence orbitals are carried out by solving the Schrödinger equation in the complex domain. Two independent models are implemented in the study of static ionization of the molecular orbitals (MOs). In the first one, a spherical effective potential obtained from a self-consistent calculation of H_2O orbital energies is combined with an exterior complex scaling approach to express the problem as a system of partial differential equations that is solved numerically using a finite-element method. In the second approach, a model potential for the H_2O molecule is expanded in a basis of spherical harmonics and combined with a complex absorbing potential that results in a complex eigenvalue problem for the Stark resonances.

The second part of this investigation is concerned with the study of ATI for atoms subjected to a strong laser field. The convergence of the ionization spectrum for a model-helium atom is addressed in a systematic study that is carried out following Keldysh's formalism of SFA. A generalized compact expression for the ionization amplitude that incorporates electron rescattering into the analysis is explored as well. Additionally, a model based on the concept of quantum paths is implemented in the numerical evaluation of the SFA transition amplitude. In this analysis, a coherent sum over all allowed quantum trajectories that render the action stationary is carried out. This calculation allows to generate an ATI spectrum that converges to the numerical Keldysh amplitude as the number of trajectories increases.

Contents

List of Tables

List of Figures

List of Abbreviations

ATI: above-threshold ionization

SFA: strong-field approximation

MO: molecular orbital

TDSE: time-dependent Schrödinger equation

SCF: self-consistent field

HF: Hartree-Fock

CC: coupled-clusters

CS: complex scaling

CAP: complex absorbing potential

ECS: exterior complex scaling

PDE: partial differential equation

AP: antisymmetrized product

MSO: molecular spin-orbital

LCAO: linear combination of atomic orbitals

STO: Slater-type orbital

NHQM: non-Hermitian quantum mechanics

DFT: density functional theory

OPM: optimized potential method

KFR: Keldysh-Faisal-Reiss

HHG: high-harmonic generation

1 Introduction

Atomic and molecular systems exposed to strong external fields have been explored extensively. The H_2O molecule, which is of interest in this work, has served as a reference for nonlinear molecules under strong external fields and has received considerable attention in ion-molecule collision studies (see [9, 10] and references therein) due to its relevance in applied fields, such as radiation therapy. The multicentre nature of its potential makes the water molecule an attractive and challenging problem, and diverse approximations have been implemented in order to learn about its molecular structure as well as its interaction with external perturbations such as strong dc fields and high-intensity laser fields [11–15].

High-intensity laser-atom interactions are the origin of phenomena such as ATI, which reveals that an atom may absorb many more photons than the minimum necessary for ionization [16]. Under the effect of an intense laser field, an atom that is initially in its ground state gets ionized at some given time followed by the ejection of an electron that interacts with the laser field once it is promoted to the continuum and eventually rescatters to within the vicinity of the binding potential as the external field changes direction. As a consequence of this interaction, an ATI spectrum consisting of a sequence of peaks separated by the photon energy is generated. The study of this spectrum has been of increased interest as it reveals features that describe the mechanism of interaction of an atom with an external field [17, 18].

Events of strong dc field ionization of the water molecule valence orbitals and laser-induced ionization of atoms constitute the essence of this work. This study involves deriving an effective potential that reproduces the symmetry properties of each MO as an initial step in the calculation of the Stark resonance parameters for the water molecule under an external static electric field. The interaction of a strong laser field with atoms, in particular, the phenomenon of ATI is addressed within a framework that allows to uncover the underlying physics without having to

resort to computationally demanding tools such as solving the time-dependent Schrödinger equation (TDSE). A generalization of the SFA [19] is implemented within two independent frameworks for the case of a zero-range potential: a semi-classical approach involving quantum paths [20] and a numerical evaluation of the exact SFA results [21].

Since the work of Ellison and Shull [22], numerous theoretical studies that attempt to formulate an accurate description of the H_2O molecule have been reported. The self-consistent field (SCF) method introduced by Roothaan [23], which allows to represent the Hartree-Fock (HF) orbitals of a molecule as expansions of basis functions, has been widely implemented in the study of the ground state and symmetry properties of H_2O. Within the SCF framework, the MOs have been approximated using multicentre Slater-type atomic orbitals as basis sets [24–27], as well as Gaussian basis functions [28, 29].

Additionally, one-centre expansions were applied in order to bypass the difficulty of evaluating multicentre integrals [1, 30, 31]. However, inherent to this method is the additional difficulty of needing a more extensive set of basis functions. As an example, Moccia introduced an expansion of the H_2O MOs in terms of Slater-type functions all centred at the nucleus of the oxygen atom [1]. This work, in which the author determined the expansion coefficients of a linear combination consisting of 28 Slater-like functions by means of Roothaan's SCF method, obtained wave functions that led to remarkably accurate values for the total energy of the ground state configuration of H_2O.

Solving the TDSE in the study of static-field ionization rates could perhaps seem like a logical effort that leads to highly accurate solutions. This approach has been implemented, within the framework of Hermitian quantum mechanics, in tunnelling calculations for the helium atom [32, 33] in which the two-electron Schrödinger equation was solved and the results were in good agreement with previous calculations [34]. However, obtaining a numerical solution to the many-body TDSE, corresponding to molecular Stark resonances, remains a challenging problem even for a small number of particles.

Time-independent approaches, which make use of a non-Hermitian formulation of quantum mechanics by means of a complex-variable representation of the molecular Hamiltonian, have established useful alternatives in the study of molecular static-field ionization. Within a complex-variable framework, the Stark resonance parameters induced by an external field are associated

with a discrete set of complex eigenvalues. Among the proposed methods, coupled-cluster (cc) calculations of molecular strong-field ionization provided accurate results for the Stark and static-field ionization rates of several molecules [11]. In this work, the author combined cc methods [35] with complex basis functions, consisting of basis sets of atom-centred Gaussian functions with a complex-scaled exponent, and computed molecular Stark resonances linked to complex eigen-states of H_2O for different orientations of the external dc field.

Among alternative well-established methods to compute resonance states are those of complex scaling (cs) [36] and complex absorbing potentials (caps) [37] in which the Hamiltonian is extended analytically into the complex plane by an artificial local potential formulated to absorb the diverging tail of the resonance wave functions at the boundaries of a finite volume. The resonance parameters are then obtained from the square-integrable eigenfunctions of the modified non-Hermitian Hamiltonian with absorbing boundary conditions. Extensions of these methods, such as the exterior complex scaling (ecs) [38], have been introduced in studies of ionization of molecular structures [39, 40], and to determine numerical solutions of the tdse for strong-field-induced dynamics in atoms and molecules [41–43].

A modified exterior complex scaling approach in which the radial coordinates are gradually continued into the complex plane, the method implemented in the current work, is introduced with the aim of studying the field-ionization properties of the H_2O valence orbitals. This method permitted to formulate the problem of H_2O static-field ionization as a system of partial differential equations (pde) in which the Stark resonance parameters were obtained via the complex eigenenergies of the pde system. This work led to two referenced publications [44, 45].

In what follows, the topic of strong-field laser-atom interactions is addressed. Numerous formulations have been introduced which aim to understand the physics behind the complicated structure of the ati spectrum. The Keldysh theory of strong-field approximation is one of the pioneering works that properly accounts for tunnelling ionization [19], and produces accurate electron spectra for ati for relatively low energies. However, the sfa in its early versions failed to provide a comprehensive description of the ionization spectrum, in particular, to account for the extended plateau at higher energies that was first observed in [7] for the ati spectrum of rare gases in strong laser pulses.

Extensions of the Keldysh theory have provided a deeper understanding of laser-atom inter-

actions and revealed the underlying mechanism that gives origin to the ATI plateau: rescattering. In order to incorporate rescattering events, subsequent models needed to allow the freed electron to interact once more with the ion. A semiclassical three-step model which incorporates the effect of rescattering, in which the atomic potential is considered a perturbation while the electron propagates in the laser field, [46, 47] was successful in revealing the complicated angular distributions of the ATI spectrum. Additional attempts that incorporate rescattering in the context of the Keldysh approach were implemented by means of Coulomb-Volkov solutions [48].

An interesting interpretation of the laser-atom interactions is the one offered by the path-integral formulation of quantum mechanics [49]. The concept of a quantum path that connects the initial and final state of a system, and combines the tunnelling of an electron with its subsequent semiclassical propagation in the laser field, has been used to explain subtle features of ATI [50]. In addition, incorporating the path-integral principles within the framework of SFA calculations, has allowed to successfully reproduce the structure of ATI spectra that can be connected with interferences of the contributions of a finite number of quantum trajectories [20].

This dissertation addresses two separate topics, the static-field ionization of the H_2O molecule and the phenomenon of ATI within the framework of an extended SFA. Chapter 2 presents the necessary background of the HF formulation that sets the basis for the SCF calculation of the H_2O orbital energies [1] used as reference in the study of the water molecule under the effect of an external field. Chapter 3 contains two independent studies of the dc field ionization of the H_2O valence orbitals, $1b_1$, $1b_2$, and $3a_1$ within the framework of non-Hermitian quantum mechanics (NHQM). A modified exterior complex scaling and a complex absorbing potential combined with a partial-wave expansion of a previous model potential are implemented. The topic of laser-atom interactions is approached in Chapters 4 and 5. Chapter 4 contains a study of convergence of the ATI spectrum associated with an improved Keldysh model [21] within the limits of a zero-range potential in which events of direct ionization and ionization with rescattering are treated separately. A saddle-point approximation is implemented in Chapter 5 to the problem of evaluating the ATI spectrum of a model-helium atom in a strong laser field in terms of quantum orbits. Finally, conclusions of this work are presented in Chapter 6.

Atomic units ($\hbar = m = -e = 4\pi\epsilon_0 = 1$) are used throughout unless otherwise indicated.

2 Electronic Structure of H_2O

This chapter presents a brief compilation of the principles of the HF formulation implemented in problems of molecular quantum mechanics. Section 2.1 summarizes the Roothaan formulation of the HF formalism, in which the HF orbitals are expressed as linear combinations of suitable analytical functions [23]. For molecules, the calculation of electronic wave functions is more intricate than for atoms since it is preferable to use basis functions centred about several nuclei, which implies the difficult task of evaluating multicentre integrals [26, 27]. Sec. 2.2 describes a different approach that consists of using a set of basis functions all referred to one common origin and has reported satisfactory results in calculations of SCF molecular orbitals for AH_n-type molecules [1, 51].

2.1 Variational Hartree-Fock method

As a starting point in the SCF MO calculations, the $N-$electron HF wave function for a molecule is written as the antisymmetrized product (AP) of N one-electron wave functions [23]. A molecular spin-orbital (MSO) which factors into a molecular orbital, φ, and a spinor, η, that depends on the space and spin coordinates of the μth electron can be defined as

$$\psi_k^\mu \quad = \quad \varphi_{i(k)}(x^\mu, y^\mu, z^\mu)\eta_k(s^\mu), \tag{2.1}$$

where the superscript μ stands for the coordinates of the μth electron and the subscripts k and i label the different MSOs and MOs, respectively,

The total N-electron wave function is then built up as an AP of N molecular spin-orbitals of

the form (2.1) [23]

$$\Phi = \sqrt{N!}\psi_1^{[1}\psi_2^{2} \cdots \psi_N^{N]} = (N!)^{-1/2} \begin{vmatrix} \psi_1^1 & \psi_2^1 & \cdots & \psi_N^1 \\ \psi_1^2 & \psi_2^2 & \cdots & \psi_N^2 \\ \cdots & \cdots & \cdots & \cdots \\ \psi_1^N & \psi_2^N & \cdots & \psi_N^N \end{vmatrix}, \tag{2.2}$$

where the superscripts $[1\ 2 \cdots N]$ indicate that one must consider all the permutations of the sequence $1\ 2 \cdots N$ such that the Pauli exclusion principle is satisfied, that is, each MO φ_i^μ may occur not more than twice (corresponding to opposite spin projections) in the AP (2.2). The right-hand side of Eq. (2.2) is a Slater determinant of MSOs that is constructed by taking an antisymmetric linear combination of products of spin-orbitals.

For a closed-shell structure, in which the AP (2.2) is made up of complete electron shells, the HF method seeks the MO's that minimize the variational energy [23]

$$E = 2\sum_i h_i + \sum_i \sum_j (2J_{ij} - K_{ij}). \tag{2.3}$$

The first sum in Eq. (2.3) represents the energy of all the electrons in the field of the nuclei alone, where h_i are the nuclear-field orbital energies [23]. The remaining sum contains the electronic interactions, in which the Coulomb integrals J_{ij} and exchange integrals K_{ij} are defined by

$$J_{ij} = \int \frac{\bar\varphi_i^\mu \bar\varphi_j^\nu \varphi_i^\mu \varphi_j^\nu}{r^{\mu\nu}} dv^{\mu\nu} \tag{2.4a}$$

$$K_{ij} = \int \frac{\bar\varphi_i^\mu \bar\varphi_j^\nu \varphi_j^\mu \varphi_i^\nu}{r^{\mu\nu}} dv^{\mu\nu}, \tag{2.4b}$$

where the integration goes over the spatial coordinates of the μth and the νth electron.

The HF SCF method looks for those molecular orbitals φ_i that minimize the variational energy (2.3). In an iterative process, the molecular orbitals that form the AP (2.2) are corrected by an infinitesimal amount $\delta\varphi_i$, that along with the requirement that the molecular orbitals continue to form an orthonormal basis, leads to express the variation of the energy as [23]

$$\delta E = 2\sum_i \int (\delta\bar\varphi_i)\{H + \sum_j (2J_j - K_j)\}\varphi_i dv + 2\sum_i \int (\delta\varphi_i)\{\bar H + \sum_j (2\bar J_j - \bar K_j)\}\bar\varphi_i dv, \tag{2.5}$$

where $H = -\frac{1}{2}\nabla^2 - \sum_\alpha \frac{1}{r^\alpha}$ is the Hamiltonian that represents the field of the nuclei alone. The operators J_j and K_j represent the Coulomb operator and exchange operator, respectively, and

are defined as [23]

$$J_i^\mu \varphi^\mu = \left(\int \frac{\bar{\varphi}_i^\nu \varphi_i^\nu}{r^{\mu\nu}} dv^\nu \right) \varphi^\mu \tag{2.6a}$$

$$K_i^\mu \varphi^\mu = \left(\int \frac{\bar{\varphi}_i^\nu \varphi^\nu}{r^{\mu\nu}} dv^\nu \right) \varphi_i^\mu. \tag{2.6b}$$

The Coulomb operator represents the potential energy operator associated to an electron distributed in space with a density $|\varphi_i|^2$. On the other hand, the exchange operator has no classical analog. The notation $\bar{U}$ is used to represent the complex conjugate of the operator U.

In order for the energy (2.3) to reach its absolute minimum, the condition $\delta E = 0$ must be satisfied for any choice of MOs that form an orthonormal basis. This condition can be expressed as [23, 52]

$$\{H + \sum_j (2J_j - K_j)\}\varphi_i = \sum_j \varphi_j \epsilon_{ji}, \tag{2.7}$$

where ϵ_{ji} are the elements of a Hermitian matrix obtained in the variational procedure of minimizing the energy (2.3) [23]. Once an initial guess for the occupied MOs has been introduced, the orbital energies ϵ_i can be obtained as the energy eigenvalues of the Fock operator, F, that satisfies

$$F = H + \sum_j [2J_j - K_j]. \tag{2.8}$$

Consequently, the HF SCF problem can be addressed as the problem of finding the best set of MOs that satisfy [23, 52]

$$F\varphi_i = \sum_j \varphi_j \epsilon_{ji}. \tag{2.9}$$

Without loss of generality, Eq. (2.9) can be expressed as the eigenvalue problem

$$F\varphi_i = \epsilon_i \varphi_i, \tag{2.10}$$

where ϵ_i are the real elements of a diagonal matrix, which results from applying a unitary transformation to the Hermitian matrix ϵ_{ji}. The set of Eqs. (2.10), commonly known as HF equations, states that the eigenfunctions of the Hermitian operator F are the set of MOs that give the best AP, while the eigenvalues ϵ_i represent the HF orbital energies [23].

The formalism introduced by Roothaan [23], that allows the Hartree-Fock-Roothaan orbitals to be expressed as linear combinations of suitable analytical functions, represents a crucial development in obtaining accurate numerical results that approximate the true HF wave functions

of the water molecule, as well as predicting chemical properties in addition to the binding energy of its ground state [22, 27, 29, 53, 54]. This approach introduces a representation of the MOs by means of a linear combination of atomic orbitals (LCAO) [23]

$$\varphi_i = \sum_{s=1}^{b} c_{si} \chi_s. \tag{2.11}$$

Given that the sum (2.11) is an approximation to the exact HF MOs, the AP built from these MOs would be a less good approximation to the exact AP built from the HF MOs. In order for the linear combination (2.11) to be an exact representation of a HF MO, the basis functions χ_s should form a complete set. However, in practice one is limited to a finite (and therefore incomplete) basis set. The number of basis functions, b, as well as the proper choice of basis functions χ_s are essential in order to obtain MOs that resemble the HF MOs with very small error [1, 51, 55].

The problem of obtaining the best set of MOs for a closed-shell ground state consists in finding the set of coefficients c_{si} for which the energy of the associated AP reaches its absolute minimum. The LCAO SCF procedure begins with an initial guess for the linear combination of basis functions (2.11). This initial set is used to compute the Fock operator from equations (2.8) to (2.6b). The matrix elements F_{rs}

$$F_{rs} \equiv \langle \chi_r | F | \chi_s \rangle \tag{2.12}$$

are then evaluated in order to determine the nontrivial solutions of the set of b simultaneous linear equations of the form

$$\sum_{s=1}^{b} c_{si}(F_{rs} - \epsilon_i S_{rs}) = 0, \quad r = 1, 2, \ldots, b$$

$$S_{rs} \equiv \langle \chi_r | \chi_s \rangle, \tag{2.13}$$

that results from inserting the expansion (2.11) into the HF equations (2.10), and represents a linear algebra generalized eigenvalue problem, in which the eigenvalues ϵ_i and linear coefficients c_{si} are to be obtained. The eigenvalues of Eq. (2.13), which are the roots of the secular equation [23, 52]

$$\det(F_{rs} - \epsilon_i S_{rs}) = 0, \tag{2.14}$$

form an initial set of LCAO orbital energies that leads to a set of coefficients c_{si} and, consequently, MOs.

In the process of solving the set of equations (2.10) one looks for the MOs φ_i that minimize the variational energy (2.3). Initially, one infers a set of coefficients c_{si}, and, consequently, MOs of the form (2.11), that are used to compute the Fock operator F and solve the secular equation (2.14) to obtain an initial set of orbital energies ϵ_i, which in turn is used to obtain an improved set of coefficients by solving the eigenvalue problem (2.13). This procedure to minimize the energy is set up carefully as an iteration until the MO coefficients converge according to an established norm and no further improvement is observed from one evaluation to the next.

The LCAO SCF formalism is an approximation that leads to rather straightforward results for the MOs. This model leads to accurate approximations of the HF SCF wave function provided the basis set (2.11) is large enough [1, 22, 51, 55]. Taking things further to achieve a complete description of the true HF wave function is a much more complicated mathematical problem.

2.2 Self-Consistent Field Slater Orbitals

A frequently used set of basis functions in atomic and molecular HF calculations, in order to represent molecular wave functions as linear combinations of analytical functions, is the set of Slater-type orbitals (STOs) of the form

$$f_{n,l,m}(\zeta; r, \theta, \phi) = \frac{(2\zeta)^{n+\frac{1}{2}}}{[(2n)!]^{\frac{1}{2}}} r^{n-1} e^{-\zeta r} S_{l,m}(\theta, \phi), \tag{2.15}$$

where n, l, and m are integers indicating a basis function, while the nonlinear variational parameter ζ satisfies $\zeta \in \Re > 0$. The angular part $S_{l,m}(\theta, \phi)$ represents real spherical harmonics.

In order to converge to an exact representation of the HF orbitals, it would be necessary to include a rather large basis of STOs in an expansion of the form (2.11). However, previous calculations indicate that it is possible to obtain highly accurate results by choosing conveniently optimized basis of STOs to represent atomic orbitals [56–58] and molecular orbitals [1, 51, 55].

The formalism implemented by Moccia to study the ground state of XH_n molecules [1, 51, 55] develops the previously introduced method of using electronic wave functions expressed by a one-centre expansion with the centre at the X nucleus [30, 31]. This approach, labeled as SCF one-centre-expanded molecular orbitals [51], permits to evaluate the ground state along with the vibrational spectrum of this type of molecules for a given geometrical arrange.

Following the Roothaan formalism described in Sec. 2.1, the initial wave function is expressed

as an AP of molecular spin-orbitals in which each MO is built as a linear combination of Slater-type orbitals (STOs) of the form (2.15). The orbital exponents ζ_i corresponding to each basis set were obtained by means of an optimization process closely connected with finding the geometrical equilibrium configuration of the molecule [1, 51]. Returning to the linear expansion for the i-th MO φ_i introduced in Roothaan's formalism, Eq. (2.11) can be expressed in terms of Slater-type orbitals as follows

$$\varphi_i(\zeta, r, \theta, \phi) = \sum_{s=1}^{b} c_{si} f_{s_{n,l,m}}(\zeta_{si}, r, \theta, \phi), \qquad (2.16)$$

where the expansion coefficients c_{si} are evaluated within a self-consistent procedure in order to minimize the electronic energy. The sets of (n, l, m) values indicate the size and orbital symmetries of the basis set implemented for a given molecule.

The SCF calculations for the ground state of H_2O, in which the expansion centre was located upon the oxygen nucleus [1], explored different combinations of symmetries and n values in order to obtain the best possible linear combination available from a basis set of the form (2.15). Table I in [1] shows the converged numerical results including the geometrical parameters of the equilibrium configuration for the ground state of H_2O. It emerged from these calculations, in which the basis parameter n was fixed at values as high as 4, that very large values of n are not needed in order to obtain rather accurate results since the converged wave functions obtained for the MOs could not be dramatically improved by simply changing the nonlinear parameters of the STOs, ζ_i, (2.15). Rather, a careful selection of an initial set for the nonlinear variational parameters ζ_i for a moderate number of basis functions indicated to be crucial for improving the radial behaviour of the wave functions for a given symmetry.

As an initial step in the one-centre SCF iterative process implemented by Moccia [1, 51, 55], some parameters are provided as input data. The basis functions that are identified by the three integers n, l, m in Eq. (2.15) and by the orbital exponents ζ, as well as an estimate of the expansion coefficients, c_{si}, of the MOs are among these quantities. The process of variation of the nonlinear parameter ζ reveals a strong correlation with the geometrical equilibrium configuration of the molecule. The numerical results of the one-centre basis SCF method were obtained by modifying the basis sets (2.11) implementing a variational method and determining the geometrical configuration that minimizes the total energy for each set of ζ's. The final results, indicated in

Table I [1] for the H$_2$O molecule, correspond to the geometrical configuration that provides the lowest total energy among the different sets considered.

Other studies have addressed the problem of the electronic structure of H$_2$O within the HF SCF scheme using multicentre basis functions, and achieved satisfactory total energies that approach the converged HF energies rather well. Total energies of -75.776 a.u. and -75.741 a.u. are quoted in Refs. [24] and [25], respectively, using Roothan-type SCF basis functions. A compilation of SCF results that employ multicentre basis sets in HF calculations of the ground state of some polyatomic molecules can be found in Ref. [59]. Additionally, a series of SCF calculations in a Gaussian basis [28] reported a total energy of -76.0421 a.u. for H$_2$O. Many of these calculations, however, used extensive sets of basis functions or more complicated forms of wave functions. More advanced calculations of the H$_2$O wave functions, in which an increasing number of multicentre s, p, and d STOs was used as basis sets, were successful in calculating physical properties, such as the electric dipole moment and force constants, in good agreement with experiment [26, 27].

3 H$_2$O in an external electric dc field

The Stark resonance parameters, which characterize the shift and decay width of the molecular energy levels under an external dc field, are fundamental in the study of the strong dc field ionization of MOs. In the case of the water molecule, the multicentre nature of the combined Coulomb interactions and, consequently, the additional degrees of freedom as compared to atoms, make the strong dc field ionization of H$_2$O an attractive and challenging problem from the point of view of a theoretical description. Complex variable techniques, such as ECS [38, 42] and CAPs [37, 41], have been implemented in order to address the problem of molecular static-field ionization and compute the induced Stark resonances.

The dc Stark problem for the H$_2$O valence orbitals is addressed in this chapter within the framework of non-Hermitian quantum mechanics [60]. Two independent complex variable techniques are implemented in order to modify the divergent outgoing wave functions into the physical domain of square integrable wave functions. A modified ECS, in which the Hamiltonian of the system is gradually rotated into the complex plane to obtain the resonance parameters induced by an external dc field, is the first of these approaches. The construction of a local effective potential, which reflects the individual properties of the orbitals, is crucial in this study. An alternative analysis is based on a quadratic CAP which requires successive calculations of complex eigenvalues along a trajectory that is determined by the strength parameter of the CAP. The CAP method is then combined with a correction scheme in order to eliminate the artifact introduced in the Hamiltonian by the complex absorber.

Section 3.1 introduces some of the fundamental aspects of non-Hermitian quantum mechanics. In Sec. 3.2, we formulate the problem with emphasis on the representation of the MOs. The ECS formalism is introduced in Secs. 3.3 and 3.4 as a crucial step in finding a numerical solution to a spherically symmetric problem, in the case of the $1b_1$ and $1b_2$ orbitals, and the problem of a

non-central effective potential, in the case of the $3a_1$ orbital. Section 3.5 is concerned with the discussion of a partial-wave expansion method implemented for a model potential designed to simulate the structure of the H_2O molecule. The problem of dc-ionization of the H_2O valence orbitals is treated in terms of a CAP. The Stark resonance parameters are then presented in Sec. 3.6, in which the symmetry properties of the orbitals are considered independently. The analysis presented in this chapter compiles that of [44, 45].

3.1 Non-Hermitian quantum mechanics

Resonance phenomena, such as atomic and molecular strong-field ionization events, have been successfully approached within the framework of NHQM [60]. This alternative formulation to the standard formalism of quantum mechanics allows for a time-independent interpretation of strong-field ionization processes and quantitative modelling of the associated ionization rates. This is possible by means of implementing analytic continuation methods on the Hamiltonian, from which the resonance is obtained as a solution with complex eigenvalues of the form

$$E = E_R + iE_I = E_R - i\Gamma/2, \tag{3.1}$$

in which the ionization rate, Γ, induced by the external field F_0 is associated to the lifetime of the decaying state τ via $\Gamma\tau = 1$, while the Stark shift under the external field is given by the difference between the real part of the complex-valued energy and the ground state energy, $E_R - E_0$.

Several numerical techniques have been introduced within the framework of NHQM in studies of atomic and molecular Stark resonances. These approaches implement a complex-scaled Hamiltonian by means of a mapping operator that results in complex eigenvalues and provide direct access to the resonant states of the Stark problem. It is the scope of this work to focus on two of these methods to study the response of the H_2O highest-energy orbitals to an external dc-field, the concept of a CAP introduced as a perturbation to the molecular Hamiltonian and a modified ECS.

A CAP is introduced as an imaginary potential which introduces an analytical continuation of the Hamiltonian to the complex plane. This artificial perturbation of the system acts as an effective absorber potential that suppresses the diverging tail of the resonance wave function in

the vicinity of the edges of a numerical grid. As a result, the solutions of the modified non-Hermitian Hamiltonian behave as square-integrable eigenstates.

In general terms, the application of a CAP begins with the addition of an artificial local potential of the form $-i\eta W(r)$ to the Hamiltonian of the system, where the parameter η indicates the strength of the CAP. The function $W(r)$, which determines the onset of the CAP, has been most commonly defined as a quadratic potential centred at some radius r_c, such that the artificial term to be included in the Hamiltonian takes the form

$$
V_{\text{CAP}} = \begin{cases} -i\eta_c(r - r_c)^2 & \text{when} \quad r > r_c \\ 0 & \text{when} \quad r < r_c \end{cases}.
\tag{3.2}
$$

The CAP approach requires calculating sets of complex eigenvalues which form complex trajectories, $E(\eta_c)$. These trajectories are generated by varying the CAP strength η_c. Subsequently, a correction scheme to extrapolate to $\eta_c = 0$ is carried out in order to obtain the eigenvalues of a complex-scaled Hamiltonian in which the perturbation introduced by the CAP has been removed.

Strategies used to obtain accurate values for the resonance parameters that extrapolate the complex trajectories to the limit of $\eta_c = 0$ include the Padé extrapolation procedure [61], and the Riss-Meyer iterative correction method [37]. Combining such correction schemes with a CAP has proven to yield accurate results for the Stark resonance parameters of diatomic molecules, such as the hydrogen molecular ion in a static electric field [62] and a low-frequency ac field [63].

An alternative method to divert the divergent resonance wave functions into the domain of square integrable solutions is the ECS [38], in which the Hamiltonian is rotated into the complex plane at a boundary of the problem. One applies the coordinate transformation

$$
x = \begin{cases} x' & \text{if} \quad x' < x_0 \\ e^{i\xi}x' & \text{if} \quad x' \geq x_0 \end{cases},
\tag{3.3}
$$

in order to carry out an ECS of the x coordinate at the scaling radius x_0 with scaling angle $\xi < \pi/2$. The application of the complex scaling in an external region, which keeps the coordinates unscaled in some range of the potential, avoids the numerical difficulties that arise when the potential has singularities. This approach, however, imposes explicit discontinuity conditions on the wave function and its derivatives [39]. The method of ECS has proven to be useful in acting as a perfect absorber of the outgoing flux when solving the TDSE with strong laser fields [42]. The

14

implementation of a smooth ECS to the radial coordinates of an orbital-dependent Hamiltonian that represents the H_2O valence orbitals is one of the motivations of the current chapter.

3.2 Molecular orbital representation of H_2O

The starting point for this study is the HF calculation of the H_2O molecular states using a single-center Slater orbital basis [1, 51, 55], applied to collision studies [64] and compared to experimental electron spectroscopy [65]. Accurate descriptions of the molecular structure of H_2O have been obtained by means of the variational HF method using multicentre Slater orbitals as basis functions [26, 27]. However, the direct application of these multicentre orbitals for strong-field studies implies significant computational and methodological challenges. The experimental ionization energies of H_2O can be deduced from photoelectron spectroscopy, but they are complicated by vibrational level structures and are significantly broadened; quoted values for the three valence orbitals correspond to ionization energies of $0.68, 0.54, 0.46$ for $1b_2, 3a_1, 1b_1$, respectively [66].

The present work is intended to study the valence MOs of H_2O, $1b_1$, $1b_2$ and $3a_1$. The wave functions for the $1b_1$ and $1b_2$ MOs, which can be approximated as the $2p_x$ and $2p_y$ oxygen orbitals, are dominated by a single angular momentum symmetry. The $3a_1$ MO, on the other hand, consists mainly of the oxygen $2s$ and $2p_z$ and the hydrogen $1s$ atomic orbitals.

The general expression for the basis functions, introduced as a set of single-center wave functions [1, 51, 55], is a Slater-type orbital as defined in Eq. (2.15). The expansion coefficients and nonlinear coefficients $\{\zeta_i\}$, determined by Roothaan's SCF method [1, 23] introduced in Sec. 2.2, are used to construct a reduced form of the radial functions that describe all the molecular orbitals. More specifically, we are interested in using a reduced STO expansion to construct an effective potential that describes an H_2O bound state as a first step in studying the response of the H_2O valence orbitals when applying an electric dc field along the symmetry axis (i.e., the $z-$axis). For the study shown in this chapter, the external dc field is oriented in the molecular plane, which coincides with the $y - z$ plane. Both geometries are considered, the field pointing away from the oxygen atom along the centre line passing in between the two hydrogen atoms, $F_0 > 0$, and the reverse orientation, $F_0 < 0$.

Based on their symmetry properties, independent descriptions of the valence MOs of H_2O

are constructed. The dominant components of the $1b_1$ and $1b_2$ orbitals, namely the np_x and np_y parts, are used to derive spherically symmetric effective orbital-dependent potentials [44]. A similar procedure is implemented for the $3a_1$ orbital, in which the np_z parts of the MO are retained. Additionally, the strong asymmetry introduced by the two protons located in the $y - z$ plane is incorporated in the analysis by including STOs of type $2s$ and $2p_z$ in the orbital expansion for the $3a_1$ MO. This extended STO expansion leads to a non-spherical effective potential that contains the significant admixtures of $s-$type Slater orbitals in the Moccia STO expansion [1].

3.3 $1b_1$ and $1b_2$ molecular orbitals

The Schrödinger equation for the bound-state problem of a MO within an effective potential $V_{\text{eff}}(r)$ is expressed in spherical polar coordinates as

$$[-\frac{1}{2}(\frac{\partial^2}{\partial r^2} + \frac{2}{r}\frac{\partial}{\partial r}) + \frac{\hat{L}^2}{2r^2} + V_{\text{eff}}(r)]\Psi(r,\theta,\varphi) \;\; = \;\; E\Psi(r,\theta,\varphi), \qquad (3.4)$$

where $\hat{L}^2$ is the orbital quantum momentum operator. The present study involves the construction of the effective orbital-dependent potential, $V_{\text{eff}}(r)$, extracted from the single-centre Moccia wave functions [1]. This is followed by the implementation of an ECS [38] to determine the numerical solution of the problem associated with a MO in the presence of a strong electric dc field applied along the $\hat{z}-$direction [44]. A schematic representation of the geometry of the system is shown in Figure 3.1, where the orientation of the $1b_1$ and $1b_2$ MOs is indicated with respect to the plane where the protons are located. The direction of the applied electric field along $\hat{z}$ is included as well.

As a first step in solving Eq. (3.4) for the H_2O MOs, we introduce the reduced single-centre Moccia wave function,

$$\psi_n(r) = \sum_i c_n(\zeta_i)f_n(\zeta_i, r), \qquad (3.5)$$

which approximates the MO by an eigenstate of a spherically symmetric potential. The functions $f_n(\zeta_i, r)$ represent the radial part of the Slater orbitals (2.15) with $|m| = 1$ for the magnetic quantum number, in which the STO expansion is limited to $2p_x$ and $2p_y$ orbitals, respectively. The set of expansion coefficients and non-linear coefficients in (3.5), indicated in Table 3.1, represents a reduced selection of the expansion parameters given by Moccia for the ground state of the water molecule [1].

16
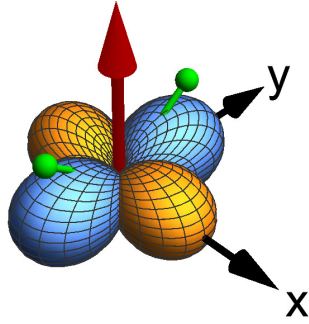
Figure 3.1: Schematic display of the $1b_1 \approx 2p_x$ (shown in yellow along the x axis) and $1b_2 \approx 2p_y$ (shown in blue along the y axis) MOs. Also indicated (in green on the $y - z$ plane) is the location of the protons. The z axis (in red) is the direction of the external electric field of strength F_0. As indicated in the text, positive values of F_0 correspond to the external field pointing from the oxygen towards the hydrogen atoms; negative values of F_0 correspond to a field pointing from the hydrogen atoms towards the oxygen atom.

In order to determine the effective potential corresponding to each MO, the wave function (3.5) is inserted into the single-electron Schrödinger equation (3.4), which is then solved for $V_{\text{eff}}^{(1)}(r)$. Afterwards, the so-called Latter correction [44, 67] is applied to ensure that the effective potential converges asymptotically to $-1/r$, as expected in a Coulomb potential:

$$
V_{\text{eff}}(r) = \begin{cases} V_{\text{eff}}^{(1)}(r) \text{ for } r < r_0 \\ -1/r \text{ for } r > r_0 \end{cases}, \tag{3.6}
$$

where the point r_0 is determined from $V_{\text{eff}}^{(1)}(r_0) = -1/r_0$, and is found to be sufficiently large that the original SCF orbital energy used to derive $V_{\text{eff}}^{(1)}(r)$ is close to the eigenenergy of (3.4), with at least two significant digits of agreement, with $V_{\text{eff}}(r)$ given by (3.6).

Figure 3.2 shows a comparison of the effective potential $V_{\text{eff}}^{(1)}(r)$ (solid lines), with black representing the $1b_1$ MO and blue representing the $1b_2$ MO, derived from the Moccia wave functions representing the $1b_1$ and $1b_2$ MOs [1], and the transformed electronic potential $V_{\text{eff}}(r)$ (dashed lines) after the Latter correction was implemented. The effective potentials for the $1b_1$ and $1b_2$ MOs are given as the shallower and deeper curves, respectively. As Figure 3.2 illustrates, one drawback of the method is that the effective potential is orbital dependent. A direct consequence

17
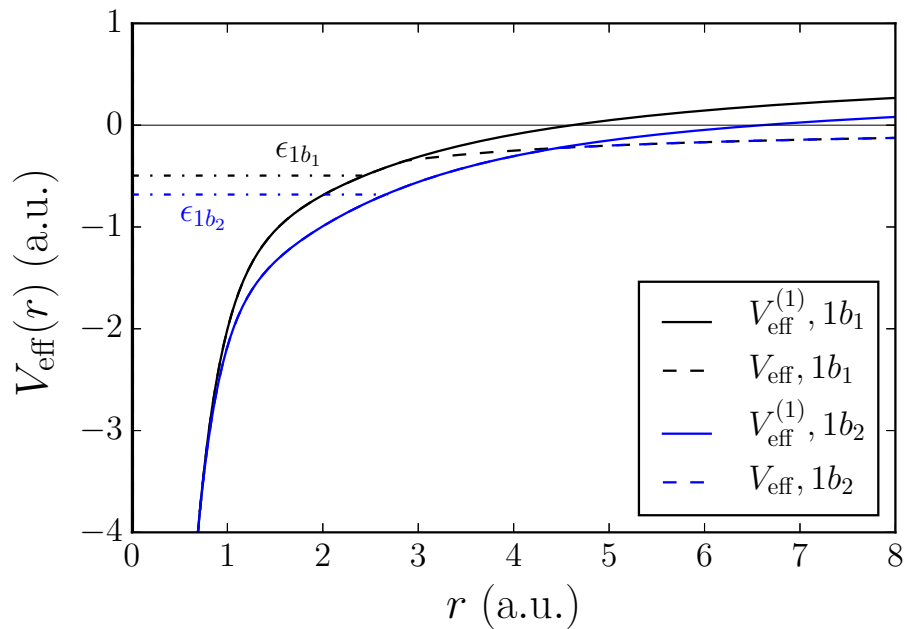
Figure 3.2: Electronic effective potential in atomic units for the $1b_1 \approx 2p_x$ (black) and $1b_2 \approx 2p_y$ (blue) MOs of the H_2O molecule. The solid lines give the potential as derived from (3.4) using the SCF orbitals and eigenenergies, while the dashed lines show the potentials after the Latter correction is applied. The dot-dashed lines indicate the eigenenergies obtained from the Moccia wave functions [1].

Table 3.1: Expansion coefficients and nonlinear coefficients for the $1b_1$ and $1b_2$ MOs of H_2O. The parameters used in our reduced STO expansion are indicated as included.

(n,l,m)		ζ_i	$c_{nlm}^{1b_1}$	$c_{nlm}^{1b_2}$
$(2,1,1)$	included	1.510	0.72081	–
$(2,1,1)$	included	2.440	0.11532	–
$(2,1,1)$	included	3.920	0.24859	–
$(3,2,1)$	excluded	1.600	0.05473	–
$(3,2,1)$	excluded	2.400	0.00403	–
$(4,3,1)$	excluded	1.950	0.00935	–
$(4,3,3)$	excluded	1.950	-0.02691	–
$(2,1,-1)$	included	1.510	–	0.88270
$(2,1,-1)$	included	2.440	–	-0.07083
$(2,1,-1)$	included	3.920	–	0.23189
$(3,2,-1)$	excluded	1.600	–	0.25445
$(3,2,-1)$	excluded	2.400	–	-0.01985
$(4,3,-1)$	excluded	1.950	–	0.04526
$(4,3,-3)$	excluded	1.950	–	-0.06381

is that the value of $r = r_0$, which sets the position in r where the Coulombic tail is imposed, differs between the MOs, being almost two times larger for the $1b_2$ compared to the $1b_1$ MO.

3.3.1 PDE approach and exterior complex scaling

This section discusses further the formalism implemented to calculate the relevant resonance parameters in the problem of the H_2O molecule exposed to a strong dc field. Having obtained an effective potential to define the field-free Schrödinger equation (3.4) for an orbital obtained in the SCF method [1], we proceed with the problem of the molecule ionized by a strong dc field.

When an electric field is applied in the $\hat{z}$ direction, $\mathbf{F} = F_0\hat{z}$, the separation of variables

ansatz as applied to the Schrödinger equation (3.4)

$$\Psi(r, \theta, \varphi) = \Psi(r, \theta) \exp(im\varphi) \tag{3.7}$$

leads to a PDE in spherical coordinates that represents the Stark problem for an H_2O orbital:

$$-\frac{1}{2}\frac{\partial^2 \Psi}{\partial r^2} - \frac{1}{2r^2}\left(\frac{\cos\theta}{\sin\theta}\frac{\partial \Psi}{\partial \theta} + \frac{\partial^2 \Psi}{\partial \theta^2}\right) + \left(\frac{m^2}{2r^2\sin^2\theta} + V_{\text{eff}}(r) - E + F_0 r\cos\theta\right)\Psi = 0. \tag{3.8}$$

Here the complex eigenenergy E contains the information about the resonance position (real part), i.e., E_R and width Γ (imaginary part is $-\Gamma/2$) as indicated in Eq. (3.1). For the $1b_1$ and $1b_2$ MOs, which are formulated as linear combinations of $2p_x$ and $2p_y$ orbitals, respectively, we have $|m| = 1$ in Eq. (3.8). The presence of the effective potential $V_{\text{eff}}(r)$ makes this problem challenging in the sense that it is not possible to obtain separable solutions like for the hydrogen atom in which a pure Coulomb potential leads to separability in parabolic coordinates, as was discussed in [2]. It is then necessary to generate a more general solution by solving the PDE numerically, e.g., by applying a finite-element method.

The ionization regime of the water molecule is described by means of a non-Hermitian Hamiltonian that reveals discrete resonance eigenvalues containing information about the quasibound states that tunnel through the barrier or escape over the potential barrier for strong fields. Among the different techniques implemented in the study of atomic resonances, a standard tool is the method of complex scaling [36, 68, 69] introduced in Chapter 1.

For most phenomenological potentials, such as molecules with fixed internuclear distances, a modified method of scaling is required as an extension to cases where the potential is analytic only outside some bounded region. In these cases, the approach of ECS [38] is more appropriate, as the potential needs to have analyticity properties only in the region affected by the scaling, where one can look for solutions which decay exponentially in the asymptotic region of the potential. Approaches of complex scaling have been widely used in scattering problems [36, 69], in studies of the Stark problem for multi-electron systems [39, 40], as well as in TDSE problems for strong fields [42, 43, 70].

For our aim of studying the field ionization properties of H_2O orbitals, we implement a modified ECS technique in which the radial coordinates are extended into the complex plane by a phase factor, which is turned on gradually beyond some distance from the origin. This method allows us to address the tunnelling and over-barrier ionization problem by avoiding the
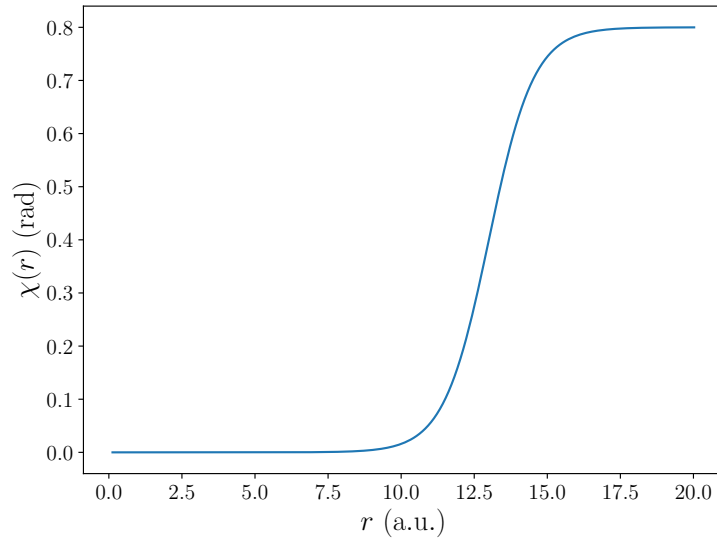
Figure 3.3: Scaling function corresponding to $\chi_{\mathrm{s}} = 0.8$ rad, $r_{\mathrm{s}} = 13$ a.u., and $1/\Delta r = 1.3$ a.u.

complication of describing quasibound states with outgoing waves for $r \to \infty$. In the present work, the complex scaling transformation is given by

$$r \to \quad r \exp(i\chi(r)), \tag{3.9}$$

where χ is defined as a function of the r coordinate with the purpose of making the scaling gradually effective from some vicinity of $r = r_{\mathrm{s}}$ on,

$$\chi(r) = \quad \frac{\chi_{\mathrm{s}}}{1 + \exp[-\frac{1}{\Delta r}(r - r_{\mathrm{s}})]}. \tag{3.10}$$

For given r_{s} one has to choose Δr to be sufficiently small, so that the function $\chi(r)$ starts from small values at $r = 0$. For large r, it converges to the value χ_{s}. Figure 3.3 illustrates the scaling function $\chi(r)$ that corresponds to the set of $(\chi_{\mathrm{s}}, r_{\mathrm{s}}, \Delta r)$ values used in the numerical calculations of the dc Stark parameters for the H_2O valence orbitals.

The set of possible values for the asymptotic scaling angle χ_{s} and the parameters r_{s} and Δr, which control where and how quickly the scaling is turned on, is explored in detail in order to establish how sensitive the PDE solutions are and to test the effectiveness of the complex scaling technique to absorb the outgoing wave. Numerous tests were carried out to ensure

21

that the numerically "exact" results of Telnov [2] for atomic hydrogen orbitals including $2p$ are reproduced.

In order to investigate the effects of the dc field on the H_2O orbital energies it is necessary to consider the extra terms that the ECS (3.9) introduces in the Schrödinger equation (3.8). Additionally, we need to turn the scaling on only in the regime $r > r_0$, as Eq. (3.6) indicates, such that we have a simple Coulomb potential in the scaling region. In order to make use of standard finite-element methods, the complex-valued wave function is separated into real and imaginary parts, such that a system of coupled differential equations is obtained as follows [44]:

$$
\begin{aligned}
-\frac{1}{2}\frac{\partial^2 \Psi_R}{\partial r^2} - \frac{1}{2r^2}\Big(\frac{\cos\theta}{\sin\theta}\frac{\partial \Psi_R}{\partial \theta} + \frac{\partial^2 \Psi_R}{\partial \theta^2}\Big) & \\
+\Big(\frac{m^2}{2r^2\sin^2\theta} + V_{\text{eff}}^R(r)c_2 - V_{\text{eff}}^I(r)s_2 - E_R c_2 + E_I s_2 + F_0 r\cos\theta c_3\Big)\Psi_R & \\
+(-V_{\text{eff}}^R(r)s_2 - V_{\text{eff}}^I(r)c_2 + E_R s_2 + E_I c_2 - F_0 r\cos\theta s_3)\Psi_I &= 0, \\
-\frac{1}{2}\frac{\partial^2 \Psi_I}{\partial r^2} - \frac{1}{2r^2}\Big(\frac{\cos\theta}{\sin\theta}\frac{\partial \Psi_I}{\partial \theta} + \frac{\partial^2 \Psi_I}{\partial \theta^2}\Big) & \\
+\Big(\frac{m^2}{2r^2\sin^2\theta} + V_{\text{eff}}^R(r)c_2 - V_{\text{eff}}^I(r)s_2 - E_R c_2 + E_I s_2 + F_0 r\cos\theta c_3\Big)\Psi_I & \\
+(V_{\text{eff}}^R(r)s_2 + V_{\text{eff}}^I(r)c_2 - E_R s_2 - E_I c_2 + F_0 r\cos\theta s_3)\Psi_R &= 0. \quad (3.11)
\end{aligned}
$$

The labels R and I stand for real and imaginary parts, respectively; also, the notation $[c_k, s_k]$ is introduced to represent $[\cos[k\chi(r)], \sin[k\chi(r)]]$, respectively, with $k = 2, 3$ and $\chi(r)$ defined in (3.10). Note that the effective potential has real and imaginary parts on account of the coordinate transformation (3.9).

The PDE system (3.11) is solved numerically on a rectangular mesh defined by the (r, θ) coordinates, which take values in the domains $\epsilon < r < r_{\text{max}}$ and $\eta < \theta < \pi - \eta$, respectively. The parameters ϵ and η, that limit the coordinate ranges to avoid singularities at the origin, were chosen to be of the order of 10^{-3} a.u., and the r coordinate extends to $r_{\text{max}} = 20$ a.u. In order to find a correct set of $\Psi_{R(I)}(r, \theta)$ solutions, it is essential to impose proper boundary conditions that ensure the wave functions vanish at the limits of the mesh. For the $|m| = 1$ states we impose the condition $\Psi_{R(I)}(\epsilon, \theta) = \epsilon\sin(\theta) = \epsilon P_1^1(\theta)$, which is consistent with the assumption that at small $r = \epsilon$ the lowest term in an expansion in associated Legendre polynomials dominates and behaves like $Ar^2\sin(\theta)$.

A two-parameter root search for $\{E_R, E_I\}$ is implemented by solving the PDE as if it were an

22

inhomogeneous problem. We pick a location in the (r, θ) plane where the probability amplitude is expected to be large and vary $\{E_R, E_I\}$, i.e., effectively the complex energy E to maximize the amplitude.

3.4 $3a_1$ molecular orbital

In this section we extend the approach to study the dc Stark problem for the $3a_1$ MO of H_2O. Given the orientation of this orbital with respect to the plane in which the two protons are located it is deemed necessary to go beyond the spherical effective potential approximation, which was implemented in Sec. 3.3 for the $1b_1$ and $1b_2$ orbitals, in order to take into account the strong asymmetry introduced by the protons in the $y-z$ plane and the significant admixtures of $s-$type Slater orbitals in the STOs [1].

The proposed method to address this problem is to define a reduced single-centre Moccia wave function,

$$\Psi_{3a_1}(r, \theta) = \sum_{n,l} c_{nl0} \varphi_{nl}(r, \theta). \tag{3.12}$$

Here the $\varphi_{nl}(r, \theta)$ are Slater orbitals with $m = 0$ for the magnetic quantum number, and we limited the expansion to STOs of $2s$ and $2p_z$ type. The parameters are given in Table 3.2 and three $2p_z$ orbitals are mixed with three $2s$-type orbitals. This set of coefficients represents a reduced selection of the expansion parameters given by Moccia for the ground state of the water molecule [1] also shown in Table 3.2.

The probability densities for the $3a_1$ orbital as obtained from the reduced expansion (3.12) and from the Moccia self-consistent results are shown in Figures 3.4a and 3.4b, respectively. The protons (in red) lie in the $y - z$ plane. As Fig. 3.4a indicates, the contributions to the density of the $2s-$type states reproduce the proper dependence of the $3a_1$ probability density with the polar angle θ, as the broader hump is located on the negative $z-$axis in the same way as in the complete Moccia representation shown in Fig. 3.4b.

In order to illustrate the fraction of the full Moccia expansion that our reduced wave function (3.12) represents, the projections of the probability densities over the $x - y$ plane are shown as contours of constant density in Figure 3.5, for the height where the protons are located. From the complete Moccia representation of the $3a_1$ MO (in dashed lines), one observes that the loca-

23

Table 3.2: Expansion coefficients and non-linear coefficients for the $3a_1$ MO. The parameters used in our reduced STO expansion are indicated as included.

(n, l, m)		c_{nlm}	ζ_i
$(1, 0, 0)$	excluded	-0.00848	12.600
$(1, 0, 0)$	excluded	0.08241	7.450
$(2, 1, 0)$	included	0.79979	1.510
$(2, 1, 0)$	included	0.00483	2.440
$(2, 1, 0)$	included	0.24413	3.920
$(2, 0, 0)$	included	-0.30752	2.200
$(2, 0, 0)$	included	-0.04132	3.240
$(2, 0, 0)$	included	0.14954	1.280
$(3, 2, 0)$	excluded	0.05935	1.600
$(3, 2, 0)$	excluded	0.00396	2.400
$(3, 2, 2)$	excluded	-0.09293	1.600
$(3, 2, 2)$	excluded	0.01706	2.400
$(4, 3, 0)$	excluded	-0.01929	1.950
$(4, 3, 2)$	excluded	-0.06593	1.950

tion of the protons (shown as red circles) has an influence on the shape of the upper lobe in the probability density, i.e., it introduces dependence on the azimuthal angle φ. In our simplified expansion, where only $l = 0, 1$ and $m = 0$ parts were included (shown with solid lines), the probability density misses to represent the proper azimuthal dependence that follows from the $m \neq 0$ parts.

The non-spherical effective potential corresponding to the STO expansion (3.12), $V_{\text{eff}}(r, \theta)$, is obtained from the Schrödinger equation in spherical polar coordinates,

$$\left[-\frac{1}{2} \nabla^2 + V_{\text{eff}}(r, \theta) \right] \Psi_{3a_1}(r, \theta) = E_{3a_1} \Psi_{3a_1}(r, \theta). \tag{3.13}$$

For given E_{3a_1} and $\psi_{3a_1}(r, \theta)$, an effective potential $V_{\text{eff}}(r, \theta)$ can be constructed from Eq. (3.13) as described in Sec. 3.4.1. In order to use this potential to define a Hamiltonian for the $3a_1$

(a) Simplified $3a_1$ orbital   (b) Full Moccia $3a_1$ orbital
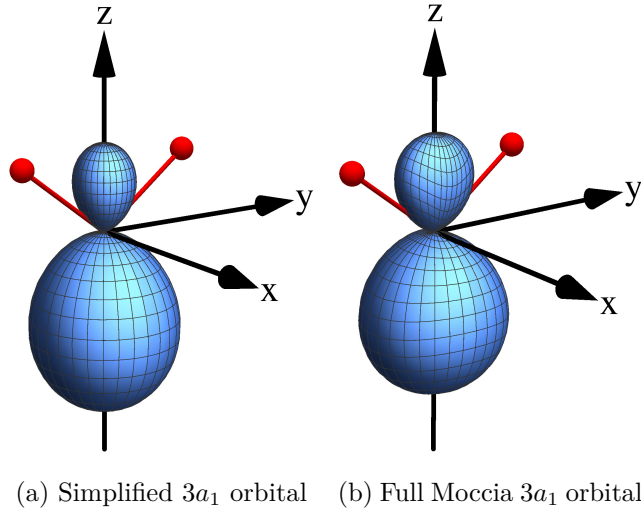
Figure 3.4: Schematic display of the $3a_1$ MO (shown in blue along the z axis) used to construct $V_{\text{eff}}(r, \theta)$. The orbital obtained from a reduced expansion in STOs is shown in (3.4a), and the complete Moccia orbital is shown in (3.4b). Also indicated (in red in the $y - z$ plane) is the location of the protons. The $\hat{z}-$axis is the direction along which the external electric field of strength F_0 is applied.

orbital in an electric field, an asymptotic Latter correction needs to be applied.

Other strategies for finding an effective potential could be pursued, such as using a density functional, inserting the Moccia wave function, and then performing an azimuthal angle average. Ultimately, one would like to extend density functional theory (DFT) from finding ground-state energies to obtaining resonance positions and widths. This might be feasible using a combination of time-dependent DFT and Floquet theory. Floquet formalism provides a solution for the periodically time-dependent Hamiltonian of a system that interacts with an external electromagnetic field. The solution to the TDSE is formulated in terms of stationary states by means of a Fourier expansion, which obey a system of time-independent coupled differential equations [63, 71]. The goal of the present work is more modest: we calculate the response of an isolated MO in a simple approximation. Recently, the problem of small molecules in a dc field has revealed the effect of electron-electron interactions on Stark resonance parameters [40]. It will be interesting to observe such effects for the water molecule in future work.
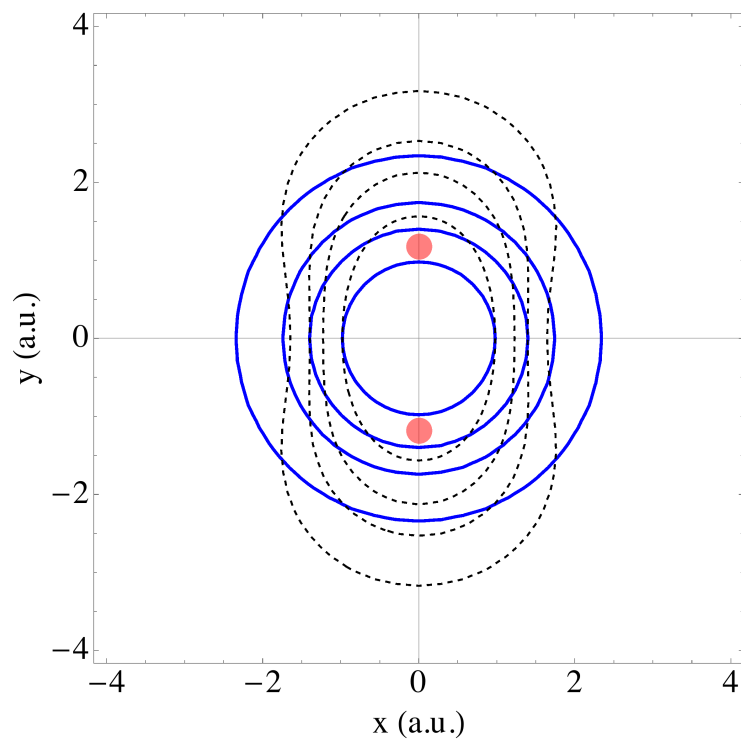
Figure 3.5: Projections of the probability densities for the $3a_1$ orbital on the $x-y$ plane. The simplified STO expansion is shown by continuous blue lines, and the full Moccia expansion is represented by black dashed lines. The proton locations are indicated as red circles. The chosen contour values are $0.5, 0.3, 0.2, 0.1$ starting from the innermost contour.

3.4.1 Interpolation and Latter correction of the non-spherical effective potential

The non-central effective potential, $V_{\text{eff}}(r,\theta)$, leads no longer to an orbital of (l,m) symmetry for the case of the $3a_1$ orbital. This reflects the geometry of the problem as a consequence of the location of the protons. The use of this more general potential implies that the so-called Latter criterion [67], which ensures the proper asymptotic behaviour of the potential, $V(r) \to -1/r$ as $r \to \infty$, is not as straightforward to implement as in the case of the spherical potential discussed in Sec. 3.3, where the correction applies beyond a determined r value [44]. In this case, the correction must be implemented in the $r - \theta$ plane, by defining a $\theta-$dependent boundary beyond which the potential obtained from (3.13) rises above $-1/r$ in the asymptotic region [45].

The θ coordinate is fixed at two extreme positions, such as $\theta = 0$ and $\theta = \pi$, in order to find the corresponding r values r_0 and r_π, for which $V_{\text{eff}}(r,\theta) = -1/r$ is satisfied, then we interpolate between them by introducing the $\theta-$dependent function

$$r_{\text{match}}(\theta) \;\; = \;\; \bar{r} - (r_\pi - \bar{r})\cos\theta, \tag{3.14}$$

where $\bar{r} = (r_0 + r_\pi)/2$. With this approach we redefine the effective potential to be the non-central potential derived from the reduced Moccia wave function using Equation (3.13) when $r < r_{\text{match}}(\theta)$, and $-1/r$ otherwise.

The weighted functions used to construct the Moccia orbitals [1] imply a potential difficulty in our problem. Since these functions are not exact solutions of the Schrödinger equation but were obtained from the variational principle by implementing a self-consistent calculation [51], there may be regions in the (r,θ) domain where $\Psi_{3a_1}(r,\theta)$ vanishes, whereas its second derivative remains finite; this produces a nodal line in the electronic potential. Thus, finding a potential for which our approximate wave function satisfies a Schrödinger equation represents an intricate problem.

It turns out that the nodal region is so narrow that when solving the Schrödinger equation the kinetic energy term dominates and it is possible to obtain a solution that remains close to that obtained by the HF method [1], regardless of the fact that there is a region where the effective potential might diverge.

The probability density exhibits two humps indicating the positions of the protons, which is consistent with Figure 3.4, and the effects of the mixing with the $s-$state. One may argue
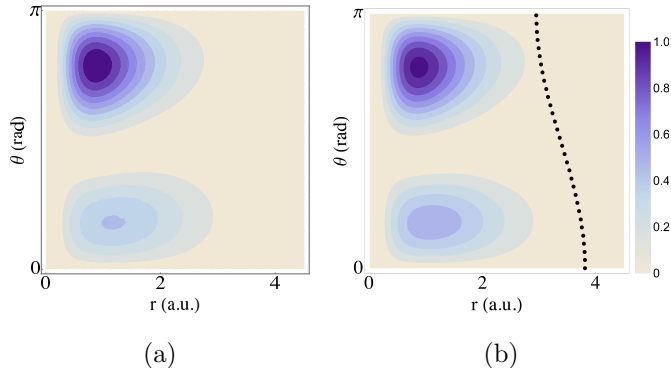
Figure 3.6: Contour plots of the scaled probability density, $|\Psi_{3a_1}|^2 r^2 \sin(\theta)/(2\pi)$, for the $3a_1$ MO. The orbital density constructed from the reduced STO expansion is shown in (3.6a), while the solution obtained from the non-spherical $V_{\text{eff}}(r, \theta)$ with Latter correction is shown in (3.6b) along with a dotted line indicating where the Latter correction acts. Starting from the innermost contours the contour values are $0.45 \ldots 0.05$ for the upper density lobes and $0.2 \ldots 0.05$ for the lower density lobes, in steps of 0.05.

that one of the reasons this nodal region in the potential does not have a negative impact on the results is due to the way the $3a_1$ orbital responds to the effective potential by avoiding this region, its probability density being distributed as shown in Figure 3.6. A numerical interpolation of $V_{\text{eff}}(r, \theta)$ is implemented in order to ensure it continues smoothly over this problematic region.

The interpolation is achieved by collecting data from the evaluation of the potential on two sections of the (r, θ) grid in the vicinity of the nodal line, where the potential takes on finite values. Then, a numerical interpolation was carried out between those regions in order to obtain a continuous function, $V_{\text{eff}}^{\text{intp}}(r, \theta)$, on the two-dimensional grid. The Latter correction is applied to the interpolated potential and the effective potential is defined as

$$V_{\text{eff}}(r, \theta) = \begin{cases} V_{\text{eff}}^{\text{intp}}(r, \theta) & \text{for} \quad r < r_{\text{match}}(\theta) \\ -1/r & \text{for} \quad r > r_{\text{match}}(\theta) \end{cases}. \tag{3.15}$$

Figure 3.6a shows the probability density for the $3a_1$ MO as a contour plot in the $r - \theta$ plane as obtained from the reduced Moccia expansion in STOs (3.12). Figure 3.6b shows the same for the solution of the Schrödinger equation (3.13) using the interpolated $V_{\text{eff}}(r, \theta)$, defined in Equation (3.15), with the Latter correction [67] applied in the asymptotic $r-$region.

28

The effective potential (3.15) results in the probability density shown in Figure 3.6b and yields an orbital energy of -0.5579 a.u. for the $3a_1$ MO, with a relative change of 0.32% in comparison with the self-consistent result of Moccia [1] of -0.5561 a.u..

As Figure 3.6b indicates, the implementation of the Latter correction to the orbital-dependent potential obtained from Equation (3.13) introduces a slight re-adjustment of the density, with a somewhat higher probability density in the region $0 < \theta < \pi/2$. The probabilities for finding the electron at $\pi/2 < \theta < \pi$ is 66.2% before the Latter correction is applied (Figure 3.6a) and becomes 63.5% for the case shown in Figure 3.6b.

3.4.2 Exterior complex scaling

For our aim of computing the resonance parameters that describe the tunnelling process, a modified ECS to the radial coordinates was implemented. As was described in Sec. 3.3.1, the $r-$coordinate is extended into the complex plane by the phase function $\chi(r)$, Eq. (3.10), with r replaced by $r^* = r \exp[i\chi(r)]$. The phase function $\chi(r)$ is chosen to be very small for r values smaller than the Latter radius $\bar{r}$. It then turns on from nearly zero to reach an asymptotic value χ_s at $r-$values just outside where the Latter correction is applied, i.e., $r_\mathrm{s} > r_\mathrm{match}$. By means of the phase function $\chi(r)$, we are implementing a smooth exterior scaling [60] in which the transition from a non-scaled region to the scaled region in the complex plane occurs in a gradual fashion. Applying such a smooth scaling is an alternative approach to the exterior scaling, and avoids the numerical difficulties that arise when a discontinuity in the wave function and its derivative need to be defined at the scaling radius [42].

A non-Hermitian Hamiltonian results from considering the additional terms that the modified complex scaling to the radial coordinates introduces in the Schrödinger equation. The complex wave function is separated into real and imaginary parts, $\Psi_{R(I)}$, such that the problem of describing the ionization regime of the $3a_1$ MO under an external dc field applied along the orientation axis of the orbital is expressed in terms of a system of partial differential equations for the real and imaginary parts of $\widetilde{\Psi}(r, \theta)$ in spherical polar coordinates given explicitly as Eq. (3.11). Schematically, the equations are extensions of the field-free Schrödinger equation (3.13) and

$\widetilde{\psi}(r, \theta)$ satisfies [45]

$$\left[-\frac{1}{2} \nabla^2 + V_{\text{eff}}(r, \theta) \pm F_0 z \right] \widetilde{\Psi}(r, \theta) = (E_R - i\Gamma/2) \widetilde{\Psi}(r, \theta), \tag{3.16}$$

where E_R is the resonance position and Γ the width. The $z-$coordinate, in spherical coordinates $z = r \cos \theta$, is also scaled into the complex plane. Compared to Eq. (3.13), the Hamiltonian in Eq. (3.16) contains the interaction with the external field and complex scaling is responsible for the replacement $E_{3a_1} \rightarrow E_R - i\Gamma/2$; while $\widetilde{\Psi}(r, \theta)$ remains square integrable.

The domains of r and θ values are restricted to the intervals $\epsilon < r < r_{\max}$ and $\eta < \theta < \pi - \eta$, with typical values $\epsilon = 10^{-2}$ a.u., $\eta = 10^{-2}$, $r_{\max} = 28$ a.u. In the limit of low field strengths, i.e., $F_0 = 0.05$ a.u., 0.06 a.u., the value of $r_{\max}$ was increased to 40 a.u. in order to ensure the outer turning points lie inside the grid, as the tunnelling barrier extends to larger r.

The problem of finding a solution of the Schrödinger equation for the $3a_1$ MO with contributions of $2s$ and $2p-$type states requires a set of boundary conditions that describes the properties of the orbital on the grid. In contrast with the numerical solutions obtained for the $1b_1$ and $1b_2$ MOs of H_2O [44], Neumann boundary conditions are implemented for the angular coordinate θ in order to obtain an eigenstate and orbital energy consistent with the variational results [1]. This choice of boundary conditions, that the derivative with respect to θ vanishes at the limits of the mesh ($\theta = 0$ and $\theta = \pi$), leads to solutions $\Psi_{R(I)}(r, \theta)$ with a probability density consistent with the $\theta-$dependence of the $3a_1$ orbital, as shown in Figure 3.6.

3.5 Partial-wave method with a complex absorbing potential

The problem of Stark resonances for the H_2O molecule is treated with a partial-wave expansion approach [72] in which the starting point involves a three-centre model potential that was initially introduced to simulate the structure of the water molecule in a study of ion collisions with water molecules [73], and was later used in numerical calculations of the TDSE for proton-water collisions [4]. The field-free problem is addressed as well in a convergence study of the orbital energies for the three H_2O valence orbitals, namely $1b_1, 1b_2$ and $3a_1$, in terms of the partial wave expansion limits. The results are contrasted with a previous calculation that includes the model potential and Gaussian-type basis [4].

The model potential is formulated as a superposition of three spherical potentials, that rep-

resent the oxygen atom, and the two hydrogen atoms of the water molecule at the equilibrium configuration determined by HF calculations [4], it has the form

$$
\begin{aligned}
V_{\text{mod}} =& V_{\text{O}}(r) + V_{\text{H}}(r_1) + V_{\text{H}}(r_2) \\
V_{\text{O}}(r) =& -\frac{8 - N_{\text{O}}}{r} - \frac{N_{\text{O}}}{r}(1 + \alpha_{\text{O}}r)\exp(-2\alpha_{\text{O}}r) \\
V_{\text{H}}(r_j) =& -\frac{1 - N_{\text{H}}}{r_j} - \frac{N_{\text{H}}}{r_j}(1 + \alpha_{\text{H}}r_j)\exp(-2\alpha_{\text{H}}r_j),
\end{aligned}
\tag{3.17}
$$

where $\alpha_{\text{O}} = 1.602$, $\alpha_{\text{H}} = 0.617$ are screening parameters, r_j indicates the electron position relative to either proton $(j = 1, 2)$, and the electron density 'charge parameters' were chosen as $N_{\text{O}} = 7.185$ and $N_{\text{H}} = (9 - N_{\text{O}})/2 = 0.9075$ for three highest occupied MOs of H_2O.

The following ansatz in spherical polar coordinates is introduced for the wave function

$$
\Psi(r, \theta, \phi) = \sum_{l=0}^{l_{\text{max}}} \sum_{m=-l}^{l} \frac{u_{lm}(r)}{r} Y_l^m(\theta, \phi),
\tag{3.18}
$$

where Y_l^m represents the complex-valued spherical harmonics. The numerical problem then consists of obtaining the $u_{lm}(r)$ solutions by solving coupled ordinary differential equations.

The partial-wave expansion approach for the hydrogen potentials is implemented as follows. The potential for one hydrogen atom placed on the $\hat{z}$ axis with distance R_j from the oxygen core, as indicated in the model potential (3.17), is expressed as an expansion in terms of Legendre polynomials, such that for an axially symmetric $O - H$ problem one has [72]

$$
V_{\text{H}}(r_j) \approx \sum_{\lambda=0}^{\lambda_{\text{max}}} V_\lambda(r) P_\lambda(\cos\theta),
\tag{3.19}
$$

where the channel potentials $V_\lambda(r)$ are obtained by projecting $V_{\text{H}}(r_j)$ onto Legendre polynomials. The hydrogen atom is then rotated into the position consistent with the H_2O geometry using the addition theorem for spherical harmonics

$$
P_\lambda(\cos\theta) = \frac{4\pi}{2\lambda + 1} \sum_{\mu=-\lambda}^{\lambda} Y_\lambda^\mu(\hat{r}')\bar{Y}_\lambda^\mu(\hat{r}''),
\tag{3.20}
$$

where $\cos\theta = \hat{r}' \cdot \hat{r}''$. As a result, the hydrogen components of the model potential (3.17) are expressed as partial-wave expansions in (r, θ, ϕ) coordinates. The orientations defined by θ' correspond to one half of the opening angle, 52.2 degrees, for each hydrogen atom, respectively, and the azimuthal angles are $\phi_1' = \pi/2$ and $\phi_2' = 3\pi/2$ in accordance with the geometry described

in [1]. A truncated potential of the form [72]

$$V_{\mathrm{H}}(r,\theta,\phi) = \sum_{\lambda=0}^{\lambda_{\mathrm{max}}} \frac{4\pi}{2\lambda+1} V_\lambda(r) \sum_{\mu=-\lambda}^{\lambda} Y_\lambda^\mu(\theta,\phi)\bar{Y}_\lambda^\mu(\theta',\phi_j) \qquad (3.21)$$

is then obtained for each hydrogen atom.

The partial-wave model potential that results from inserting the expansion (3.21) into the H$_2$O model potential introduced in (3.17) leads to a system of coupled radial equations of the form [72]

$$-\frac{u_{l,m}''(r)}{2} + \frac{l(l+1)}{2r^2} u_{l,m}(r) + V_{\mathrm{O}}(r)u_{l,m}(r) + \sum_{l',m'} R_{l,m}^{l',m'}(r)u_{l',m'}(r) = \varepsilon u_{l,m}(r), \qquad (3.22)$$

in which the matrix elements $R_{l,m}^{l',m'}(r)$ contain the potentials of the hydrogen atoms as partial-wave expansions, and are evaluated by means of Gaunt integrals [72]. The quantum numbers l,m satisfy $l = 0,\ldots,l_{\mathrm{max}}$, and $-l \leq m \leq l$. The reference frame used in this approach places the oxygen atom at the origin of coordinates, hence the oxygen potential in (3.22), $V_{\mathrm{O}}(r)$, represents the spherically symmetric potential introduced in the model potential (3.17).

Once a partial-wave potential has been generated for each hydrogen atom one can proceed to calculate the eigenvalues for the field-free problem. The computation of numerical solutions for the coupled equations for the different (l,m) channels is carried out using *Mathematica*'s NDEigensystem package, which implements a finite-element mesh to represent the coupled ordinary differential equations (3.22).

The $n-$channel problem to obtain the energy eigenvalues is addressed in the following manner: given a set of different initial conditions and a trial energy value, the system of coupled equations (3.22) can generate n independent solutions that are propagated to a given endpoint at large r where one can build a determinant of the solutions that is ultimately minimized in an iterative process to find the optimal combination of solutions that leads to a zero, or small valued, determinant. Ultimately, one wants to find the energy eigenvalue associated to the overall solution that is bound at some outer radius, i.e., that evaluates to zero or a very small value at large r. As the number l_{max} grows, the number of (l,m) channels increases noticeably and the problem of finding a numerical solution to (3.22) becomes more sensitive to propagated errors, it is necessary in theses cases to increase the working precision of the calculations.

The dc-field ionization problem to determine the Stark resonances for the H_2O valence orbitals under an external field applied along the $\hat{z}$-direction is stated by including the external field potential in the Schrödinger equation. The resulting equation takes the form [72]

$$\left[-\frac{1}{2}\nabla^2 + V(r,\theta,\phi) - F_0 r \cos\theta\right] \Psi(r,\theta,\phi) = E\Psi(r,\theta,\phi), \tag{3.23}$$

where $V(r,\theta,\phi)$ is the model potential (3.17) in which the potential for each hydrogen atom is expressed as a truncated expansion of the form (3.21). The energy E is complex-valued as indicated in Eq. (3.1). A quadratic CAP of the form (3.2) is applied to the system of coupled differential equations in order to determine the complex eigenvalues that result from the effect of the external dc field. The Stark problem presents a higher numerical challenge than the field-free one, in this case we are looking for a solution in the complex plane and the determinant to be minimized is a complex number, which implies that the condition of convergence to zero should be applied to its norm.

The radius r_c in (3.2) indicates the beginning of the region where the CAP turns on. In order to avoid oscillating outgoing waves in the numerical solutions, it is a good practice to turn the CAP on at distances where the partial-wave potential (3.21) has reached its simple asymptotic form. This condition is satisfied for $r > 12$ a.u. with great accuracy. The parameter η_c indicates the strength of the CAP. Ideally, the parameter η_c should be a small number in order to have a small artifact introduced to the system of equations. However, it is important to keep in mind that when $\eta_c \to 0$ numerical errors may increase. Ultimately, the artificial term introduced by the CAP needs to be removed from the results in order to obtain the resonance parameters [37].

The complex eigenvalues that result from applying the CAP (3.2) to the system of coupled equations (3.23) are computed according to the following scheme. For a given field strength, F_0, a set of complex eigenvalues is computed for an equidistant mesh of strength parameters, e.g., $\eta_c = n \times 10^{-3}$ for $n = 20, \ldots, 70$. These results are interpolated to a sixth-order polynomial as a function of η_c, and then the optimal η value is calculated according to the Riss-Meyer correction scheme [37], which is implemented up to second order.

According to the Riss-Meyer scheme [37], the effects of the CAP can be removed by means of an iterative correction scheme based on perturbation theory, in which the n-th order corrected

33

energy can be expressed as a truncated Taylor expansion of the form

$$E^{(n)} = \quad E^{(n)}(\tilde{\eta}) = E_{\text{fb}}(\tilde{\eta}) + \sum_{j=1}^{n} \frac{(-\tilde{\eta})^j}{j!} \frac{d^j E_{\text{fb}}}{d\eta^j}\bigg|_{\eta=\tilde{\eta}}, \tag{3.24}$$

where E_{fb} stands for the finite-basis trajectory of eigenvalues obtained on the $\eta-$grid, and $\tilde{\eta}$ is the optimal value of the CAP strength at which the total error of approximating the exact resonance energy is minimal. This optimal value depends on the order of the correction scheme. Assuming that the next higher order corrected energy is a sufficiently good approximation to the exact resonance energy, the condition to determine the optimal $\tilde{\eta}$ can be expressed as [37]

$$\left| \frac{\eta^{n+1}}{(n+1)!} \frac{d^{n+1} E_{\text{fb}}}{d\eta^{n+1}} \right|_{\eta=\tilde{\eta}} = \quad \min, \quad n = 0, 1, 2, 3. \tag{3.25}$$

The nth order Riss-Meyer correction can be interpreted as removal of the artifact provided by the CAP by nth order perturbation theory.

As an illustrative example, the trajectory of complex eigenvalues as a function of the CAP strength for a partial-wave calculation with $l_{\max} = 3$ for the $3a_1$ MO is shown in Figure 3.7 for a field intensity of $F_0 = -0.1$ a.u.. The blue circles indicate the eigenvalues corresponding to the range of η_{c} values $[0.003, \ldots, 0.06]$ of the CAP parameter in steps of $\Delta\eta_{\text{c}} = 10^{-3}$. The results were obtained using *Mathematica*'s NDEigensystem finite-element solver. The trajectory is smooth for larger values of η_{c}, but it shows remarkable variation at small η_{c} (on the left in Fig. 3.7). This demonstrates the above mentioned difficulty in solving the Schrödinger equation when $\eta_{\text{c}} \to 0$.

The stabilization point $(n = 0)$ is shown as a red cross, and the complex energy values at the accumulation points for $n = 1, 2$ of the Riss-Meyer iterative correction scheme (equations (3.24) and 3.25)) are shown as green and magenta crosses, respectively. These $n = 1, 2$ perturbatively corrected energies fall below the curve and are in close proximity to one another. Looking at the trajectory of complex eigenvalues and the locations of the stabilized value $(n = 0)$ as well as the corrected values to first and second order in perturbation theory $(n = 1, 2)$, it can be noticed that the CAP results shown in Figure 3.7 agree up to three significant digits, both in resonance position and width.

34
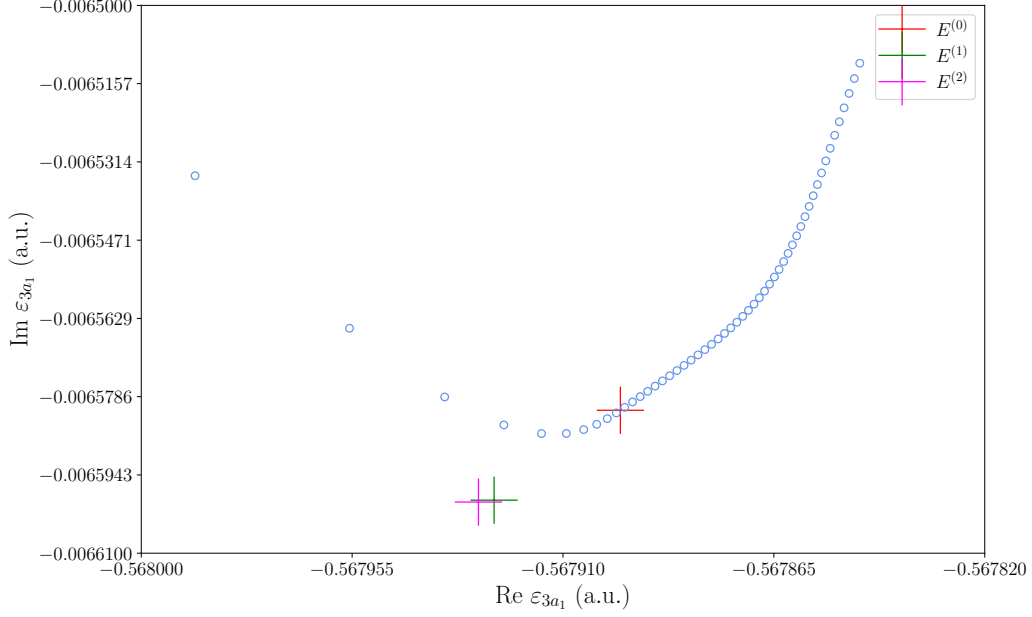
Figure 3.7: Trajectory of complex eigenvalues as a function of η_c (blue circles) corresponding to an $l_{\max} = 3$ calculation of the $3a_1$ MO. The energy corresponding to the η_c stabilization value ($n = 0$ in Eqs. (3.24) and (3.25)) is shown with a red cross. The first and second order Riss-Meyer corrected energies ($n = 1, 2$ in Eqs. (3.24) and (3.25)) are indicated as green and magenta crosses, respectively. The electric field strength is -0.1 a.u.

3.6 Stark resonance parameters

Sections 3.6.1 and 3.6.2 present the numerical results for the physical parameters of interest, namely the resonance position, E_R, and width, $\Gamma = -2E_I$, that characterize the tunnelling process of the quasi-stationary state when an external electric dc field is applied along the $\pm\hat{z}$ directions. The system of partial differential equations (3.11) is solved for a set of field strength values, F_0, as if it were an inhomogeneous problem. In the vicinity of a location in the (r, θ) plane in which the probability amplitude is expected to be large, a two-parameter root search is implemented in order to determine E_R, E_I, the complex energy that maximizes the probability density amplitude in the $2d-$grid.

A study of the influence of a set of numerical parameters involved in the two-dimensional problem (3.11) on the complex eigenvalue $E_R + iE_I$, which describes the ionization process as an exponential decay in time in terms of resonance position and half-width, is carried out. In addition to testing the code against known results for atomic hydrogen [2], a systematic study of the results for the H_2O valence orbitals against a number of parameters is performed in order to assess their accuracy. One parameter concerns the limiting resolution with which the finite-element method proceeds (the MAXCELLSIZE parameter in the *Mathematica* 10 implementation of NDSOLVE, denoted as Δ). For values $\Delta < 0.02$ a.u. we find stability in the eigenvalues (real and imaginary parts) of two-three significant digits. For the results quoted in Secs. 3.6.1 and 3.6.2, the more stringent criterion of $\Delta = 0.01$ a.u. is applied.

The second parameter analyzed in this chapter is the range where the complex scaling function sets in, i.e., r_s and Δr in Eq. (3.10). For the scaling method to work the scaling is required to set in for $r > r_0$, where the effective potential represents a simple Coulomb tail, which in practice is satisfied by $r_s > 2r_0$. Additionally, the condition $\Delta r < 2$ a.u. is needed to guarantee a smooth turn-on of the scaling in this region. Small values of Δr pose challenges for the automated finite-element method, since in the limit of $\Delta r \to 0$ one would need to implement the derivative discontinuity in the solution as discussed by Scrinzi [42]. It has been discussed in the literature that implementing this smooth exterior scaling of the coordinates into the complex plane is equivalent to adding a CAP to the Hamiltonian [74, 75]. We find stable results for the real and imaginary parts of the eigenenergies at the level of three significant digits for the range $10 < r_s < 15$ a.u. Larger values would require an increase in the computational domain beyond
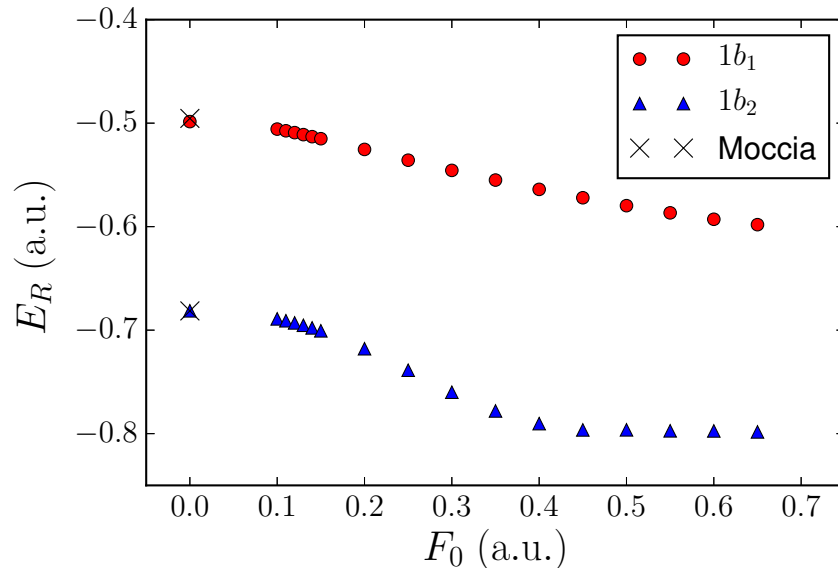
Figure 3.8: Resonance position as a function of the external field strength F_0 for the $1b_1$ (red circles) and $1b_2$ (blue triangles) MOs of H_2O.

$r = 20$ a.u.

Another systematic that is explored is the choice of the ultimate scaling angle reached at large r, namely the value of χ_s in (3.10). For an accuracy demand of three significant digits, and the other parameters chosen in the ranges described above stability in the resonance widths is achieved for $0.6 < \chi_s < 1.2$ rad.

Finally, in Section 3.6.3 we discuss the results of the partial-wave expansion method introduced in Sec. 3.5 for a model potential that simulates the structure of the H_2O molecule [73]. The partial-wave approach is combined with a quadratic CAP in order to study the effects of an external dc field. The angular momentum basis in the model potential expansion is truncated at $l_{max} = 2$ and $l_{max} = 3$ including all the associated m values. The resonance positions and widths are obtained from the complex eigenvalues associated with the non-hermitian analysis of the system of radial equations (3.22) introduced by the CAP.
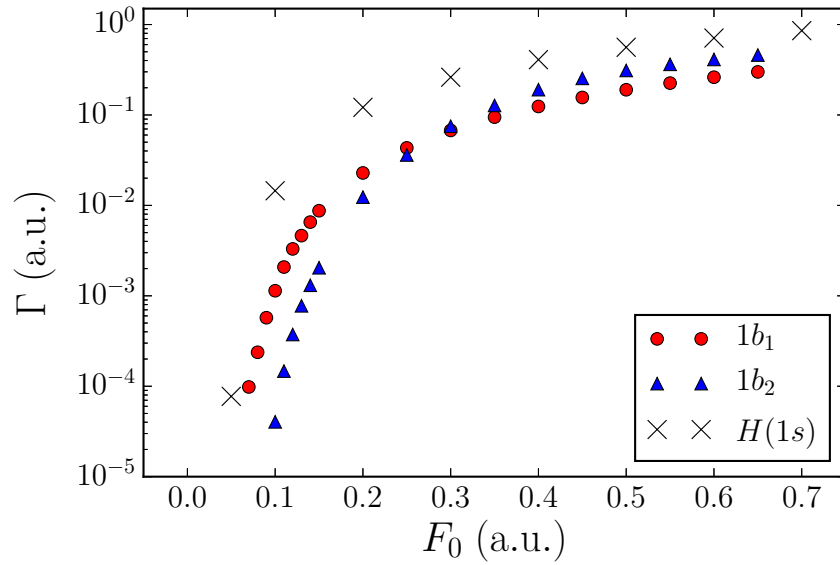
Figure 3.9: Resonance width as a function of the external field strength F_0 for the $1b_1$ (red circles) and $1b_2$ (blue triangles) MOs of H_2O. For comparison, atomic hydrogen $H(1s)$ ionization rates from Refs. [2, 3] are shown as crosses. For weak fields one observes a tunnelling regime with 'threshold' field strengths where the ionization rate rises quickly with F_0.

3.6.1 $1b_1$ and $1b_2$ molecular orbitals

Figure 3.8 shows the resonance position E_R as obtained from the present calculations for the weakly bound $1b_1$ and the strongly bound $1b_2$ valence orbitals as a function of applied electric field strength F_0. In the limit of zero field the calculation reproduces the SCF eigenvalues of Moccia [1]. The field has to be strong (in comparison with atomic hydrogen results for $2p$ orbitals [2]) in order to change the resonance position appreciably. For the more deeply bound $1b_2$ orbital the shift in resonance position saturates with field strength.

In Figure 3.9 the resonance widths are shown for both orbitals as functions of external field strength F_0. The graphs display threshold behaviour at the weaker field strengths. As expected, we find a lower threshold (critical field strength) for the more weakly bound $1b_1$ orbital. Interestingly, however, at a field strength of about $F_0 = 0.3$ a.u. the values for the widths cross; that is, the more deeply bound $1b_2$ orbital displays a larger ionization rate as the field strength is increased further.

Also shown in Figure 3.9 are the widths for the $H(1s)$ orbital from Refs. [2, 3]. They can be compared to the $1b_1$ orbital results, since the binding energy is very close in the free-field limit. Since the tunnelling barrier is mostly in the asymptotic regime where the potential energy has a $-1/r$ tail, it is not surprising that the widths for $H_2O(1b_1)$ and $H(1s)$ share some similarity in shape. In the tunnelling region $H(1s)$ has an ionization rate that is larger by about an order of magnitude. In the over-barrier regime, however, the ionization rates approach each other to within a factor of 3. Reasons for why the $1b_1$ water MO is harder to ionize than $H(1s)$ have to do with the different shape of the orbital density ($m = 1$ *vs* the spherical $H(1s)$ density), and the substantially more attractive potential at shorter distances.

An examination of contour plots of the densities $\Psi^*\Psi$, as well as of the potential energies $V_{\text{eff}} - F_0 z$ for different field strengths (both as a function of r, θ), allows us to make the following observations. For field strengths $F_0 < 0.1$ a.u. there is a barrier the electrons need to penetrate in order to be ionized, which is longer for the more deeply bound $1b_2$ orbital. This explains why the ionization threshold occurs for $F_0 > 0.1$ a.u. for this orbital, which is about a factor of 2 larger than for the $1b_1$ orbital.

The field-strength region where the ionization rates (resonance widths) display a change in character, i.e., turn over to rise much more gradually with the field strength F_0, can be

characterized as a regime where there is a narrow potential saddle at small θ in the vicinity of $r \approx 3$ a.u., such that electron flux can leave and is then accelerated by the electric field. The crossing of the ionization rates for the $1b_1$ and $1b_2$ orbitals occurs since the saddle in the potential becomes effectively lower at strong fields for the $1b_2$ orbital. This can be inferred from the comparison of the two effective potentials, which share the same asymptotic behaviour beyond $r = 4.3$ a.u. (see Figure 3.2).

The origin for the different radial dependencies of the effective potential for the two orbitals can be found in the geometry of the water molecule. The weakly bound $1b_1$ orbital has its lobes perpendicular to the plane defined by the location of the three nuclei. Therefore, it is least affected by the two protons. The $1b_2$ orbital explores the potentials due to the protons more strongly in the SCF calculation of Moccia, and therefore, the resulting $V_{\text{eff}}(r)$ has a more attractive region in the range 0.7 a.u. $< r < 4.3$ a.u..

3.6.2 $3a_1$ molecular orbital

The numerical results from applying the procedure described in Section 3.4 are shown in Figures 3.10 and 3.11.

The resonance positions E_R are shown in Figure 3.10 for external fields applied along the $\pm\hat{z}$ directions (red triangles/blue circles) for a range of external field strengths. For reference, the resonance positions obtained for the $1b_1$ and $1b_2$ MOs using a spherically symmetric potential, $V_{\text{eff}}(r)$, are also indicated in the form of dashed and dot-dashed lines respectively. For zero field strength $F_0 = 0$ self-consistent eigenenergies obtained by Moccia [1] are included as black crosses for the three valence orbitals of interest. The resonance position for the $3a_1$ orbital is bracketed by those for the $1b_1$ and $1b_2$ orbitals.

It can be noticed that for external fields applied along the $-\hat{z}$ direction, where most of the density is located, the field strength F_0 has to be strong, i.e., $F_0 > 0.1$ a.u., for the resonance position to change appreciably. On the other hand, the resonance position for fields applied along $+\hat{z}$ appears to be more sensitive at weaker fields. However the barrier appears to be longer for external fields applied along the $+\hat{z}$ direction, at a field strength of about $F_0 = 0.2$ a.u. the position values cross, indicating a higher sensitivity of the resonance positions for fields applied along the negative $\hat{z}$ direction as the field strength is increased further.
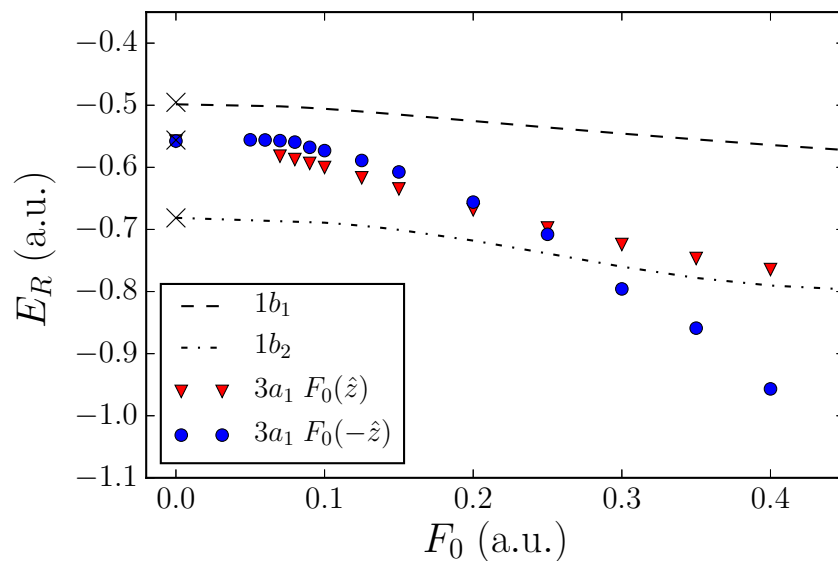
Figure 3.10: Resonance position in atomic units as a function of the external field strength F_0 and the orientation of the field, along the $\pm\hat{z}$ direction (red triangles/blue circles), for the $3a_1$ MO of H_2O. As a reference, the resonance position values for the $1b_1$ (dashed line) and $1b_2$ (dot-dashed line) MOs are also included.
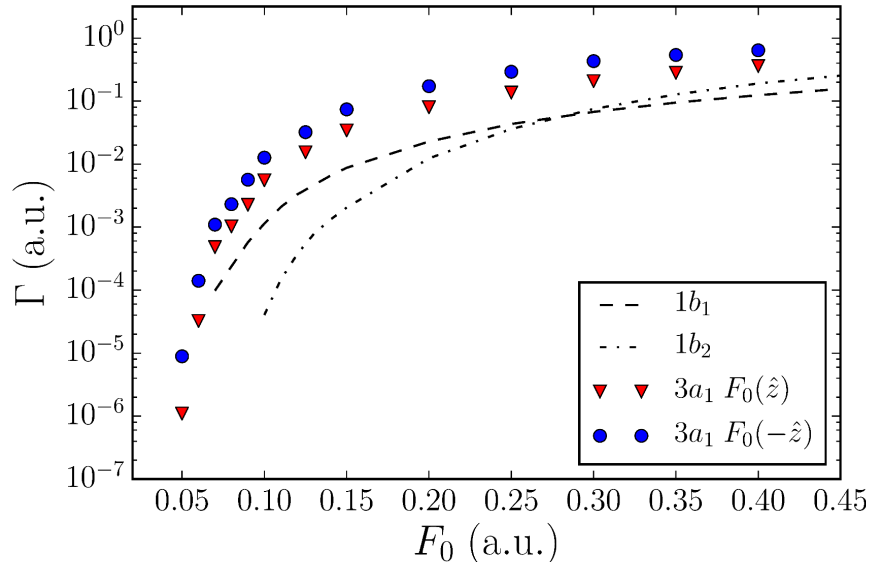
Figure 3.11: Resonance width in atomic units as a function of the external field strength F_0 and the orientation of the field, along the $\pm\hat{z}$ direction (red triangles/blue circles), for the $3a_1$ MO of H_2O. For reference, the resonance widths for the $1b_1$ (dashed line) and $1b_2$ (dot-dashed line) MOs are also shown.

Figure 3.11 shows the resonance widths corresponding to external fields applied along the $\pm\hat{z}$ directions, as a function of the field strength F_0. The results obtained with a symmetric effective potential, $V_{\text{eff}}(r)$, for the $1b_1$ and $1b_2$ MOs are also shown as dashed and dot-dashed lines for comparison purposes.

In analogy to the $1b_1$ and $1b_2$ orbitals, the ionization rates for the $3a_1$ MO, associated with the lifetime of the decaying state via $\Gamma\tau = 1$, exhibit a threshold behaviour at the weaker field strengths. Interestingly, for the two directions of the applied field, we find a lower critical field strength for the $3a_1$ orbital in comparison to what the more weakly bound orbital, $1b_1$, indicates. In the tunnelling region, at $F_0 = 0.05$ a.u., the $3a_1$ orbital for fields applied along the $-\hat{z}$ direction (blue circles) shows an ionization rate that is about one order of magnitude larger than the ionization rate for fields applied in the opposite direction (red triangles), this gap becomes narrower as the field strength increases toward the over-barrier regime. The strong dependency on field direction implies that a different potential barrier is experienced by the electrons for the two cases.

Table 3.3: Resonance positions and widths for different field strengths (in atomic units). The orientation of the external field is indicated by $\pm\hat{z}$. The numbers in parentheses indicate the exponent k, so that the numbers are multiplied by 10^k.

F_0	$3a_1(\hat{z})$		$3a_1(-\hat{z})$		$1b_1$		$1b_2$	
	E_R	Γ	E_R	Γ	E_R	Γ	E_R	Γ
0.05	–	1.09(−6)	−0.556	8.91(−6)	–	–	–	–
0.06	–	3.23(−5)	−0.556	1.41(−4)	–	–	–	–
0.07	−0.582	4.82(−4)	−0.557	1.09(−3)	−0.502	9.82(−5)	–	–
0.08	−0.587	1.03(−3)	−0.559	2.31(−3)	−0.503	2.38(−4)	–	–
0.09	−0.594	2.26(−3)	−0.568	5.65(−3)	−0.504	5.72(−4)	–	–
0.1	−0.600	5.53(−3)	−0.573	1.26(−2)	−0.506	1.14(−3)	−0.689	4.04(−5)
0.125	−0.617	1.54(−2)	−0.589	3.21(−2)	−0.510	3.76(−3)	−0.694	5.45(−4)
0.15	−0.635	3.41(−2)	−0.607	7.39(−2)	−0.515	8.73(−3)	−0.701	2.04(−3)
0.2	−0.668	7.98(−2)	−0.656	1.72(−1)	−0.525	2.28(−2)	−0.718	1.23(−2)
0.25	−0.698	1.37(−1)	−0.708	2.92(−1)	−0.536	4.33(−2)	−0.739	3.61(−2)
0.3	−0.724	2.07(−1)	−0.796	4.31(−1)	−0.546	6.74(−2)	−0.760	7.51(−2)
0.35	−0.747	2.81(−1)	−0.859	5.40(−1)	−0.555	9.46(−2)	−0.778	1.27(−1)
0.4	−0.765	3.60(−1)	−0.957	6.40(−1)	−0.564	1.24(−1)	−0.790	1.91(−1)

The numerical results for the H_2O valence orbitals studied in this chapter, $1b_1$, $1b_2$ and $3a_1$, are summarized in Table 3.3 for further reference, i.e., to allow comparison with future calculations based on other models for the MOs.

3.6.3 Ionization parameters from a partial-wave approach

Figure 3.12 shows the convergence of the three H_2O valence MO eigenvalues as a function of the basis size parameter $l_{\max}$. The comparison with the orbital energies obtained previously using the model potential with a Gaussian basis in a quantum chemistry program [4] (shown as solid lines) reveals that the outermost orbital, $1b_1$, with its density perpendicular to the molecular

plane, converges rapidly, because the density has limited overlap with the hydrogen atoms, as indicated in Fig. 3.1. The calculated orbital energies fall slightly below the quoted values in Ref. [4]. The values indicated as dash-dotted lines correspond to a local self-consistent potential approach, namely the optimized potential method (OPM) [5]. The OPM represents a HF equivalent calculation in which an effective local potential is optimized by means of a variational method to yield self-consistent results that correspond to minimizing the total energy. The OPM total energy and outermost orbital energy are comparable with HF results. The OPM values quoted in Fig. 3.12 are an interesting comparison point since they result from an effective self-consistent potential.

The $1b_1$ orbital is referred to as the highest occupied molecular orbital, and Koopmans' theorem in HF theory [76] can be carried over to DFT methods which have a correct asymptotic form of the effective potential and have been investigated for molecules [77].

For the $3a_1$ orbital, which contributes to the bonding of the water molecule the convergence with $l_{\max}$ is not as fast. One can expect therefore more interesting phenomena from the Stark resonance parameter calculations for this case. Convergence with $l_{\max}$ is really slow for the bonding orbital $1b_2$ due to the fact that a considerable amount of electron density appears along each O-H bond.

The results of complex eigenenergies for the outermost MO $1b_1$ are shown in Fig. 3.13 for $l_{\max} = 2, 3$ as blue and red crosses, respectively. As a comparison the results obtained from the one-centre expansion local potential combined with a modified ECS are indicated as purple crosses. The left panel indicates the real part of the eigenvalue as the resonance position, and the right panel shows the imaginary part, which represents the resonance width. When the electric field is pointing towards the oxygen atom, $F_z < 0$, the electrons are pushed towards the protons, which lowers their eigenenergy considerably (binding is represented by the magnitude of the real part). When the electric field is pointing away from the oxygen, $F_z > 0$, the electrons are attracted towards the nucleus, which initially decrease in binding, but eventually the attraction to the oxygen reinforces their binding as the field strength increases.

The resonance width shown in the right panel indicates that there is a strong dependence on the field strength at weak fields where the tunnelling regime dominates. In this region, there is a marked increase in the exponential decay rate. As the field strength increases in both directions
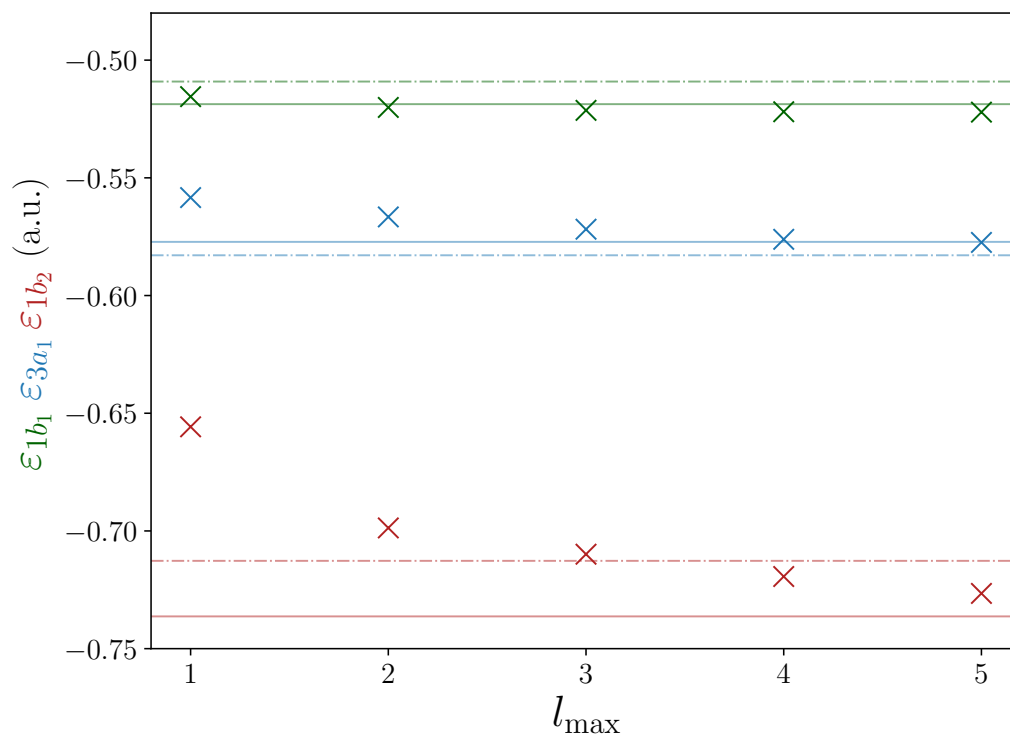
Figure 3.12: Eigenvalues for the H_2O valence MOs $1b_1, 3a_1, 1b_2$ obtained from the model potential (3.17) as a function of the basis truncation parameter $l_{\max}$ are shown in green, blue and red, respectively. The eigenvalues obtained for the model potential as quoted in Ref. [4] are shown as solid lines. Also as a reference, the eigenvalues for an exchange-only density functional theory approximation (OPM) from Ref. [5] are shown as dash-dotted lines.
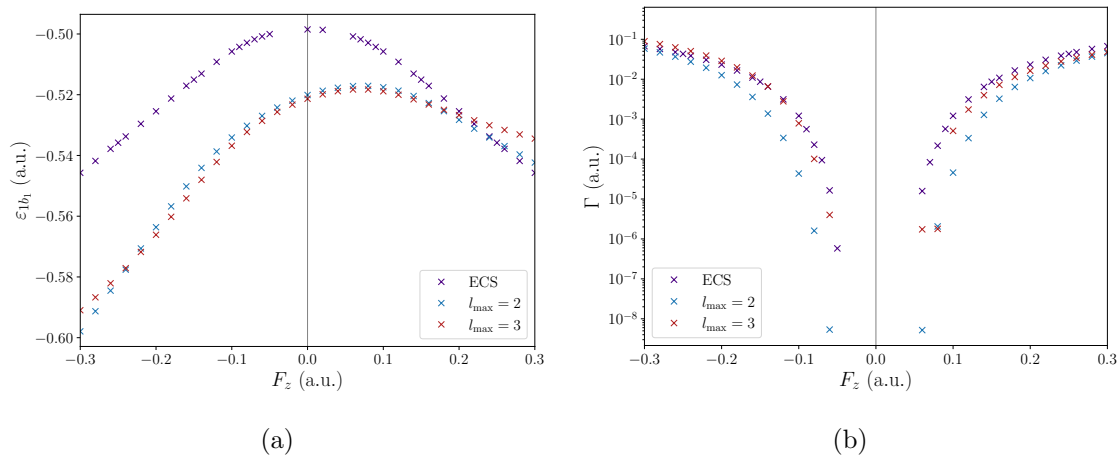
Figure 3.13: Resonance parameters for the $1b_1$ MO of H_2O. The results for the truncation parameter $l_{max} = 2, 3$ are shown as blue and red crosses, respectively. The results obtained with a modified ECS are shown as purple crosses. The electric field is pointing in the molecular plane from the oxygen atom along a centre line between the two hydrogen atoms (for $F_z > 0$), and towards the oxygen atom (for $F_z < 0$).

one observes a turnover towards the over-barrier ionization regime. For $F_z < 0$, the continuous lowering of the orbital energies observed in the left panel is accompanied by an increase in the decay rate that exceeds the rate observed in the opposite direction by about a factor of two in the over-barrier ionization regime.

The complex eigenenergies for the partial-wave-CAP approach corresponding to the $1b_2$ MO are shown in Fig. 3.14. In this case, convergence with the truncation parameter l_{max} is slower than for the $1b_1$ valence orbital. This is consistent with the behaviour observed in Fig. 3.12 for the field-free case. The $1b_2$ orbital, which is the most deeply bound of the three valence orbitals, is harder to ionize as can be noticed in the widths that reach about one half of those for the $1b_1$ MO at strong fields in either direction respectively (see Fig. 3.14b). These decay rates also indicate that for the given field range the tunnelling regime is dominant. As was observed for the $1b_1$ MO, when the electric field points towards the oxygen atom, $F_z < 0$, the $1b_2$ is easier to ionize than in the opposite direction.

Concerning the ECS results, shown as purple crosses in Figs. 3.13 and 3.14, derived from a local effective potential corresponding to a one-centre expansion with an STO basis [44], some
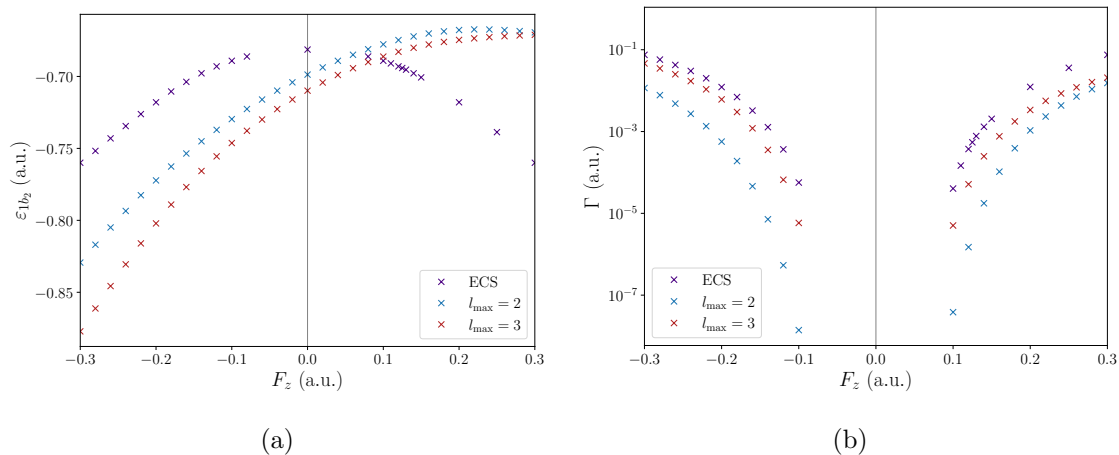
Figure 3.14: Resonance parameters for the $1b_2$ MO of H_2O. The results for the truncation parameter $l_{max} = 2, 3$ are shown as blue and red crosses, respectively. The results obtained with a modified ECS are shown as purple crosses. The electric field is pointing in the molecular plane from the oxygen atom along a centre line between the two hydrogen atoms (for $F_z > 0$), and towards the oxygen atom (for $F_z < 0$).

remarkable features require a discussion. The resonance positions in the left panels show a symmetric behaviour about $F_z = 0$. This contrasts the partial-wave-CAP calculations which are more sensitive to the orientation of the external field showing a more pronounced dc shift for both the $1b_1$ and $1b_2$ MOs, respectively. On the other hand, comparable results are observed in the decay rates as a function of the field orientation and strength shown in the right panels.

The partial-wave results for the $3a_1$ valence orbital are shown in Figure 3.15. The $3a_1$ MO, with a probability distribution along the $\hat{z}$-direction on the molecular plane formed by the three nuclei, presents remarkable results that follow a unique trend. In contrast with the monotonic increase in binding that is observed in Figs. 3.13 and 3.14 when the electric field is pointing towards the oxygen atom ($F_z < 0$), the resonance position (Fig. 3.15a) exhibits a different pattern as the external field pushes the electrons towards the hydrogen atoms. Two oscillating trends are observed, corresponding to each orientation of the dc field. A similar feature was reported for molecular Stark shift calculations based on the total energy of the H_2O molecule [11].

Comparing these results with the previous calculations based on a single-centre SCF effective potential [45], indicated as purple crosses in Fig. 3.15, it can be noticed that the partial-wave ex-
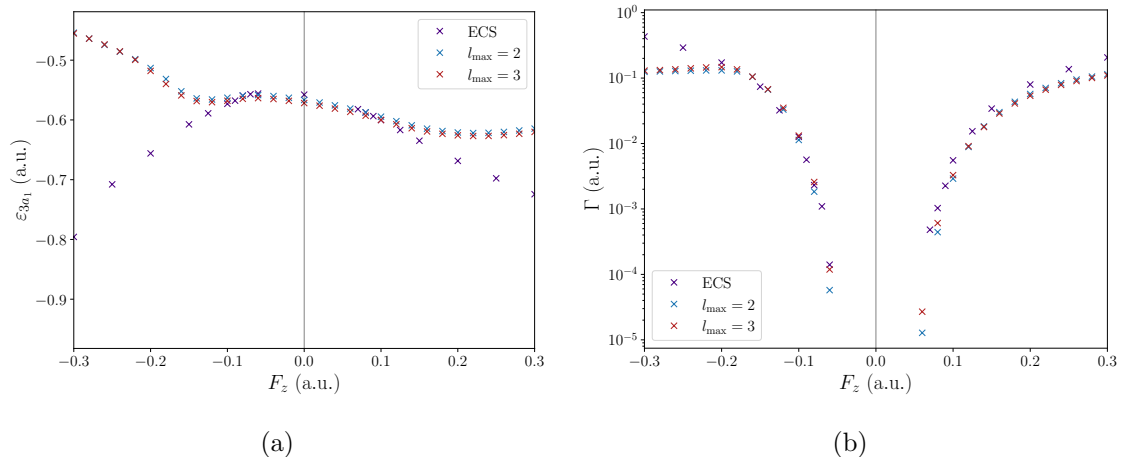
Figure 3.15: Resonance parameters for the $3a_1$ MO of H_2O. The results for the trunca-tion parameter $l_{max} = 2, 3$ are shown as blue and red crosses, respectively. The results obtained with a modified ECS are shown as purple crosses. The electric field is point-ing in the molecular plane from the oxygen atom along a centre line between the two hydrogen atoms (for $F_z > 0$), and towards the oxygen atom (for $F_z < 0$).

pansion of a model potential provides a more sensitive solution that preserves distinctive features of the Stark dc shift and decay rate. Some agreement in the resonance positions can be noticed at low field strengths on each side of the F_z axis. This could be attributed to the extension of the SCF effective potential to include a polar angle dependence for the $3a_1$ orbital (see Eq. (3.15) for the effective potential $V_{eff}(r, \theta)$), as opposed to the $1b_1$ and $1b_2$ orbitals. However, the inclusion of the dependence in this effective potential on the azimuthal angle ϕ seems crucial in order to reproduce the behaviour observed for the dc Stark shift.

As Fig. 3.15b indicates, the resonance widths from previous results are similar to the widths obtained with the partial-wave-CAP approach, with the decay rate diverging for the case where electrons are pushed away from the oxygen atom towards the two protons by about a factor of two at $F_z = -0.3$ a.u.

4 Above threshold ionization in laser-atom and laser-molecule interactions

Generally, the interaction of an atom with intense laser fields is associated with photoionization of the atom by the absorption of one or more photons. In fact, in very intense laser fields an atom may absorb many more photons than the minimum required to get ionized, ejecting an electron of very high energy. The photoelectron energy spectrum associated with this effect exhibits a series of peaks separated by the energy of a laser photon. This phenomenon is known as ATI and was first observed by Agostini et al [16].

ATI has been tackled by means of diverse approaches, with analytical approximations dating back to the Keldysh theory which represents a strong-field approximation [19]. Alternatively, attempts to find a numerical solution to the TDSE [78–80] have been instrumental for the understanding of ATI, and a variety of efforts that deal with the complexity of solving this challenging numerical problem have been successful in the past [18]. In the same way, complementary approaches to the solution of the TDSE, such as the so-called Volkov-state methods [48, 81, 82], have revealed their strengths within strong-laser field problems in which a numerical solution would involve a computationally taxing problem. The strong-field approximation [19], which treats the binding potential of the atom as a perturbation to the ionized electron, is the foundation to the formalism discussed in this chapter.

Section 4.1 introduces some basic notions about strong-field ionization. Sec. 4.2 presents an overview of the pioneering work by Keldysh to describe the laser ionization of atoms. Next, a generalized approach that introduces rescattering of the electron back to the vicinity of the binding potential is included in Sec. 4.3. The ionization regime of a model He atom under a strong-laser field is explored in Sec. 4.4.1 for both scenarios: considering only direct electrons where the ionization spectrum is reproduced by the Keldysh amplitude, and using a compact

expression for the transition amplitude that encloses the limiting case of direct trajectories while allowing electrons to rescatter to the parent ion as well. In addition to working out numerical details presented in Kopold's dissertation [8], in this thesis we explore the laser ionization of the $1b_1$ and $1b_2$ molecular orbitals of H_2O in Sec. 4.4.2. The analysis presented in this chapter closely follows that of [21].

4.1 Multiphoton versus tunnelling ionization

As a result of the interaction with strong laser pulses that compete with the Coulomb forces, the electron dynamics in atoms and molecules is characterized by multiphoton processes that determine their response to the laser field. The Keldysh theory of strong-field approximation illustrates how the dynamics of the underlying phenomena that contribute to the formation of the ionization spectrum evolves as the laser field intensity increases [19].

At moderate intensities, $I < 10^{14}$ W/cm^2, atomic states undergo a transition from bound states into the continuum due to the multiphoton excitation linked to the interaction with the laser field. The interaction with intense laser fields induces an ac Stark shift of the atomic bound states that is responsible for the peak suppression in the ionization spectrum as the field intensity increases [83]. While s states with low principal quantum number n, have a negligible shift in energy due their strong bond and are, in fact, harder to influence by the field, the upward shift of the higher$-n$ states and continuum can become appreciable in the form of an increase in the ionization potential of the atom, I_p, see Figure 4.1(a). This shift is given by the electron ponderomotive energy, $U_p = e^2 E^2/4m\omega^2$, which is the cycle-averaged kinetic energy of a free electron in the electric field of strength E and frequency ω. Although this increase in the ionization potential could, possibly, make some transitions energetically forbidden, in a smoothly varying pulse ionization channels may not be closed for the entire pulse, in such a way that the corresponding peak in the ionization spectrum will not vanish completely [6, 71].

The number of photons required for multiphoton ionization to take place depends on the typical binding energies of the initial states, $E_i = -I_p$. For ionization of a hydrogen atom, $I_p \sim 13.6$ eV, with a typical photon energy of $\hbar\omega \sim 1.5$ eV at 800 nm, at least 9 photons are necessary for the outer electrons to escape the binding potential of the atom and reach the continuum. For the helium atom, $I_p \sim 24.5$ eV, under a laser photon energy of $\hbar\omega = 1.58$ eV,

which we consider in this chapter, at least 15 photons are needed for ionization to occur.

At sufficiently high intensity, $I > 10^{14}$ W/cm^2, and low frequency, the number of photons required for ionization grows considerably and the ionization process is ruled by a tunnelling mechanism. In this regime, intense laser fields are comparable to the Coulomb binding potentials, and ionization can be described by means of a quasi-static approach, in which the bound electrons experience an effective potential that results from the interaction between the laser electric field and the Coulomb attraction from the ion core [19]. This effective potential acts as an oscillating barrier through which electrons can escape via tunnelling, as Figure 4.1(b) illustrates. In the tunnelling regime, since the laser field varies slowly compared to the response time of the electron, the ionization rate becomes the cycle average of the instantaneous dc tunnelling rate. A fundamental quantity in Keldysh theory, known as the Keldysh parameter, is the ratio of the incident laser frequency to the tunnelling rate, and can be written as [19]

$$\gamma = \frac{\omega}{\omega_t} = \sqrt{\frac{I_p}{2U_p}}, \tag{4.1}$$

where I_p is the field-free atomic ionization energy. Eq. (4.1) also explains the different time scales in the tunnelling regime: when $\gamma < 1$ a bigger ionization potential I_p is associated with more rapid electron motion inside the well. As a result the electron motion is on a faster time scale than the laser oscillation period $2\pi/\omega$. The Keldysh parameter illustrates the limits of applicability of the competing mechanisms that characterize the ionization process. For $\gamma < 1$, tunnelling dynamics will dominate, whereas for $\gamma > 1$ multiphoton dynamics will prevail. In this chapter, we focus on the tunnelling regime in ATI.

4.2 Keldysh formalism

Even though the Keldysh formalism for strong-field ionization provided very good agreement with experimental data of electron ATI spectra for helium ionization [84], rescattering effects were not included in the theory and it failed to reproduce the plateau that is visible in measurements along a broad energy spectrum [7, 85], and emerged as a prevalent feature in the ATI energy spectrum. Figure 4.2 shows the measured ATI spectra of rare gases in which a sudden change of slope of the envelope of the peak heights or a plateau is observed. These effects were observed to evolve in a similar manner at certain ranges of the laser-field intensities for all rare gases [7]. For the ATI
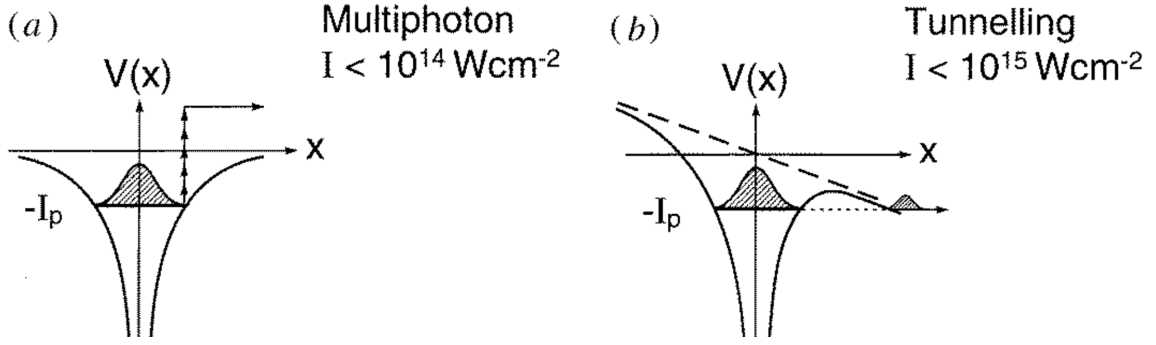
Figure 4.1: Schematic representation of (a) multiphoton ionization and (b) tunnelling ionization as the laser intensity, I, increases. The dashed line corresponds to the contribution to the potential energy due to the instantaneous laser electric field. The solid line represents the full effective potential. From Ref. [6].

spectra shown in Fig. 4.2 the plateaus are more pronounced for Ar and Xe, while it appears to be weaker for He.

A recollision picture in which the strong-field ionization is characterized by several steps, involving tunnelling of the electron followed by a free interaction with the laser field in which the electron returns to the core, was introduced later than the standard Keldysh description [86, 87]. In this chapter we are concerned with the numerical evaluation of an improved Keldysh approximation [21] that accounts for rescattering effects and reveals the complex structure of the ionization spectrum.

The probability amplitude for an electron to transfer from the ground state of an atom with binding potential $V(\mathbf{r})$ into a scattering state $|\psi_{\mathbf{p}}(t)\rangle$ due to an external laser field is given by [21]

$$M_{\mathbf{P}} = \lim_{t \to \infty, t' \to -\infty} \langle \psi_{\mathbf{p}}(t)|U(t,t')|\psi_0(t')\rangle, \tag{4.2}$$

where it is assumed that in the limit of early times, $t' \to -\infty$, the exact wave function reduces to the ground state $\psi_0(t)$. In order to express the total wave function in terms of the unperturbed wave function, the evolution operator formalism [88] is implemented. The time-evolution operator, $U(t,t')$, propagates the wave function $|\psi(t)\rangle$ from t' to t under the full Hamiltonian

$$H(t) = -\frac{1}{2}\nabla^2 + V_I(t) + V(\mathbf{r}), \tag{4.3}$$
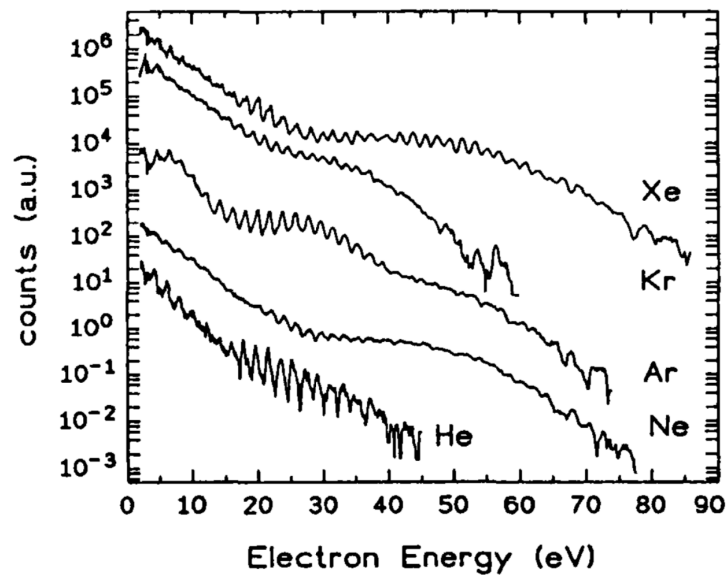
Figure 4.2: Experimental ATI spectra for various noble gases, at a wavelength of $\lambda = 630$ nm and an intensity of $I \simeq 2 \times 10^{14}$ W/cm^2 (3×10^{14} W/cm^2 for He). From Ref. [7]

which includes the binding potential of the parent ion, $V(\mathbf{r})$, and the interaction with the laser field, $V_I(t) = \mathbf{r} \cdot \mathbf{E}(t)$, under the dipole approximation in the length gauge [21] (see Appendix A).

The time-evolution operator satisfies an integral equation, namely the Dyson equation [21, 89], which conveniently allows to construct an expansion in which the interaction with the external field is treated as a perturbation. This representation, together with the orthogonality of the initial ground state $|\psi_0\rangle$ and scattering state $|\psi_{\mathbf{p}}\rangle$, illustrates the possibility of major excursions of the scattering electron away from its parent ion once it was propagated from the initial state by $U(t, t')$.

Two approximations are crucial to derive the Keldysh result for the transition amplitude [21]. The first approximation consists of replacing the complete time-evolution operator in (4.2) by the Volkov time-evolution operator $U^V(t, t')$, which propagates the wave function of a free electron coupled through the interaction $V_I(t)$ to the external laser field and satisfies the Schrödinger equation

$$
[i\partial_t - H_L(t)]U^{(V)}(t, t') = 0
$$
$$
H_L(t) = -\frac{1}{2}\nabla^2 + V_I(t) = -\frac{1}{2}\nabla^2 + \mathbf{r} \cdot \mathbf{E}(t),
\tag{4.4}
$$

In other words, the interaction with the binding potential is considered a perturbation everywhere except in the initial and final states. In the second approximation the scattering state, $\psi_{\mathbf{p}}$, is replaced by the Volkov wave function, $\psi_{\mathbf{p}}^{(V)}$, which represents the state of a free electron in a laser field with time-averaged momentum $\mathbf{p}$. Further details about the derivation are to be found in [21]. These transformations, along with additional algebraic operations, lead to obtain an equivalent form of the standard Keldysh amplitude [21, 90]

$$
M_{\mathbf{p}}^{(0)} = -i \int_{-\infty}^{\infty} dt \, \langle \psi_{\mathbf{p}}^{(V)}(t)|V|\psi_0(t)\rangle.
\tag{4.5}
$$

Generally, replacing the time-evolution propagator $U(t, t')$ by the Volkov propagator $U^{(V)}(t, t')$ is more justified the shorter the range of the binding potential and the higher the intensity of the laser field. In what follows, we will consider the limiting case of zero-range interactions of the form

$$
V(\mathbf{r}) = -\lambda \, \delta(\mathbf{r}),
\tag{4.6}
$$

54

which has one or more bound states depending on λ [18, 46], and restricts the range of the spatial integration in the amplitude (4.5). Zero-range potentials have been widely used in tunnelling [91] and multiphoton ionization problems [92], as well as to simulate the electron dynamics in molecular systems under intense laser fields [93]. Inserting the zero-range potential (4.6) into the standard Keldysh amplitude (4.5) yields the expansion

$$
\begin{aligned}
M_{\mathbf{p}}^{(0)} \sim &\frac{1}{2\pi}\sqrt{2|E_0|} \sum_n \delta\left(\frac{p^2}{2} + U_p + |E_0| - n\omega\right) \\
&\times \sum_{l=-\infty}^{\infty} J_{2l+n}\left(\frac{2p_x}{\omega}\sqrt{U_p}\right) J_l\left(\frac{U_p}{2\omega}\right),
\end{aligned}
\tag{4.7}
$$

that generates the ionization spectrum of direct electrons only [21], i.e., without rescattering. After ionization, direct electrons escape the laser focus without any additional interaction with the ion. The strength parameter of the zero-range potential, i.e., λ is effectively replaced by $\sqrt{2|E_0|}$. With this approximation one completely neglects the Coulomb interaction between ionized electrons and the ion left behind. Here U_p represents the ponderomotive potential of an electron moving in the laser field with momentum $\mathbf{p}$ parallel to the laser field, $p_x = |\mathbf{p}|$, $|E_0|$ stands for the binding energy, and the J_n represent Bessel functions.

4.3 Generalized ionization amplitude including rescattering

As a result of ionization by a strong-laser field, electrons do not depart the ion vicinity immediately after tunnelling the potential barrier and emerging in the continuum. Rather, they are driven by the electric field of the laser, as the field changes in sign, away and back to the core for several laser periods. Under these conditions they may scatter, at least once, off the atomic potential before finally leaving the laser pulse. Rescattering mechanisms determine the universal picture of ATI spectra [17, 46, 85], and, along with momentum conservation, represent the origin of the characteristic plateau that is present in linear-polarization generated spectra [7], as shown in Fig. 4.2. In this section, we are concerned with exploring the ATI energy spectrum of such electrons that interact further with the atomic core and rescatter.

In order to include electron rescattering in our study, it is necessary to allow the electron to interact with the parent ion once it has been freed from the binding potential. This represents a step further in relation to Keldysh theory of direct ionization [19] and it can be implemented by

resorting to the Dyson expansion of the time-evolution operator in which the binding potential is considered a perturbation and the Volkov time-evolution operator plays an essential role. Inserting the expansion for the time-evolution operator into the ionization amplitude (4.2) one obtains the generalized expression [21]

$$
\begin{aligned}
M_{\mathbf{p}} = \ &-i \lim_{t \to \infty} \int_{-\infty}^{t} dt' \langle \psi_{\mathbf{p}}(t) | U^{(V)}(t,t') \{ H_I(t') | \psi_0(t') \rangle \\
&-i \int_{-\infty}^{t'} dt'' V U(t',t'') H_I(t'') | \psi_0(t'') \rangle \},
\end{aligned}
\tag{4.8}
$$

which is still an exact representation of the transition amplitude. The first term is the direct amplitude that yields the Keldysh matrix element discussed in Sec. 4.2. The second term allows for additional interactions with the atomic potential, and therefore describes rescattering of the electron. Further algebraic transformations on the second term result in the compact expression for the ionization amplitude [21]

$$
M_{\mathbf{p}} = \ - \int_{-\infty}^{\infty} dt \int_{-\infty}^{t} dt' \langle \psi_{\mathbf{p}}^{(V)}(t) | V U^{(V)}(t,t') V | \psi_0(t') \rangle,
\tag{4.9}
$$

where the scattering state was replaced by a plane wave in order to carry out the limit of $t \to \infty$. Due to this approximation, Eq. (4.9) is no longer an exact representation of the ionization amplitude. This expression now describes both the direct electrons that depart from the atom without further interaction with the binding potential, as well as the electrons that are promoted to the continuum at some time t', and propagate in the laser field until some later time t when they return to within the range of the binding potential, whereupon they rescatter into their final Volkov state.

Evaluation of the matrix element (4.9) can be very cumbersome for a finite-range binding potential. However, it simplifies noticeably in the limit of a zero-range potential of the form (4.6) where the spatial integrations become trivial. Expanding the Volkov wave function and time-evolution operator in terms of Bessel functions, one of the remaining quadratures over time can be carried out and yields the energy conserving $\delta-$function. Therefore, one quadrature is left to

be carried out numerically,

$$
\begin{aligned}
M_{\mathbf{p}} \sim \sum_n \delta & \left(\frac{p^2}{2} + U_p + |E_0| - n\omega \right) \sum_{l=-\infty}^{\infty} J_{2l+n} \left(\frac{2p_x}{\omega} \sqrt{U_p} \right) \\
& \times \int_0^{\infty} d\tau \ \left(\frac{i}{2\pi\tau} \right)^{3/2} \left(e^{-i[|E_0|\tau + l\delta(\tau)]} \right. \\
& \times \exp \left\{ -iU_p\tau \left[1 - \left(\frac{\sin \frac{1}{2}\omega\tau}{\frac{1}{2}\omega\tau} \right)^2 \right] \right\} \\
& \left. J_l \left(y(\tau) \frac{U_p}{\omega} \right) - J_l \left(\frac{U_p}{2\omega} \right) \right),
\end{aligned}
\tag{4.10}
$$

where the real quantities $y(\tau)$ and $\delta(\tau)$ are defined via

$$
y(\tau)e^{-i\delta(\tau)} = \frac{1}{2} - i \left(\sin\omega\tau - \frac{4\sin^2\omega\tau/2}{\omega\tau} \right) e^{-i\omega\tau} = Z,
\tag{4.11}
$$

and are determined through the absolute value and phase of the complex quantity Z, respectively. In contrast with the amplitude (4.7), in which the generalized Bessel function describes the emission rate of direct electrons, the ionization amplitude (4.10) presents a more complicated structure in terms of these oscillating functions.

4.4   Results

4.4.1   Ionization regime. A systematic study

This section is concerned with the study of the ionization spectrum generated by a strong-laser field acting upon an atom with a binding potential that is approximated as a zero-range potential. The external laser field is assumed to be turned off in the distant past and future, $t \to \pm\infty$. With this in mind, we carry out the numerical evaluation of the transition amplitudes (4.7) and (4.10) in which we concentrate on the case of a monochromatic laser field of the form

$$
\mathbf{E}(t) = \omega A_0 \hat{\mathbf{x}} \sin(\omega t),
\tag{4.12}
$$

where A_0 is the amplitude of the vector potential $\mathbf{A}(t) = -\int \mathbf{E}(t)dt$. For our calculation we consider a laser field with $\hbar\omega = 1.58$ eV at an intensity of 10^{15} W/cm^2, acting upon a He atom with $E_0 = -0.9$ a.u. as the binding energy. Atomic units are used for the field intensity so the relative strengths of the laser versus the atomic binding energy are displayed.

57

The numerical evaluation of the remaining quadrature in Eq. (4.10) in terms of the travel time is not straightforward as the convergence of the solution appears to be sensitive to the working precision requested. Given that the integrand is independent of the electron energy, associated with p_x in Eq. (4.10), a fixed value of the Bessel function order l would correspond to a single value of the integral. This allows us to explore the convergence of the individual integrals that form the sum over Bessel orders before assembling the results to be summed over the discrete energies given by n. In what follows, we will refer to the time integral as $F(l)$ by rewriting Eq. (4.10) as

$$M_{\mathbf{p}} \sim \lim_{|l|_{\max} \to \infty} \sum_{n} \delta \left(\frac{p^2}{2} + U_p + |E_0| - n\omega \right) \sum_{l=-|l|_{\max}}^{|l|_{\max}} J_{2l+n} \left(\frac{2p_x}{\omega} \sqrt{U_p} \right) F(l), \qquad (4.13)$$

where

$$F(l) = \int_0^\infty d\tau \ \left(\frac{i}{2\pi\tau} \right)^{3/2} \left(e^{-i[|E_0|\tau + l\delta(\tau)]} \exp \left\{ -iU_p\tau \left[1 - \left(\frac{\sin \frac{1}{2}\omega\tau}{\frac{1}{2}\omega\tau} \right)^2 \right] \right\} \right.$$
$$\left. J_l \left(y(\tau) \frac{U_p}{\omega} \right) - J_l \left(\frac{U_p}{2\omega} \right) \right). \qquad (4.14)$$

To study the convergence of the sum over l, we partitioned the integration interval into subintervals of $2\pi/\omega$ and explored the progression of the results as a function of how many intervals are included in the calculation as well as the working precision requested. A final interval following the k−th interval, $[2\pi/\omega(k-1), 2\pi/\omega k)$, that extends to $+\infty$ is included in the calculation. Additionally, in order to bypass the singularity at $\tau = 0$ due to the $1/\tau$ factor in $F(l)$, a coordinate transform of the form $x \to \sqrt{\tau}$ is implemented so that the integrand converges to a finite value as τ approaches zero.

Figure 4.3 illustrates the evolution of discrete values of $F(l)$ for a set of l values, $|l| = [10, 40, 80]$, as the working precision is increased. For $l = 10$, a working precision of about 15 decimal points seems to not affect the evaluation of the integral. As l increases, the values of the integral deviate from the initial evaluation until they converge. This happens relatively quickly for negative values of l for which the graphic indicates that approximately 25 digits of precision would be enough to obtain the converged result. In contrast, for $l > 0$ the digits of precision had to be increased to 50 for $l = 80$.

Given that the transition amplitude that describes the rescattering of an electron to its binding potential (4.10) is a generalization of the Keldysh amplitude (4.7) one should expect

58
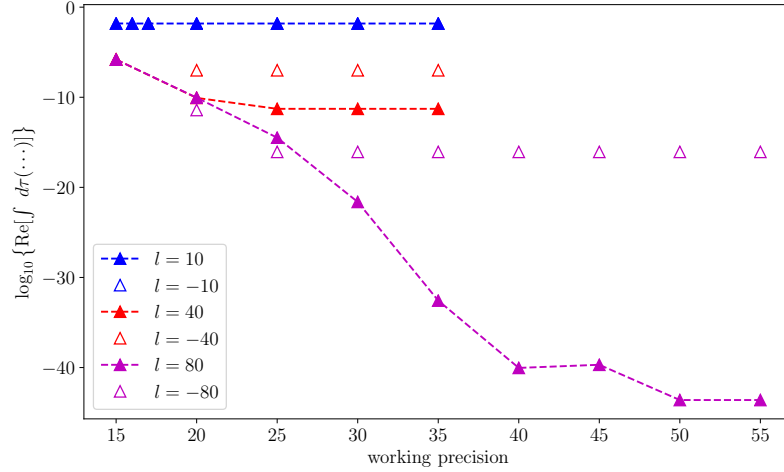
Figure 4.3: Numerical evaluation of the time integral $F(l)$, Eq. (4.14), for $|l| = 10, 40, 80$, indicated in blue, red and magenta respectively, as a function of the working precision requested.

that the generalized ATI spectrum contains that of direct electrons at low electron energies. A comparison between Eqs. (4.13) and (4.7) illustrates that, for a given value of l, the function $F(l)$ should be proportional to the Bessel factor $J_l\left(\frac{U_p}{2\omega}\right)$. This calculation was carried out for different values of l in order to corroborate the validity of the aforementioned generalization.

Figure 4.4 exhibits a comparison of the numerical evaluation of $F(l)$ in (4.13) with the simple Bessel function in (4.7) for several sets of increasing values of $l_{\max}$. It is to be expected that the integrals $F(l)$ are a multiple of the Bessel factor in the Keldysh amplitude for a given range of l values. This can be observed in Fig. 4.4 as the Bessel factors (blue dots) are divided by a factor of 5 to place them on the same scale as the time integrals $F(l)$ (red dots). For negative values of l, at about $l = -30$, the curves begin to differ as the integrals oscillate around 10^{-6} (arb. units) for a range of negative l values that extends from $l \approx -30$ to $l \approx -60$, indicating the presence of rescattering as opposed to the case for the direct transmission, shown as blue dots, from the Keldysh amplitude. As one might notice, for sufficiently small negative values of l ($l < -60$) the values of the integral start dropping below, indicating that convergence of the ionization spectrum for rescattering electrons is to be expected. As the Bessel order, l, was increased in the

59
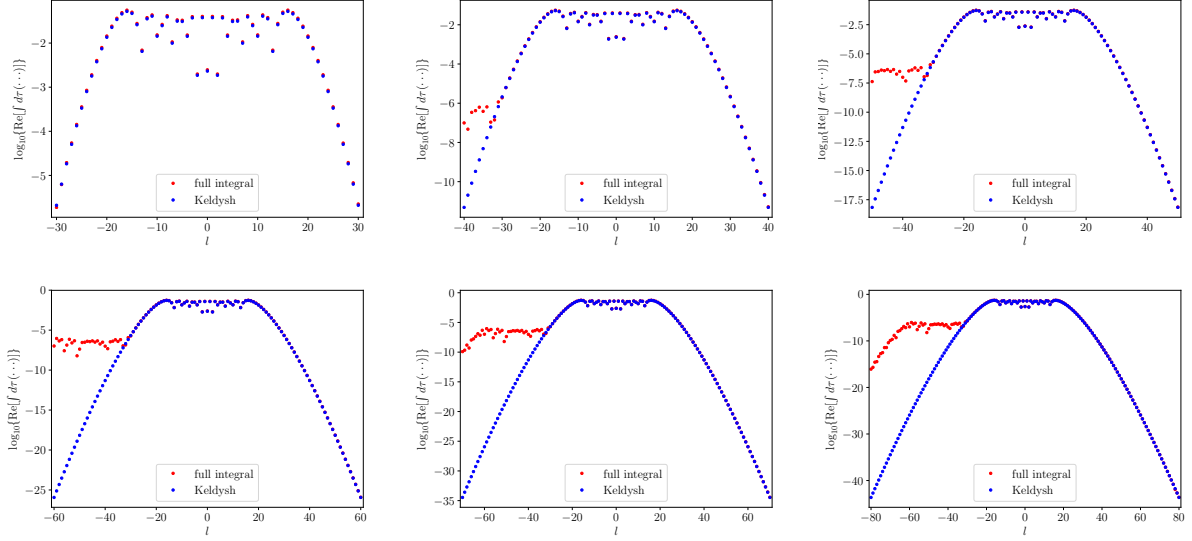
Figure 4.4: Numerical evaluation of the time integral $F(l)$ (4.14) (red dots) in contrast with its analogous Bessel term in the Keldysh amplitude (4.7) for direct transmission (blue dots) for zero-range He atom model as a function of the Bessel function order l for increasing values of $l_{\max}$, $l = [-l_{\max}, \ldots, l_{\max}]$. The Keldysh result (blue dots) is plotted on top of the result from $F(l)$, i.e., the red symbols are covered up by the blue ones when the calculations agree to graphing accuracy.

evaluation of the quadrature, the working precision and precision goal were tuned appropriately so the curves would remain comparable. This is consistent with Figure 4.3, as the order of Bessel functions increases, a higher working precision is required in order to find a numerical solution to the quadrature. The symmetric behaviour followed by the Keldysh result with respect to the Bessel function order is to be expected given the symmetric shape of the Bessel factor $J_l(\frac{U_p}{2\omega})$. In contrast, the time integral $F(l)$ contains a subtraction of Bessel functions in its argument which accounts for the asymmetric behaviour depicted by the red dots.

The ionization spectrum for the He model for emission parallel to the electric field of the laser that contains the contribution of direct electrons, given by the Keldysh amplitude (4.7), is shown in Figure 4.5. For a given electron energy, the sum over the Bessel order was extended up to increasing values of $l_{\max}$, ranging from 20 to 50, in order to display the convergence of the spectrum in the limit $l \to \infty$. For $l_{\max}$ values as low as 20 and 30 the final structure of the
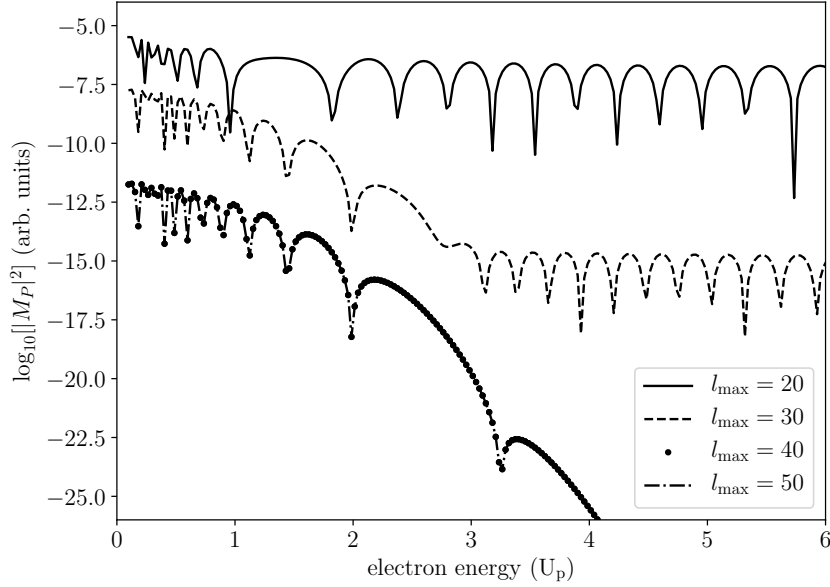
Figure 4.5: ATI spectrum of a zero-range model for helium by a linearly polarized field with a laser intensity of 10^{15} W/cm^2 with $\hbar\omega = 1.58$ eV describing direct electrons. Each curve corresponds to a finite value of $l_{\max}$ in the standard Keldysh amplitude.

spectrum for very small energies, $< 1U_{\mathrm{p}}$, begins to be visible. However, more terms need to be considered in the sum over Bessel functions in order to obtain the converged spectrum. The yield consisting only of direct electrons converges relatively fast to its final shape (dash-dotted line) in which a sequence of narrow suppressions of the probability amplitude separated by rounded tops drops as the electron energy increases and eventually vanishes at about $2.5U_{\mathrm{p}}$.

The results of the calculations based on (4.10) are shown in Figure 4.6. Each coloured curve represents the ionization amplitude for an atom of He under a strong-laser field for increasing values of the Bessel function order, l. As one might notice, the ionization spectrum converges for $l = 80$ (bottom right plot) after undergoing some fluctuations for l values between 40 and 70. The spectrum for direct electrons (black dots) is included as a reference. As it can be seen, both the standard Keldysh amplitude and the generalized ionization amplitude that incorporates rescattering exhibit very similar electron yields for energies lower than $2.5U_{\mathrm{p}}$ where the spectrum is consisting only of direct electrons. As the electron energy increases, the rescattered electrons

begin to exceed the direct ones and the curves start to differ from each other. The transition probability, consisting almost exclusively of rescattered electrons, reaches a plateau consisting of a sequence of suppressions separated by rounded tops. This behaviour is a direct consequence of quantum interference, as the released electrons interfere constructively and destructively in every optical cycle of the laser field as a function of energy. For large energies of about $10U_p$ the plateau shows a cutoff that indicates the end of the rescattering spectrum. The position of this cutoff as well as the onset energy of the plateau fluctuate with the orientation of the emitted electrons with respect to the electric field of the laser as well as with variations of the intensity of the field [7, 21, 47].

4.4.2 Ionization spectrum for the $1b_1$ and $1b_2$ orbitals of H_2O

The study on the H_2O MOs presented in Chapter 3 is extended in this section with the aim of exploring the ATI spectrum of the $1b_1$ and $1b_2$ MOs previously characterized as spherical orbitals. The zero-range model calculation carried out in the previous section combined with the SFA is applied to these valence orbitals in order to explore their response to an intense laser field.

Each MO is treated as an independent spherical orbital in which the eigenvalues ϵ_{1b_1} and ϵ_{1b_2} obtained from the radial representation of their effective potentials, $V_{\text{eff}}(r)$, are considered their binding energies, respectively. With this in mind, it is possible to generate the ionization spectrum for direct electrons and that for rescattering electrons that would correspond to each MO under a strong-laser field. Inserting the molecular binding energies into Eqs. (4.7) and (4.10) one can explore the convergence of the ionization spectrum in terms of the number of Bessel functions included in their respective sums.

Similarly to the case of strong-field ionization of a zero-range He model, the quadrature $F(l)$ in (4.13) remains to be solved in order to obtain the ionization spectrum for rescattered electrons. The general expression (4.10), which encloses the limiting case of ionization of direct electrons, generates an electron yield which follows that of direct electrons for low energies, i.e., energy values below the onset of the ATI plateau. This section is aimed to validate the previous statement and explore the convergence of the ATI spectrum of these two simplified representations of H_2O orbitals.

Figures 4.7 and 4.8 show the values taken by the function $F(l)$ for a set of values of $l_{\max}$,
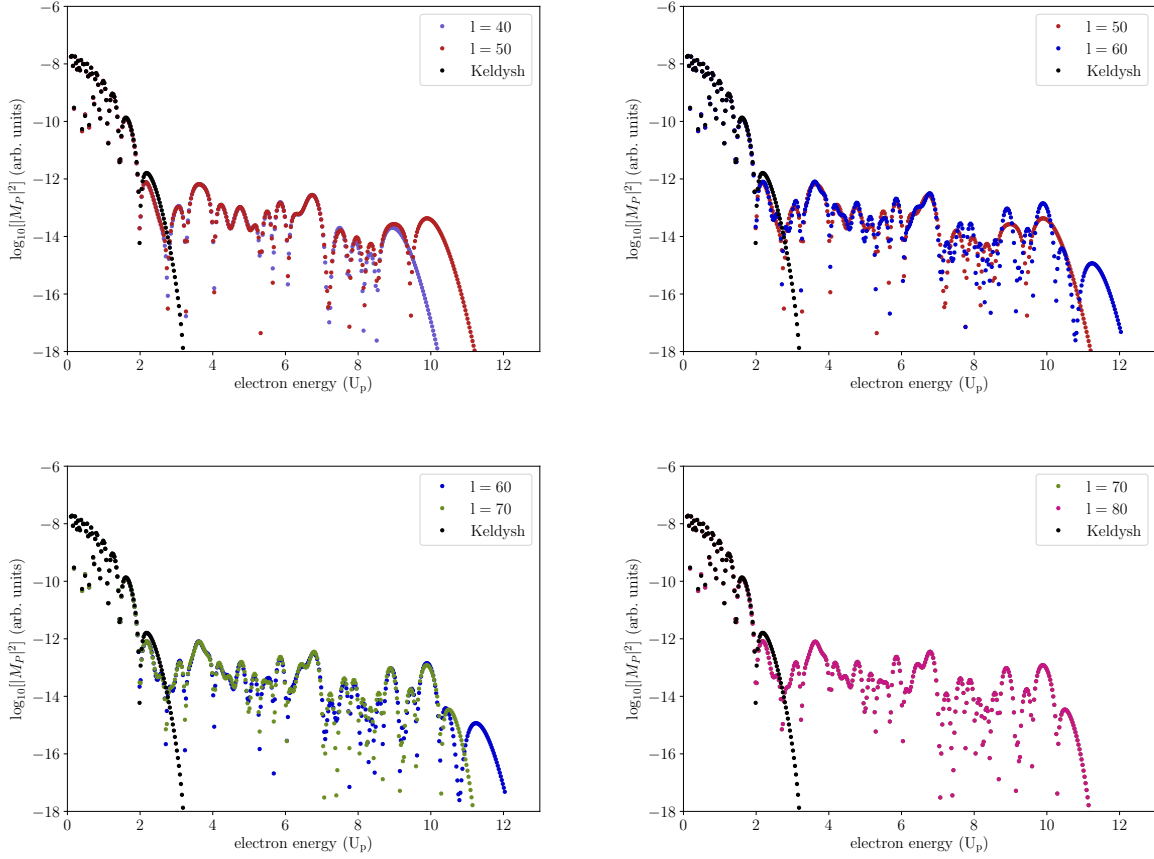
Figure 4.6: ATI spectrum of a zero-range He model with a binding energy of $E_0 = -0.9$ a.u. by a linearly polarized field with a laser intensity of 10^{15} W/cm^2 with $\hbar\omega = 1.58$ eV in terms of an increasing Bessel order, l_{max}, as a function of the electron energy (in colour). The result from the standard Keldysh approximation is shown as the black dotted line.

$l_{\max} = 30, \ldots, 80$, that indicate the extension of the sum (4.10) in terms of Bessel functions and the Bessel term in the standard Keldysh amplitude (4.7) in red and blue, respectively. The numerical values of the integral $F(l)$ were rescaled for both MOs, divided by a factor of 5.5 for the $1b_1$ MO and by a factor of 6.5 for the $1b_2$ MO, in order to make the comparison between the curves visible. Correspondingly, the working precision of the calculations was gradually increased for $|l| > 0$ up to a maximum of 50 digits of precision for $l_{\max} = 80$. As it has been observed for ionization along the electric field of the laser for a He atom [21], the precise agreement between the emission rate for direct electrons and the full ionization spectrum including rescattering for energies below the cutoff of the direct-electron spectrum indicates that a correlation between the red and blue curves should be expected for a range of values of $l_{\max}$ before deviations due to rescattering become substantial. This behaviour can be observed for both MOs for $l < -30$, where the quadrature $F(l)$ reaches a plateau at about 10^{-5} that extends up to about $l < -60$ where signs of convergence of the time integral $F(l)$ become noticeable as the red curve begins to decline.

The ionization spectra corresponding to the $1b_1$ and $1b_2$ MOs are shown in Figures 4.9 and 4.10 as a function of the electron energy. The evolution of the electron yield is presented in terms of the Bessel order l, $40 \leq l \leq 80$. As it can be noticed, expanding the sum in Eq. (4.10) up to $l_{\max} = 80$, purple curve, leads to convergence of the ATI spectrum for both molecular orbitals. Consistently with the comparison with the standard Keldysh amplitude shown in Figures 4.7 and 4.8, as l increases a higher working precision is needed to obtain an accurate representation of the ionization amplitude. It can be seen that the final shape of the spectrum for low energies can be obtained for l values as low as 40. For those energy values one obtains full agreement between the transmission due to direct electrons only (black curve) and the spectrum of rescattered electrons. As the electron energy increases, the Keldysh amplitudes corresponding to both orbitals $1b_1$ and $1b_2$ vanish, giving rise to the onset of the plateau that describes the spectrum consisting entirely of rescattered electrons.
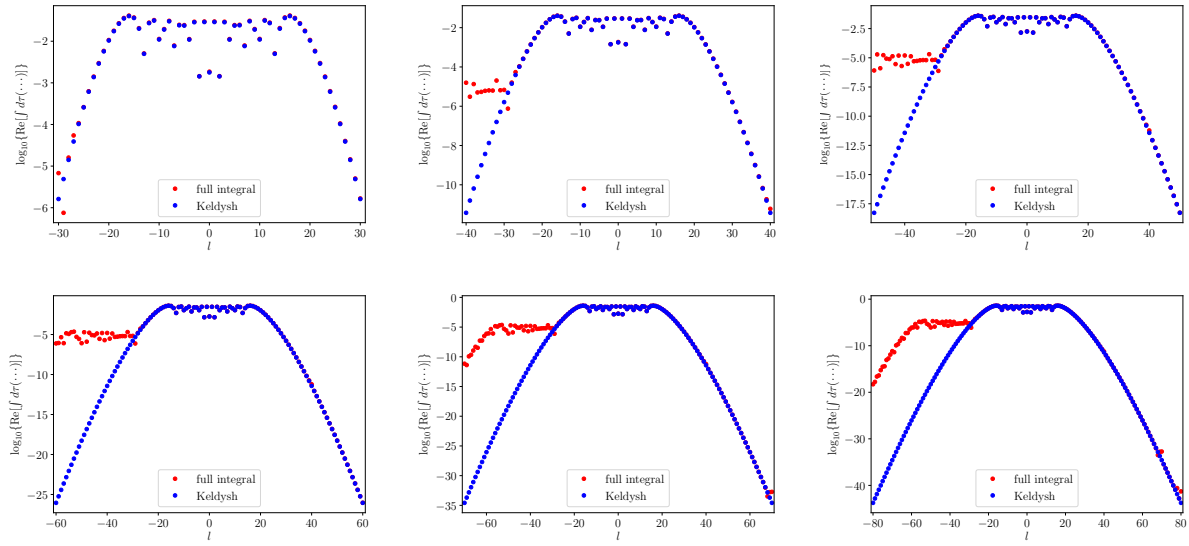
Figure 4.7: Numerical evaluation of the time integral $F(l)$ (4.14) (red dots) in contrast with its analogous Bessel term in the Keldysh amplitude (4.7) for direct transmission (blue dots) for the $1b_1$ MO of H_2O as a function of the Bessel function order l for increasing values of $l_{\max}$, $l = [-l_{\max}, \ldots, l_{\max}]$. The Keldysh result (blue dots) is plotted on top of the result from $F(l)$, i.e., the red symbols are covered up by the blue ones when the calculations agree to graphing accuracy.
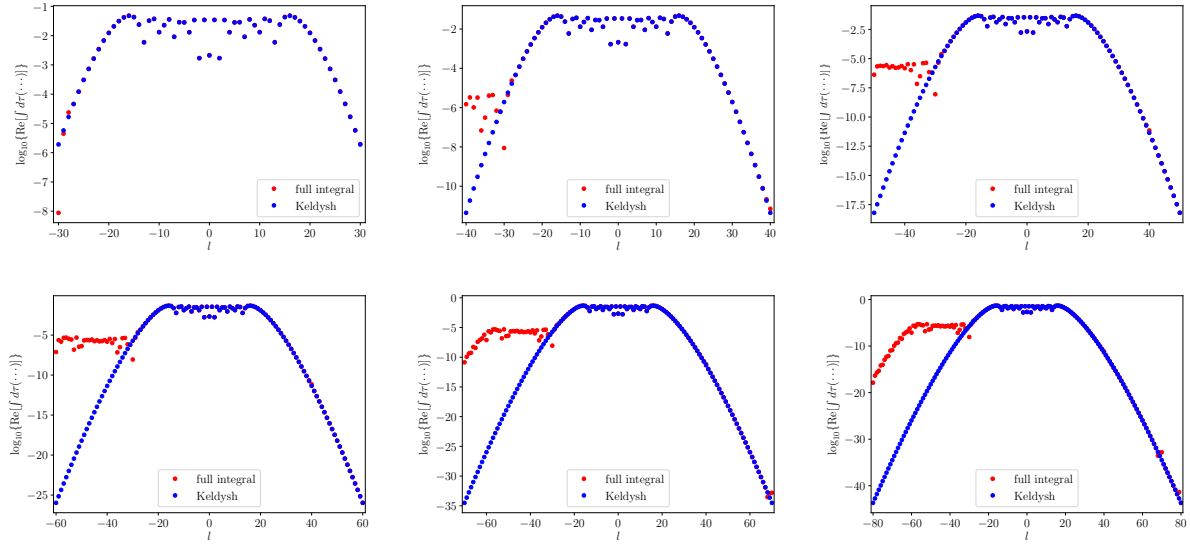
Figure 4.8: Numerical evaluation of the time integral $F(l)$ (4.14) (red dots) in contrast with its analogous Bessel term in the Keldysh amplitude (4.7) for direct transmission (blue dots) for the $1b_2$ MO of H_2O as a function of the Bessel function order l for increasing values of l_{max}, $l = [-l_{max}, \dots, l_{max}]$. The Keldysh result (blue dots) is plotted on top of the result from $F(l)$, i.e., the red symbols are covered up by the blue ones when the calculations agree to graphing accuracy.
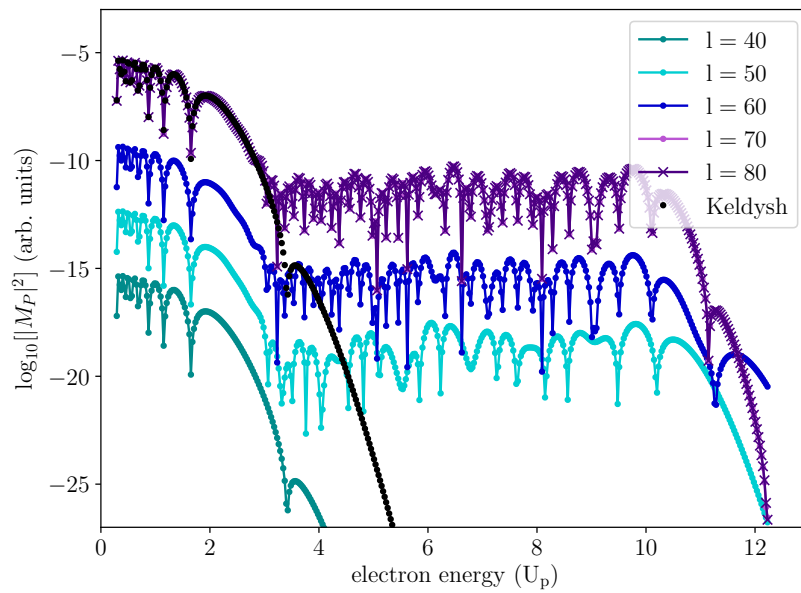
Figure 4.9: ATI spectrum for the $1b_1$ MO of H_2O by a linearly polarized field with laser intensity of 10^{15} W/cm^2 with $\hbar\omega = 1.58$ eV in terms of an increasing Bessel order, l, as a function of the electron energy (in colour). The result from the standard Keldysh approximation is shown as the black dotted line.
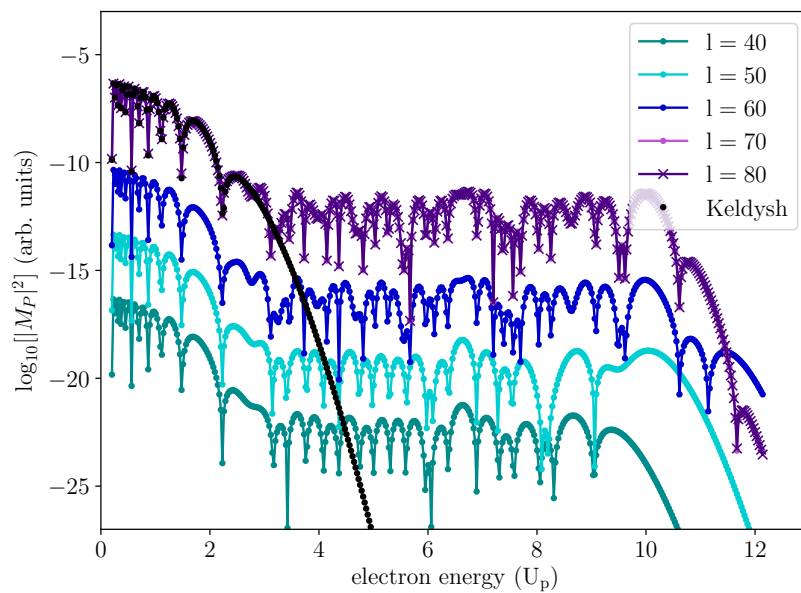
Figure 4.10: ATI spectrum for the $1b_2$ MO of H_2O by a linearly polarized field with laser intensity of 10^{15} W/cm^2 with $\hbar\omega = 1.58$ eV in terms of an increasing Bessel order, l, as a function of the electron energy (in colour). The result from the standard Keldysh approximation is shown as the black dotted line.

5   Saddle point approximation

For laser fields of sufficiently high intensity, the ATI spectrum can be generated by implementing a saddle point evaluation [87] of the multidimensional integral for the transition amplitude obtained in the previous chapter. This semi-classical approximation provides a deeper physical insight than the expansion in Bessel functions from the improved Keldysh approximation [21], as it captures the essential underlying physics. It also establishes a connection between ATI calculations within the framework of the strong-field approximation and the concept of quantum paths [20], which represent space-time trajectories of the tunneling electrons. This concept has its origins in the alternative formulation of quantum mechanics introduced by Feynman in terms of path integrals [49], in which the probability amplitude of a quantum mechanical process can be represented as a coherent superposition of contributions from all possible spatio-temporal paths that connect the initial and final state of the system.

This chapter presents the arguments of Kopold et. al. [8, 20] in an attempt to reproduce their study of ATI on atoms, including electron rescattering, and test for numerical stability. In view of this, the arguments introduced in their saddle-point analysis of ATI are presented in the following sections. The saddle-point approximation establishes the connection between the quantum mechanical path integral formalism and the improved Keldysh approximation discussed in Sec. 4.3. The transition amplitude that describes the ionization of an electron under an external laser field is evaluated within the two frameworks, that in which only direct electrons are considered as well as the case that incorporates rescattering off the parent ion. Our study follows those in Refs. [20, 21].

5.1 Quantum-orbit formalism

Several quantum models have been introduced in the literature that extend the scope of the Keldysh approximation for strong laser-atom interactions. A generalization of the Keldysh-Faisal-Reiss (KFR) formulation of ATI explores the dynamics of the ionized electrons under a high-intensity laser, including rescattering effects, by means of a representation of the time-evolution operator as an expansion with respect to the interaction with the atomic binding potential [21]. The KFR theory of SFA has also been extended to the study of harmonic generation (HHG) [87, 94] by means of a quantum model that takes into account additional interactions of the ionizing electron with the ion core including higher-order terms in a perturbative expansion leading to rescattering effects. This model, which extends beyond zero-range potentials, constitutes a quantum mechanical formulation of the three-step semiclassical picture [95], which has proven to be crucial in understanding strong-field laser-atom interactions. These models, which incorporate rescattering effects of the excited electrons, have been valuable in unraveling the physical phenomena behind the ATI plateau and its cutoff, an intrinsic feature of the ionization spectrum.

A quasi-classical analysis of this generalization, based on the saddle-point method and the path integral formalism [20, 50, 96], has been particularly useful as it illustrates fundamental aspects of the physics underlying strong-field ionization processes as well as the formation of their spectra. This approach suggests that one pictures the processes taking place in laser-atom interactions, such as ATI and HHG, in terms of electron trajectories in phase space. These quantum trajectories, as it is explained below, follow classical Newtonian dynamics, however, time must be defined in the complex plane to account for tunnelling ionization. Consequently, they present non-zero imaginary components for the ionization time, rescattering time and momentum, which determine the probability of the process. Their physical content is reflected in the electron dynamics: once it has been ionized at time t', the electron may return to its parent ion at a later time t and rescatter after propagating in the continuum with momentum $\mathbf{k}$ under the action of the external field.

As a starting point in the evaluation of the ATI probability amplitude 4.9 by means of a saddle-point approximation, we consider the compact form of the Volkov state in the length

gauge (see Appendix A), which can be expressed as [18]

$$|\psi_{\mathbf{p}}^{(V)}(t)\rangle = |\mathbf{p} + \mathbf{A}(t)\rangle e^{-iS_{\mathbf{p}}(t)}, \tag{5.1}$$

where $|\mathbf{p} + \mathbf{A}(t)\rangle$ represents a plane-wave state with momentum $\mathbf{k} = \mathbf{p} + \mathbf{A}(t)$ and

$$S_{\mathbf{p}}(t) = 1/2 \int^{t} d\tau [\mathbf{p} + \mathbf{A}(\tau)]^2 \tag{5.2}$$

denotes the action of the system.

In view of the completeness of the plane-wave states as required by the evolution operator formalism, it can be verified that the Volkov time-evolution operator of Eq. (4.4), which replaces the exact time-evolution operator in the SFA [19], expressed in terms of a Volkov-state decomposition (5.1) by

$$U^{(V)}(t, t') = \int d^3k |\psi_{\mathbf{k}}^{(V)}(t)\rangle \langle \psi_{\mathbf{k}}^{(V)}(t')|, \tag{5.3}$$

is the solution to the initial-value problem (4.4), with $U^{(V)}(t', t') = \hat{1}$, where $\hat{1}$ is the unit operator [88, 89].

Inserting the expansion (5.3) into the matrix element (4.9) and taking into account the time dependence of the ground state wave function, $|\psi_0(t)\rangle = e^{i|E_0|t}|\psi_0\rangle$, one may write the probability amplitude as the five-dimensional integral [20]

$$\begin{aligned}
M_{\mathbf{p}} &\sim \int_{-\infty}^{\infty} dt \int_{-\infty}^{t} dt' \int d^3k \, \langle [\mathbf{p} + \mathbf{A}(t)] e^{iS_{\mathbf{p}}(t)} |V| \mathbf{k} + \mathbf{A}(t)\rangle e^{-iS_{\mathbf{k}}(t)} \\
&\quad \times \langle [\mathbf{k} + \mathbf{A}(t')] e^{iS_{\mathbf{k}}(t')} |V| \psi_0\rangle e^{i|E_0|t'} \\
&\sim \int_{-\infty}^{\infty} dt \int_{-\infty}^{t} dt' \int d^3k \, \exp \, i \left[S_{\mathbf{p}}(t) - S_{\mathbf{k}}(t) + S_{\mathbf{k}}(t') + |E_0|t' \right] \\
&\quad \times \langle \mathbf{p} + \mathbf{A}(t) |V| \mathbf{k} + \mathbf{A}(t)\rangle \langle \mathbf{k} + \mathbf{A}(t') |V| \psi_0\rangle.
\end{aligned} \tag{5.4}$$

The action for ATI, in the exponent of (5.4) consists of three terms

$$S_{\mathbf{p}}(t, t', \mathbf{k}) = -\frac{1}{2} \int_{t}^{\infty} d\tau [\mathbf{p} + \mathbf{A}(\tau)]^2 - \frac{1}{2} \int_{t'}^{t} d\tau [\mathbf{k} + \mathbf{A}(\tau)]^2 + \int_{-\infty}^{t'} d\tau |E_0|, \tag{5.5}$$

which correspond to the action of the entire system after rescattering at time t, between ionization and rescattering where the intermediate free-electron momenta is indicated by $\mathbf{k}$, and before the

71

electron is ionized at time t', respectively. The rescattering amplitude, $M_{\mathbf{p}}$, which is responsible for the high-energy plateau in the electron energy spectrum, takes the form [18, 88]

$$M_{\mathbf{p}} \sim \int\limits_{-\infty}^{\infty} dt \int\limits_{-\infty}^{t} dt' \int d^3\mathbf{k} \exp\left[iS_{\mathbf{p}}(t, t', \mathbf{k})\right] m_{\mathbf{p}}(t, t', \mathbf{k}), \qquad (5.6)$$

with

$$m_{\mathbf{p}}(t, t', \mathbf{k}) = \langle \mathbf{p} + \mathbf{A}(t)|V|\mathbf{k} + \mathbf{A}(t)\rangle \langle \mathbf{k} + \mathbf{A}(t')|V|\psi_0\rangle. \qquad (5.7)$$

This amplitude corresponds to the so-called three-step model [18], in which V represents the potential that the ionized electron experiences when it rescatters off its parent ion. In order to evaluate the total probability amplitude, one needs to integrate over the interval of ionization times t' during which the electric field is non-zero, integrate over all intermediate electron momenta $\mathbf{k}$, and over all rescattering times $t > t'$. The amplitude (5.6) can be approximated using a saddle-point method [94], in which the leading contribution to the ATI spectrum is determined by requiring stationarity of the quasiclassical action (5.5).

It is revealing to point out the contrast of the ionization amplitude (5.6), obtained with the strong-field approximation, with its analogous representation in terms of the Feynman path integral formulation [49]. The time evolution operator of the entire system has the path integral representation

$$U(\mathbf{r}t, \mathbf{r}'t') = \int\limits_{(\mathbf{r}', t') \to (\mathbf{r}, t)} \mathcal{D}\left[\mathbf{r}(\tau)\right] e^{iS(t, t')}, \qquad (5.8)$$

where $S(t, t') = \int_{t'}^{t} d\tau \mathcal{L}[\mathbf{r}(\tau), \tau]$ is the action calculated along a specific path by integrating the Lagrangian of the entire system along that path, and the integral measure denoted by $\mathcal{D}\left[\mathbf{r}(\tau)\right]$ establishes a coherent sum over all possible paths that connect $(\mathbf{r}t)$ and $(\mathbf{r}'t')$. This sum is, in fact, an infinite-dimensional functional of integrals, and can be reduced, within the framework of the SFA, to a sum over a few quantum orbits. By implementing the SFA we have approximated the exact action of the system at the various stages of the process: before ionization, in between ionization and rescattering, and after rescattering, as Eq. (5.5) indicates. The ionization amplitude is then computed by means of a sum over the exponential of the action over a five-parameter set of paths, parametrized by the ionization time t', the rescattering time t and the canonical momentum of the orbit denoted by $\mathbf{k}$ [20].

In the low-frequency limit, in which the time scale of one period of the electron motion is small compared to one laser period, and for high-intensity laser fields, the five-dimensional set of paths over which the transition amplitude (5.6) is evaluated can be reduced further by invoking the saddle-point approximation [94] to calculate the integral over $\mathbf{p}$ as well as t and t'. In this regime, the transition amplitude contains a rapidly oscillating factor, $\exp\, iS_{\mathbf{p}}(t, t', \mathbf{k})$, provided that the parameters U_p, I_p, and p^2 in the quasi-classical action (5.5) are large enough. The major contributions to the integrals in (5.6) come from the saddle points that render the phase stationary.

In the process of evaluating the transition amplitude, the phase of the integrand is expanded about the saddle-points along the path of steepest descent in the complex plane. As a result, a handful of relevant paths remains to be considered in order to explore the ATI spectrum [20]. Since the tunnelling process of an electron is involved in this analysis, these paths take place in the complex time domain. The condition

$$\frac{\partial S}{\partial q_i} = 0, \tag{5.9}$$

where $q_i(i = 1, \ldots, 5)$ runs over the five variables t, t' and $\mathbf{k}$, leads to the saddle-point equations [20, 94]

$$
\begin{aligned}
(\mathbf{k} + \mathbf{A}(t'))^2 &= -\,2|E_0| \\
(\mathbf{k} + \mathbf{A}(t))^2 &= (\mathbf{p} + \mathbf{A}(t))^2 \\
(t - t')\mathbf{k} &= -\int_{t'}^{t} d\tau\, \mathbf{A}(\tau).
\end{aligned}
\tag{5.10}
$$

The solutions $(t_S(\operatorname{Re} t_S > \operatorname{Re} t'_S), t'_S, \mathbf{k}_S)$, are known as the stationary points of the quasiclassical action of the system, and define the quantum orbits which are the essential components in building the ionization spectrum through the saddle-point approximation. From a physical perspective, Eqs. (5.10) ensure the energy conservation at the time of tunnelling, elastic scattering of the electron into its final state when it returns, and that in fact the electron returns to its parent ion, respectively. Since $|E_0| > 0$ in (5.10), the condition of energy conservation at the time of ionization cannot be satisfied for any real time t'. As a consequence, the solutions $(t_S, t'_S, \mathbf{k}_S)$ of the saddle-point equations describe complex orbits which puts limitations on a straightforward visualization of the trajectories.

The probability amplitude (5.6) can now be expressed in terms of the saddle-point solutions as [20]

$$M_{\mathbf{p}} \sim \sum_i \left(\frac{(2\pi i\hbar)^5}{\det(\partial^2 S/\partial q_j \partial q_k)_{j,k=1,\ldots,5}} \right)^{1/2} \times \exp(iS(t_{S_i}, t'_{S_i}, \mathbf{k}_{S_i})), \tag{5.11}$$

where $q_i(i = 1, \ldots, 5)$ runs over the five variables t_S, t'_S and $\mathbf{k}_S$. The sum (5.11) involves a reduced set of trajectories that are sufficient to approximate the ionization spectrum through their interferences, which have constructive and destructive contributions.

5.2   Results

This section presents the results corresponding to a saddle-point analysis of the probability amplitude to detect ATI electrons that emerge from a model-helium atom under a strong laser field of the form (4.12). In order to obtain comparable results to the quantum generalization of the SFA presented in Chapter 4, the laser intensity and frequency were set to $I = 10^{15}$ W/cm^2 and $\omega = 0.0584$ a.u., respectively.

5.2.1   Direct trajectories

The probability amplitude for detecting an ATI electron that propagates with momentum $\mathbf{p}$ in the continuum as a result of the laser irradiation of an atom, originally in its ground state, is studied in this section. The action of a system consisting of a bound electron that is ionized at time t_0, without further interaction with the parent ion, has the form [8, 18]

$$S_{\mathbf{p}}(t_0) = -\frac{1}{2} \int_{t_0}^{\infty} d\tau [\mathbf{p} + \mathbf{A}(\tau)]^2 - \int_{-\infty}^{t_0} d\tau E_0, \tag{5.12}$$

Since the main contribution to the transition amplitude (5.11) is given by the stationary points of the action which satisfy the condition $dS_{\mathbf{p}}/dt_0 = 0$, the integral (5.11) is evaluated by implementing a saddle-point approximation [97]. This consists in expanding the phase of the integrand, $\Phi(t) = (1/\eta)S(t) = (\omega/U_p)S(t)$, in the vicinity of the points where the phase is stationary, which results in determining the solutions of

$$\frac{\partial S_{\mathbf{p}}}{\partial t_0} = \frac{1}{2}(\mathbf{p} + \mathbf{A}(t_0))^2 + |E_0| = 0. \tag{5.13}$$

The stationary points from Eq. (5.13) have a non-zero imaginary component, therefore, it is convenient to split the integral of the action (5.12) in the complex time domain by implementing the substitution $\omega t_0 \to \mathrm{Re}(\omega t_0) + i\,\mathrm{Im}(\omega t_0)$. For a linearly polarized laser field of the form (4.12), the location of the saddle points can be determined analytically and their real and imaginary components satisfy the conditions

$$
\begin{aligned}
\cos^2(\mathrm{Re}\ \omega t_{0s}) &= \frac{1}{2}\left(1 + \gamma^2 + \frac{E_p}{2U_p}\right) - \frac{1}{2}\sqrt{\left(\frac{E_p}{2U_p}\right)^2 + (1+\gamma^2)^2 + \frac{E_p}{U_p}(\gamma^2 - \cos 2\phi)} \\
\cosh(\mathrm{Im}\ \omega t_{0s}) &= -\sqrt{\frac{E_p}{2U_p}}\frac{\cos\phi}{\cos(\mathrm{Re}\ \omega t_{0s})},
\end{aligned}
\tag{5.14}
$$

where ϕ is the angle between the momentum $\mathbf{p}$ and the direction of polarization of the laser field, $\hat{x}$. The electron energy, as it propagates in the continuum, is indicated by $E_p = p^2/2$. As Eqs. (5.14) indicate, an electron energy E_p is associated with four saddle-points ωt_{0s}, $s = 1, \ldots, 4$, which are related to each other by complex conjugation. These complex roots are illustrated in Figure 5.1 for electron energies within the range $(0, \ldots, 6U_p)$. The saddle points with positive imaginary parts, t_{01} and t_{02}, are shown in blue, whereas the red connected dots, t_{03} and t_{04}, indicate points with negative imaginary parts. The contours defined by the saddle points in phase space illustrate the integration paths to follow for a given electron energy when constructing the ATI spectrum.

In a saddle-point evaluation of the integral (5.6), it is convenient to refer to the asymptotic evaluation of the expression

$$
I(\eta) = \int_{\mathcal{C}} dz\, g(z) e^{\eta s(z)}
\tag{5.15}
$$

in the case where the functions $s(z)$ and $g(z)$ are analytic and $\eta > 0$. The integration contour $\mathcal{C}$ is deformed into a composition of contours $\mathcal{C}_s$ coinciding with the path of steepest descent. This transformation into the complex plane, in which the function $s(z) = s(x+iy) = u(x,y) + iv(x,y)$, leads to express the saddle-point condition as

$$
(\nabla u) \cdot (\nabla v) = 0,
\tag{5.16}
$$

indicating that the curves along the directions of ∇u and ∇v always meet orthogonally at any point. Ideally, one needs a path near a point $z = z_s$ such that $u(x,y)$ attains a peak and
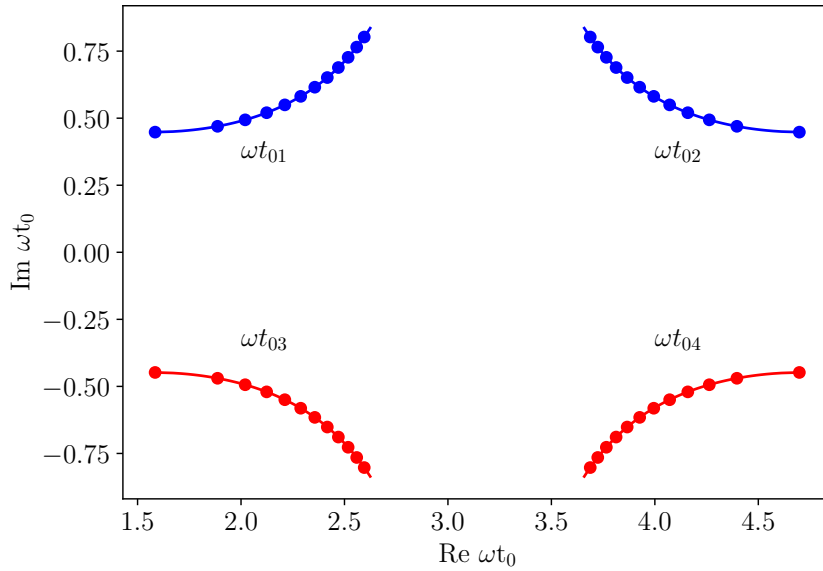
Figure 5.1: Representation of the saddle points corresponding to Eqs. (5.14) that indicate the complex ionization times associated with direct trajectories of electrons ionized by a linearly polarized field with laser intensity of 10^{15} W/cm^2 and $\hbar\omega = 1.58$ eV. The connected dots correspond to discrete energies within the range $(0, \ldots, 6U_p)$. The trajectories with Im $\omega t_{0i} > 0$ are shown in blue, while the ones with Im $\omega t_{0i} < 0$ are indicated in red.

decreases away from $z = z_s$. However, the imaginary part $v(x, y)$ will in general also change and the exponential factor $e^{i\eta v}$ will oscillate rapidly in the vicinity of z_s. If the point $z = z_s$ coincides with a saddle point, a suitable path is one where $v(x, y)$ is nearly constant as one moves away from z_s, in other words, when the exponential term in (5.15) can be expressed as [8]

$$e^{\eta u(x,y) + i\eta v(x,y)} = e^{\eta u(x,y)} e^{i\eta v(x_s, y_s)}. \tag{5.17}$$

Therefore, in order to calculate the saddle point contributions to the integral, one chooses the integration path such that $\text{Im } s(z) = \text{Im } s(z_s)$. Along the direction of steepest descent for the surface $v(x, y) = v(x_s, y_s)$, defined by $-\nabla v|_{z_s} = -(\frac{\partial v}{\partial x}, \frac{\partial v}{\partial y})|_{z_s}$, the Cauchy-Riemann equations justify that the tangents to the surface $v(x, y) = v(x_s, y_s)$ lie in the direction of steepest descent through z_s. In a contour $\mathcal{C}_s$ that goes through the saddle points of $s(z)$, the main contribution to the integral in the transition probability comes from the saddle point $z_s = x_s + iy_s$ or its immediate vicinity. Therefore, a Taylor expansion of the action (5.12) around the saddle point z_s in the form

$$s(z) \simeq s(z_s) + \frac{1}{2!} s''(z_s)(z - z_s)^2 \tag{5.18}$$

is justified. This approximation allows for an analytic determination of the saddle point contributions to the integral (5.15), which can be written as a Gaussian integral and evaluates to [8]

$$I(\eta) \simeq \sum_{s \epsilon \mathcal{Z}_\mathcal{C}} \pm g(z_s) e^{\eta s(z_s)} \sqrt{\frac{2\pi}{-\eta s''(z_s)}}, \tag{5.19}$$

provided that the original contour $\mathcal{C}$ is deformed into a composition $\mathcal{C}_{\max}$ of contours $\mathcal{C}_{s,\max}$ which are regions where $s(z)$ and $g(z)$ are analytic, with identical boundary points $\partial \mathcal{C}_{\max} = \partial \mathcal{C}$. The sum in (5.19) runs over a partial set of all saddle points whose contours $\mathcal{C}_{s,\max}$ combine into $\mathcal{C}_{\max}$.

Accordingly, the KFR matrix element for direct electrons can be approximated by a Gaussian function [8]

$$M_{\mathbf{p}} \sim \int_0^T dt \; e^{i\eta \Phi(t)}, \tag{5.20}$$

in which the phase is defined as $\Phi(t) = S_{\mathbf{p}}(t)\omega/U_p$, and the period of the laser field is indicated by T. The integration path to follow is defined by a contour of saddle points whose locations,

77

indicated in Eq. (5.14), are known analytically for a linearly polarized laser field. This expression results in [8]

$$M_{\mathbf{p}} \sim \sum_i \sqrt{\frac{2\pi}{-iS_{\mathbf{p}}''(t_{s_i})}} \exp iS_{\mathbf{p}}(t_{s_i}), \tag{5.21}$$

where t_{s_i} denote the saddle points that lie in the contour of interest. Equation (5.21) approximates the ATI spectrum for an electron that, after being ionized at some time t_0 under a strong laser field, propagates under the influence of the field with no further interaction with the binding potential.

In order to visualize the regions in phase space where the action $S_{\mathbf{p}}$ is stationary and, consequently, construct an integration path of stationary phase through the saddle-points, it is convenient to carry out the substitution $t \to t_r + it_i$ in Eq. (5.12). For a monochromatic laser field (4.12), and assuming that the electron path is parallel to the electric field of the laser, the real and imaginary components of the phase take the form [8]

$$\text{Im } i\Phi(t) = \omega t_r(1 + \frac{E_p}{U_p} + 2\gamma^2) + \frac{1}{2}\sin 2\omega t_r \cosh 2\omega t_i + 2\sqrt{\frac{2E_p}{U_p}}\sin \omega t_r \cosh \omega t_i \tag{5.22}$$

$$-\text{Re } i\Phi(t) = \omega t_i(1 + \frac{E_p}{U_p} + 2\gamma^2) + \frac{1}{2}\cos 2\omega t_r \sinh 2\omega t_i + 2\sqrt{\frac{2E_p}{U_p}}\cos \omega t_r \sinh \omega t_i. \tag{5.23}$$

At a given electron energy, the permitted integration contours follow from $\text{Im } i\Phi(t) = \text{Im } i\Phi(t_{si})$, and Eq. (5.22) allows to write them explicitly as a function of $t_i(t_r)$. Figure 5.2 shows contours for constant imaginary part of the exponent in Eq. (5.20), as well as the set of saddle points corresponding to an electron energy of $2.27U_p$, indicated by crosses ($\times$). The blue curve corresponds to contours with $\text{Im } i\Phi(t) = \text{Im } i\Phi(t_{s_1,s_3})$, while contours with $\text{Im } i\Phi(t) = \text{Im } i\Phi(t_{s_2,s_4})$ are indicated by a red curve. The purple scale represents the real values of the exponent $i\Phi(t)$, in which dark regions indicate small values of $\text{Re } i\Phi(t)$, while bright regions indicate large values of $\text{Re } i\Phi(t)$. This implies that, for every single electron energy, E_p, only one possible integration path is relevant in order to evaluate the transition amplitude $M_{\mathbf{p}}$: the one starting at $t = 0$ to $+i\infty$, C_a, then along C_1 across the saddle point t_{01} up to $\omega t = \pi + i\infty$ where the integrand vanishes, from there along C_2 across the second saddle point, t_{02}, to $\omega t = 2\pi + i\infty$, and finally along C_b to $\omega t = 2\pi$. The integrands along C_a and C_b are identical and the integrals add up to
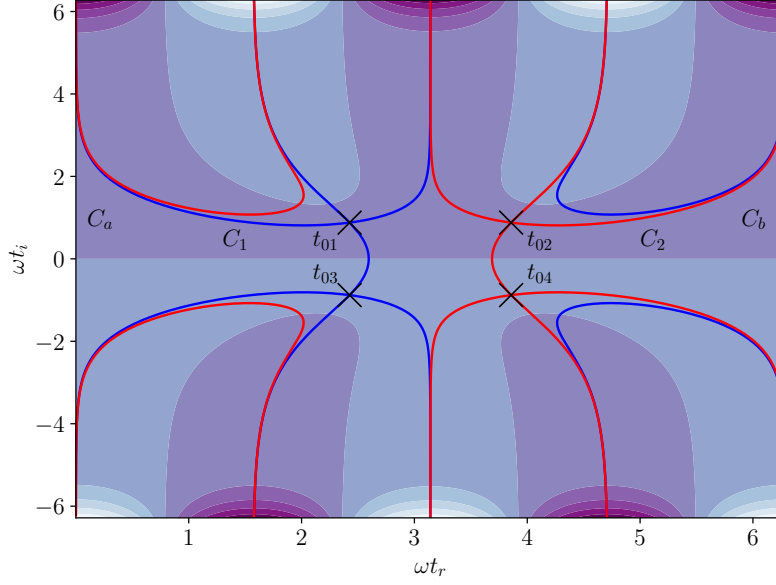
Figure 5.2: Phase contours of Im $i\Phi(t)$ corresponding to the saddle points $t_{01}(t_{03})$ (blue lines) and $t_{02}(t_{04})$ (red lines) for an electron energy of $2.27U_p$ projected on the complex plane. The allowed integration contour runs over the saddle points with positive imaginary parts, t_{01} and t_{02}. The regions in a purple scale represent the real part of the exponent in Eq. (5.20), Re $i\Phi(t)$, in which dark/light regions stand for small/large real parts .

zero due to the reversed integration orders. Along contours C_1 and C_2, the integrand is approximated by the Gaussian (5.21) with $i = 1, 2$. For a given electron energy, E_p, the probability amplitude (5.21) is evaluated along the integration trajectory that contains the saddle-points with positive imaginary parts, t_{01} and t_{02}, indicated as blue connected dots in Figure 5.1, in order to obtain a converging result when evaluating the exponential term in $M_{\mathbf{p}}$.

The described ionization spectrum of direct electrons for a model helium atom calculated by means of the saddle-point approximation (5.21) is displayed in Figure 5.3 by dash-dotted lines. The ATI spectrum corresponding to the exact Keldysh amplitude is indicated with black dots. The saddle-point approximation mirrors the fully quantum calculation in terms of an expansion in Bessel functions. Similarly to what the Keldysh SFA results point out, the saddle-
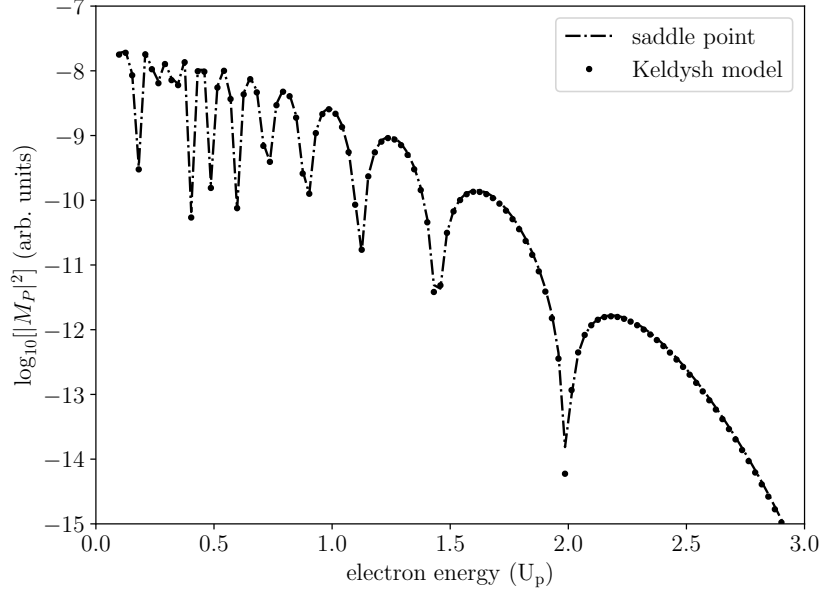
Figure 5.3: Calculated ATI spectrum using Keldysh formalism (black dots) and the saddle-point approximation (dash-dot line) in terms of trajectories 1 and 2, for a laser intensity of 10^{15} W/cm^2, $\hbar\omega = 1.58$ eV, and a binding energy of $E_0 = -0.9$ a.u. for a zero-range He model. The electron energies are expressed in multiples of U_p. The Keldysh parameter and the ratio U_p/ω are $\gamma = 0.654$ and $\eta = 17.9$, respectively.

point approximation generates an ATI spectrum that vanishes at approximately $2.5U_p$ as the electron escapes the effects of the binding potential without further interaction with the parent ion.

5.2.2 Trajectories with rescattering

Incorporating rescattering effects, in which ionized electrons are allowed to return to the parent ion, is important in the study of ATI as it expands the possible physical interpretations to the ionization spectrum. In particular, it elucidates the origin of the extended ATI plateau which can be observed at high electron energies [85]. This plateau, a key feature to the laser induced ATI, is thoroughly justified when rescattering effects are included in the analysis [7, 17], and has been

widely addressed in the literature under the hypothesis that the electrons that are responsible for this plateau gain their energy through backscattering when upon propagation in the laser field they return to the vicinity of the parent ion [7, 46, 47]. It is the purpose of this section to revisit a saddle-point approximation of the rescattering picture in which the quantum orbits of the ionized electron play an essential part in the formation of the ATI spectrum [20].

In the recollision picture, an electron transitions from the ground state into the continuum at time t'_S, ionization time, from that time on the effects of the laser field in the electron dynamics are dominant and the Coulomb potential of the parent ion becomes negligible as the electron propagates in the continuum with momentum $\mathbf{k}_S$, however, the model accounts for further interaction with the binding potential as the electron is considered to return to within the vicinity of the ion at time t_S, rescattering time, at which the electron acquires its final asymptotic momentum $\mathbf{p}$.

The relevant quantum orbits, defined by the complex saddle points $(t'_S, t_S, \mathbf{k}_S)$, are the solutions of the saddle-point equations (5.10) which have their origin in the condition that the action of the system remains stationary along those points. Given that the saddle-point equations (5.10) are real, solutions come in complex conjugate pairs. The existence of these solutions in pairs can be interpreted as a consequence of the invariance of the problem with respect to time reversal. For the linearly-polarized field (4.12), after some algebraic work on the saddle-point equations, one can solve for the rescattering time and ionization time as the numerical solutions of [20]

$$
\begin{aligned}
[\omega t_S \mp \arccos(2\cos\omega t_S + \delta \mp i\gamma)](2\cos\omega t_S + \delta) \\
\pm\sqrt{1 - (2\cos\omega t_S + \delta \mp i\gamma)^2} - \sin\omega t_S = 0
\end{aligned}
\tag{5.24}
$$

and

$$
\omega t'_S = \mp\arccos(2\cos\omega t_S + \delta \mp i\gamma),
\tag{5.25}
$$

respectively, where the quantity δ is defined as $\delta = \sqrt{p^2/(4U_p)}$. Therefore, the complex paths are generated for every possible set of saddle points $(t'_i, t_i, \mathbf{k}_i)$, where i indicates the $i-$th quantum trajectory. As Eq. (5.24) indicates, solutions for the rescattering time come in complex conjugate pairs. Each optical cycle $\omega T = 2\pi$ contains two solutions for the return time t_i for each of the two possible combinations of signs. Considering the periodicity of the laser field (4.12), we can focus our attention to the interval $0 < \text{Re } t_i < T$ for the rescattering times. Subsequently,

81

Eq. (5.25) generates a pair of solutions for the ionization time t_i' within every interval delimited by $-(\frac{n+1}{2})T < \text{Re } t_i' < -(\frac{n}{2})T$, with $n = 0, 1, \ldots$, as can be noticed in Figure 5.4 (right).

In Figure 5.4, a subset of these numerical solutions illustrates the described distribution for the release and return times corresponding to the first six quantum orbits, $i = 1, \ldots, 6$, for a fixed electron energy of $E_p = 6U_p$. It can be noticed that in both cases, i.e., return times and ionization times, the solutions come in pairs for each optical cycle of the laser field. The left panel shows the roots of Eq. (5.24) for the return times corresponding to three consecutive optical cycles. In addition, the electric field of the laser, Eq. (4.12), is depicted in the left panel with dash-dotted lines for the optical cycle $0 < \omega t < \omega T$. The right panel indicates the release times that are obtained as the roots of Eq. (5.25) once the return times are calculated. The release times illustrate how additional pairs of solutions become available for lower energies, with t_i' extending further into the past.

The value of the ponderomotive energy, U_p, at which the two trajectories of a given pair approach each other most closely corresponds to the cutoff of this pair. Typically, the orbits that correspond to a given cutoff energy are defined as long and short orbits [17]. Each pair of trajectories (i, j) has its well-defined cutoff at some energy, E_{cutoff}, at which the orbits come together, and the pair ceases to contribute to the ionization spectrum for $E_p > E_{\text{cutoff}}$. The inset in the left panel of Figure 5.4 depicts the described behaviour for the pair $(1, 2)$ of quantum orbits, the curves indicate the numerical solutions for the return times corresponding to three different values of the electron energy. No solutions can be found for the return times, and subsequently the release times, if the electron energy exceeds the cutoff energy associated to a given pair. The cutoff energy for the pair $(1, 2)$ comes out to be $10.24U_p$ as Figure 5.4 indicates. Typically, the travel time, $\text{Re}(t_i - t_i')$, associated with a quantum orbit indicates the relevance of its contribution to the ATI spectrum, the ones with shorter travel time being qualitatively more relevant, as they make up for the strongest contributions to the ionization spectrum.

The complex orbits for the ionization time, rescattering time and complex momentum, given by the saddle-point solutions of Eqs. (5.24) and (5.25), are shown in Figure 5.5 for trajectories $i = (1, \ldots, 6)$ as a function of the electron kinetic energy E_p. A subset of the energy values is indicated in multiples of U_p along the paths. In the process of obtaining the saddle points corresponding to trajectories with increasing travel times, the substitution $\omega t \rightarrow \omega t + 2\pi k$, with

82
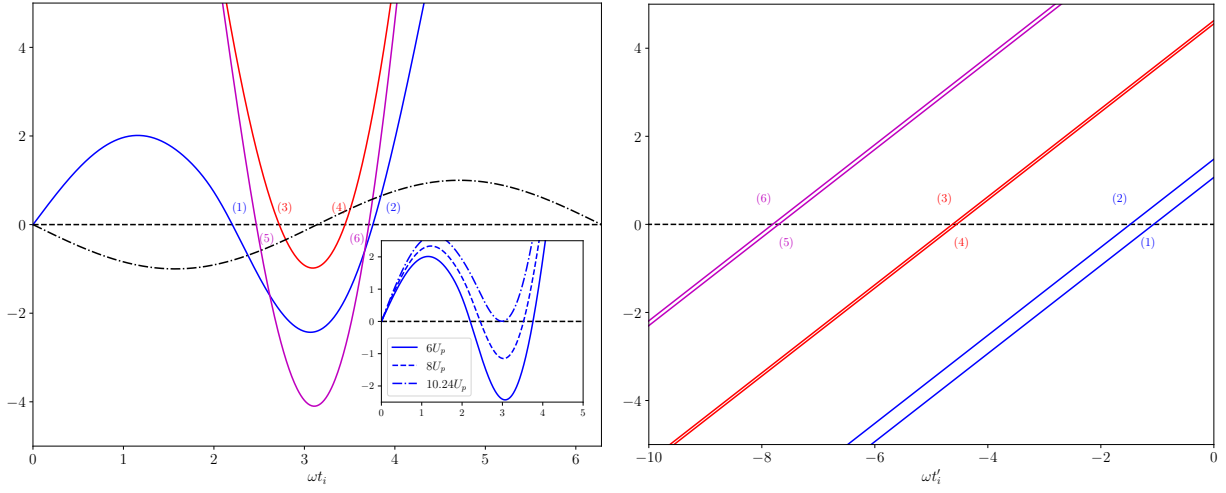
Figure 5.4: Results of a numerical determination of the return time t_i and the release time t_i' based on Eqs. (5.24) and (5.25) for a specified electron energy, $E_p = 6U_p$. The intersections with the $y = 0$ axes indicate the real components of pairs of return time (left) and their corresponding release times (right). The numbers in parentheses refer to the numbers of individual trajectories. The electric field corresponding to the monochromatic field (4.12) is depicted in the left panel in dash-dotted lines. The inset in the left panel depicts the numerical solutions for the return time as the electron energy increases.

$k = 0, 1, \ldots$, was implemented in Eqs. (5.24) and (5.25). The behaviour of these complex trajectories is markedly different depending on the location of the classical cutoff. Every pair of trajectories shows that the quantum orbits approach each other closely near the cutoff. For energies above the cutoff, the orbits in every pair diverge away from one another and the ones with negative imaginary parts stop contributing to the ATI spectrum and are dropped from the sum (5.11), as they lead to a diverging solution for the probability amplitude. This cutoff marks a turning point in the complex paths. It can be noticed that both the rescattering times and quantum momenta have very small imaginary parts before the cutoff, while their imaginary components become noticeable as the electron energies increase beyond the cutoff. In contrast, the imaginary parts of the ionization times are significant, indicating the origin of the electrons through tunnelling ionization. For energies above the cutoff, the real components of the complex paths remain approximately constant with increasing energy. As a result, a marked drop appears after the cutoff in the spectrum associated with a given pair of trajectories.

It is illustrating to take into account the complex nature of the electron dynamics in order to visualize how the action of the system, $S(t_i, t_i', \mathbf{k}_i)$, evolves as the electron energy increases. To this end, one can write the explicit analytic expression for the action in the event that the canonical momentum $\mathbf{k}$ and the final momentum $\mathbf{p}$ are parallel to the linearly polarized laser field (4.12), which reads

$$
\begin{aligned}
S(t, t', \mathbf{k}) &= -\frac{1}{2} \int_t^\infty d\tau \left[p^2 + 2A_0 p \cos(\omega\tau) + A_0^2 \cos(\omega\tau)^2 \right] \\
&\quad -\frac{1}{2} \int_{t'}^t d\tau \left[k^2 + 2A_0 k \cos(\omega\tau) + A_0^2 \cos(\omega\tau)^2 \right] \\
&\quad + \int_{-\infty}^{t'} d\tau |E_0|.
\end{aligned}
\tag{5.26}
$$

In the vicinity of the saddle points $(t_i, t_i', \mathbf{k}_i)$, where the action satisfies the stationarity condition (5.9), the integration limits that cause the integrand to diverge to $\pm\infty$ can be neglected. Some algebraic simplifications on the analytic expression for the action allow us to express the
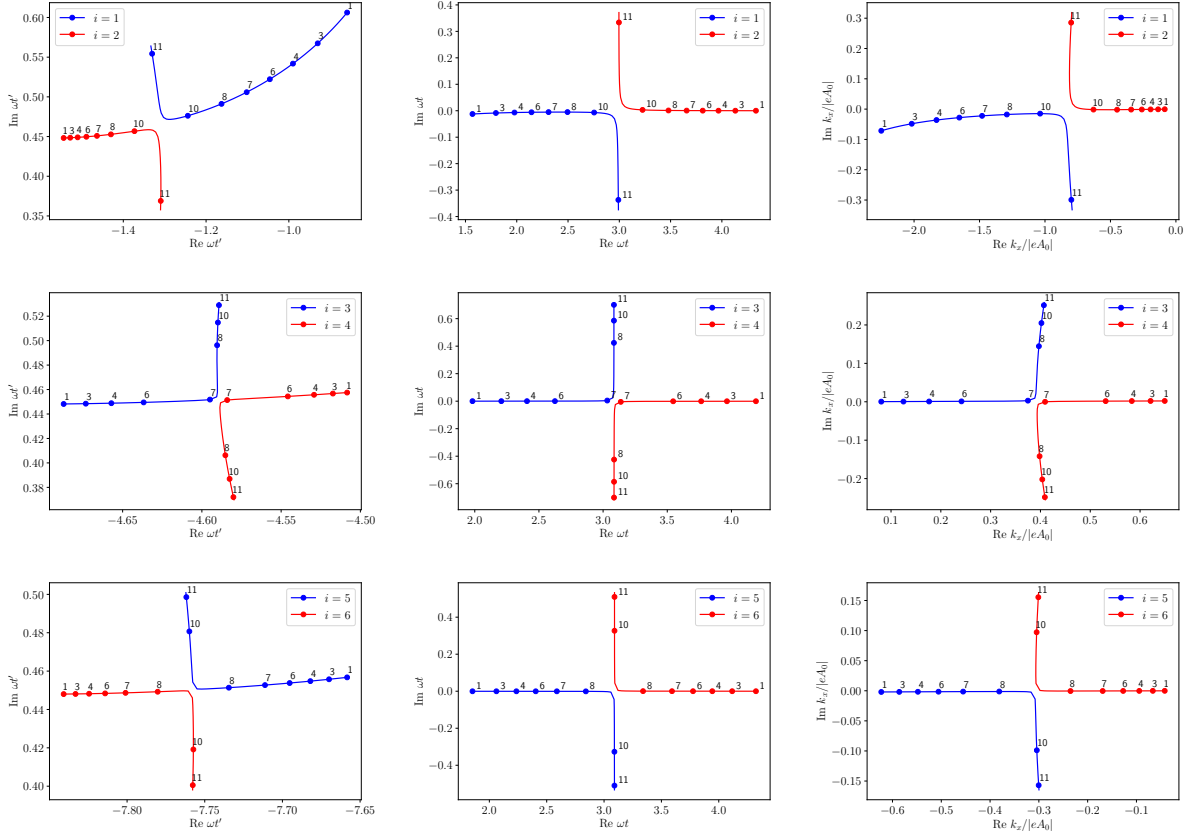
Figure 5.5: Saddle points for the orbits $(s = 1, \ldots, 6)$ in the complex plane as a function of the electron energy E_p specified along the lines in multiples of U_p. A laser field of 10^{15} W/cm^2 and $\hbar\omega = 1.58$ eV and a binding energy of $E_0 = -0.9$ a.u. were used in the calculations. In this figure, $\omega t'$ represents the ionization time, ωt stands for rescattering time, and k_x is the $x-$component of the canonical momentum $\mathbf{k}$. The underlying Keldysh parameter is $\gamma = 0.464$.

phase, $\Phi = (1/\eta)S$, in the probability amplitude (5.11) as

$$
\begin{aligned}
\Phi(t, t', \mathbf{k}) \;\; = \;\; & \left(\frac{E_P}{U_P} - \frac{k^2}{2U_P} \right) \omega t - \frac{2}{\sqrt{U_P}} \left(k - \sqrt{2E_P} \right) \sin(\omega t) \\
& + \left(\frac{k^2}{2U_P} + 1 + 2\gamma^2 \right) \omega t' + \frac{2}{\sqrt{U_P}} k \sin(\omega t') \\
& + \frac{1}{2} \sin(2\omega t'),
\end{aligned}
\tag{5.27}
$$

where $E_P = p^2/2$ indicates the electron energy.

The phase values $S(t_i, t'_i, \mathbf{k}_i)/\eta$, with $\eta = 35.8$, corresponding to the electron trajectories with the shortest travel times $(i = 1, 2)$, are shown in Figure 5.6 as a function of the electron energy E_p as blue/red lines, respectively. A subset of energy values is specified along the curves up to the cutoff energy, whereupon a crossing takes place between the paths. Additionally, the complex coordinates of the action that were graphically extracted from [8] are marked by crosses ($\times$) for the electron energies specified. The relative error of the action (5.26) with respect to the saddle-point results from [8] is indicated with errorbars for the three energies considered. For energies below the cutoff the most noticeable changes occur in the real components, while the imaginary parts of the individual trajectories change little as they approach each other along the plateau. In contrast to the saddle point behaviour (Figure 5.5), where in a given pair of trajectories (i, j) they diverge rapidly from one another towards the cutoff, the complex contributions of the action approach one another as the electron energy increases and eventually are interchanged at the cutoff, at which point one of the trajectories ceases to contribute to the ATI spectrum.

The computation of the ATI spectrum can now be carried out once the solutions of the saddle-point equations are determined. To this end, the appropriate subset of electron trajectories is inserted into the matrix element (5.11). Figure 5.7 depicts the formation of the ATI spectrum as an increasing number of quantum orbits are included in the sum (5.11). The contribution to the spectrum of a given pair of trajectories (i, j) reflects its cutoff energy, upon which the sequence of interference maxima and minima is terminated by a sharp peak where the two trajectories diverge and one of them increases exponentially and stops contributing to the spectrum. The pair $(1, 2)$ with the highest cutoff energy (around $10U_p$ as shown in Figure 5.5) and shortest travel time presents the dominant contribution to the ATI spectrum. The second most important contribution comes from the pair $(3, 4)$, which has the lowest cutoff energy at around $7U_p$ and
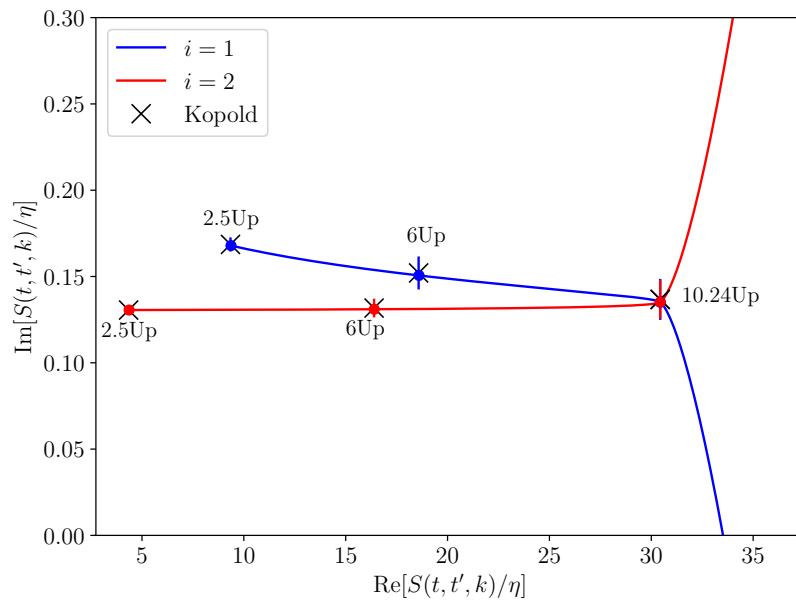
Figure 5.6: Representation of the action in the complex plane for the two shortest trajectories $(1, 2)$ shown in blue and red respectively. In addition, the complex coordinates for the action extracted from [8] are shown as $\times$ for the specified energy values.
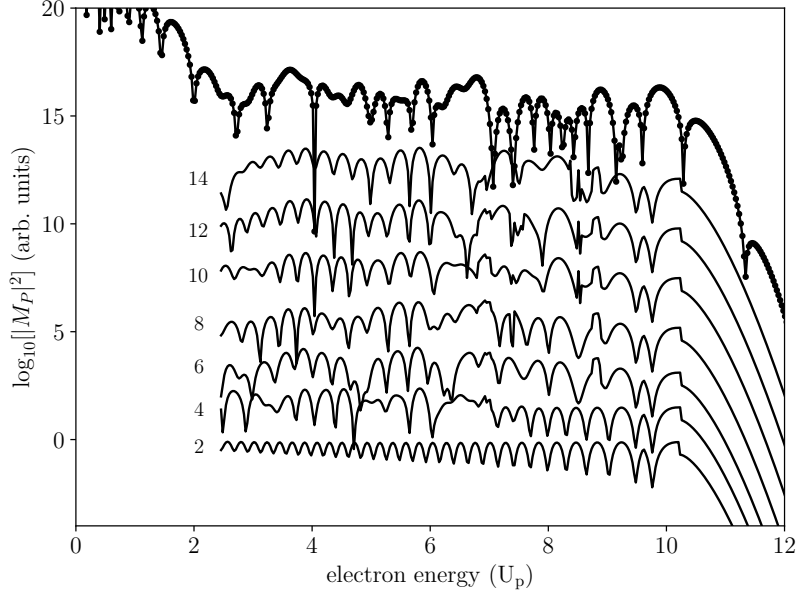
Figure 5.7: Saddle-point evaluation of the ATI spectrum as a function of the electron energy in terms of an increasing number of quantum paths. A laser intensity of 10^{15} W/cm^2 and frequency $\hbar\omega = 1.58$ eV were used in the calculations, as well as a binding energy of $E_0 = -0.9$ a.u. corresponding to a model-helium atom. The number of relevant trajectories, increased by two on each additional spectrum, is highlighted at the left of the curves. The dot-dashed curve (top) represents the calculation of the ATI spectrum from the integral (4.13).

second shortest travel time. Its final broad-top maximum, at around $6U_p$, remains visible in the converged spectrum. As further pairs of trajectories with increasing travel times are included in the calculation, their overall contribution to the spectrum decreases. In contrast with previous results [20], in which the shortest six trajectories provided a good approximation to the ATI spectrum, our calculations indicate to be more sensitive to adding further trajectories to the sum (5.11), as the converged ATI spectrum becomes visible with the contributions from 14 quantum paths.

6 Conclusions

In this dissertation we have developed a study of the ionization of the H_2O molecule valence orbitals under an electric dc field in which NHQM techniques have been implemented. Additionally, a systematic study of the ATI spectrum for a model-He atom was carried out following an extension of the SFA. In the following subsections more detailed and summarized conclusions are offered for these studies.

6.1 H_2O in an external dc field

PDE system with a modified ECS

We have carried out a study of the H_2O valence orbitals, $1b_1$, $1b_2$, and $3a_1$, in the presence of an external electric dc field applied along the symmetry axis of the molecule, $\mathbf{F} = F_0\hat{z}$. As a starting point, an orbital-dependent effective potential was extracted from a self-consistent solution for the H_2O MOs expressed as an expansion on a basis of single-centre Slater-type orbitals [1]. The $1b_1$ and $1b_2$ molecular orbitals were approximated by orbitals in a spherically symmetric potential and expressed as linear combinations of $2p_x$ and $2p_y$ orbitals, respectively. In the case of the $3a_1$ orbital, $s - p$ type Slater orbitals were considered in addition to retaining the $2p_z$ parts of the MO expansion.

A modified ECS technique was applied to the radial coordinates in the Schrödinger equation with orbital-dependent effective potential for each MO as part of solving the complex eigenvalue problem to obtain the Stark resonance parameters. By means of a phase factor the scaling was turned on gradually beyond some distance from the origin of coordinates. The ECS parameters, r_s and Δr, as well as the asymptotic scaling angle, χ_s, were optimized in order to guarantee a minimum of two to three significant digits in the solutions. The tunnelling ionization and

over-barrier ionization regimes were explored by finding a numerical solution to the PDE system resulting from separating the complex-valued wave function into real and imaginary parts [44, 45].

The resonance parameters that describe the ionization process, resonance position and width, were explored over a wide range of electric field strengths. It was demonstrated how an increase of the field strength beyond a critical point in the over-barrier region leads to a crossing between the ionization rates of the $1b_1$ and $1b_2$ orbitals.

For the $3a_1$ MO, the orientation of the external field was chosen in two directions, that is the dc field pointing away or towards the oxygen atom fixed at the origin. The relationship of the resonance parameters (position and width) to the neighbouring valence orbitals $1b_1$ and $1b_2$ was explored. Interestingly, the $3a_1$ orbital was found to ionize more easily than $1b_1$ or $1b_2$ irrespective of the field direction along $\hat{z}$.

These calculations should serve as motivation for further studies of molecular orbitals of water using more sophisticated wave functions. It would be interesting to extend this work to deal with laser fields for practical applications. For the hydrogen molecular ion this was done using Floquet theory [63], where some parallels were found between monochromatic AC and the DC cases. Experimental observations of strong-field ionization of water vapour are available for short, intense laser pulses [98, 99]. One needs to solve the TDSE for realistic simulations of these [100, 101].

Partial-wave approach with a CAP

Ionization of H_2O valence orbitals exposed to an external dc field has been addressed from an alternative perspective as well. The hydrogen components of a three-centre model potential introduced in a study of ion collisions with water molecules [73] were expressed as a partial-wave expansion in a basis of spherical harmonics [72] truncated at $l = l_{max}$. This representation of the model potential in terms of partial waves resulted in a system of radial equations of dimensions proportional to the size of the expansion. The system of coupled ordinary differential equations for the different (l, m) channels was solved numerically by implementing a finite-element *Mathematica* method. The precision of the calculations was modified accordingly as the number l_{max} increased and, consequently, the number of (l, m) channels.

The field-free problem was addressed and orbital energies for the valence MOs were obtained

for increasing sizes of the partial-wave expansion. In a comparison with the solutions for the model potential as quoted in a Gaussian orbital basis approach [4], the partial-wave expansion results were found to approximate the eigenvalues from above. The outermost orbital $1b_1$, with its density perpendicular to the molecular plane and little overlap with the hydrogen atoms, indicated a fast convergence with l_{max}. On the other hand, for the more deeply bound MO $1b_2$, with a considerable amount of electron density along each O$-$H bond, convergence with l_{max} was noticeably slower. Comparison with the eigenvalues obtained for an exchange-only OPM calculation [5] was shown as well.

The complex-valued resonance energies were computed by including a quadratic CAP that was turned on at a distance such that the effective potential had reached its simple asymptotic form. The eigenvalues were determined by implementing the Riss-Meyer correction scheme [37]. Comparison of the calculated dc shifts and decay rates with the previous results based on a single-centre SCF orbital dependent effective potential [44, 45], for which azimuthal symmetry was assumed, points to the fact that the partial-wave expansion of the model potential has more geometric flexibility in the resonance solution, and therefore shows more prominent features in the behaviour of dc shift and decay rate Γ as a function of the field strength and field orientation.

6.2   Above threshold ionization for laser-atom interactions

We have investigated the phenomenon of ATI for a model-He atom in the presence of a strong linearly polarized laser field. A generalization of the Keldysh formalism of SFA [19], in which rescattering of an electron with its parent ion is considered, has been explored in the limiting case of a zero-range potential. A systematic study of the numerical convergence of the ATI spectrum has been carried out by evaluating the compact expression for ionization of an atom into a scattering state [21] with asymptotic momentum **p**. Several parameters associated with the numerical precision of the calculation, such as the working precision, were tuned up in order to reduce the error when evaluating the relevant quadrature.

In addition to the numerical evaluation of the compact expression for the transition amplitude, an alternative analysis based on the concept of quantum paths [20] was implemented. This approach permitted to generate the ATI spectrum by means of a saddle-point approximation in which a coherent sum over a reduced number of complex trajectories was carried out. For the

case of direct electrons, a total of two complex trajectories was sufficient to generate an ATI spectrum that converged to the Keldysh model. On the other hand, convergence of the ATI spectrum including electron rescattering proved to be a more intricate problem.

The zero-range potential model was implemented to generate an approximated strong-field ionization spectrum for the $1b_1$ and $1b_2$ molecular orbitals of H_2O. Each molecular orbital was treated as an independent spherically symmetric orbital with a binding energy corresponding to the eigenvalue of the field-free problem with a one-centre SCF effective potential. This approach is by no means an attempt to provide a realistic picture of the H_2O molecule subjected to an intense laser field. However, it could serve as reference to future works that focus on the convergence of the ionization spectrum.

Bibliography

[1] Roberto Moccia. One-center Basis Set SCF MO's. iii. H_2O, H_2S, and HCl. *The Journal of Chemical Physics*, 40(8):2186–2192, 1964. vi, 2, 4, 5, 8, 9, 10, 11, 15, 16, 17, 18, 19, 23, 27, 29, 30, 32, 39, 40, 89

[2] D. A. Telnov. DC Stark effect in a hydrogen atom via Sturmian expansions. *Journal of Physics B: Atomic, Molecular and Optical Physics*, 22(14):L399–L404, 1989. vii, 20, 22, 36, 38, 39

[3] V V Kolosov. A hydrogen atom in a strong electric field. *Journal of Physics B: Atomic and Molecular Physics*, 20(11):2359–2367, 1987. vii, 38, 39

[4] L. F. Errea, Clara Illescas, L. Méndez, I. Rabadán, and J. Suárez. Lattice description of electron loss in high-energy H^+ + H_2O collisions. *Chemical Physics*, 462:17 – 22, 2015. Inelastic Processes in Atomic, Molecular and Chemical Physics. viii, 30, 31, 43, 44, 45, 91

[5] Andreas Heßelmann, Andreas W. Götz, Fabio Della Sala, and Andreas Görling. Numerically stable optimized effective potential method with balanced gaussian basis sets. *The Journal of Chemical Physics*, 127(5):054102, 2007. viii, 44, 45, 91

[6] M. Protopapas, C. H Keitel, and P. L. Knight. Atomic physics with super-high intensity lasers. *Reports on Progress in Physics*, 60(4):389–486, 1997. viii, 50, 52

[7] G. G. Paulus, W. Nicklich, Huale Xu, P. Lambropoulos, and H. Walther. Plateau in above threshold ionization spectra. *Phys. Rev. Lett.*, 72:2851–2854, 1994. viii, 3, 51, 53, 55, 62, 80, 81

[8] Richard Kopold. *Atomare Ionisationsdynamik in starken Laserfeldern*. PhD thesis, Institut für Theoretische Physik, Technische Universität München, 2001. xi, 50, 69, 74, 77, 78, 86, 87

[9] Mitsuko Murakami, Tom Kirchner, Marko Horbatsch, and Hans Jürgen Lüdde. Fragmentation of water molecules by proton impact: The role of multiple electron processes. *Phys. Rev. A*, 85:052713, 2012. 1

[10] L. F. Errea, Clara Illescas, L. Méndez, and I. Rabadán. Ionization of water molecules by proton impact: Two nonperturbative studies of the electron-emission spectra. *Phys. Rev. A*, 87:032709, 2013. 1

[11] Thomas-C. Jagau. Coupled-cluster treatment of molecular strong-field ionization. *The Journal of Chemical Physics*, 148(20), 2018. 1, 3, 47

[12] Lars Bojer Madsen, Frank Jensen, Oleg I. Tolstikhin, and Toru Morishita. Application of the weak-field asymptotic theory to tunneling ionization of H_2O. *Phys. Rev. A*, 89:033412, 2014. 1

[13] Pascal Krause and H. Bernhard Schlegel. Angle-dependent ionization of hydrides ah(n) calculated by time-dependent configuration interaction with an absorbing potential. *The Journal of Physical Chemistry A*, 119(40):10212–10220, 2015. 1

[14] Song-Feng Zhao, Junliang Xu, Cheng Jin, Anh-Thu Le, and C. D. Lin. Effect of orbital symmetry on the orientation dependence of strong field tunnelling ionization of nonlinear polyatomic molecules. *Journal of Physics B: Atomic, Molecular and Optical Physics*, 44 (3), 2011. 1

[15] Simon Petretti, Alejandro Saenz, Alberto Castro, and Piero Decleva. Water molecules in ultrashort intense laser fields. *Chemical Physics*, 414:45–52, 2013. 1

[16] P. Agostini, F. Fabre, G. Mainfray, G. Petite, and N. K. Rahman. Free-Free Transitions Following Six-Photon Ionization of Xenon Atoms. *Phys. Rev. Lett.*, 42:1127–1130, 1979. 1, 49

[17] W. Becker, S. P. Goreslavski, D. B. Milošević, and G. G. Paulus. The plateau in above-threshold ionization: the keystone of rescattering physics. *Journal of Physics B: Atomic, Molecular and Optical Physics*, 51(16):162002, 2018. 1, 55, 80, 82

[18] W. Becker, F. Grasbon, R. Kopold, D.B. Milošević, G.G. Paulus, and H. Walther. *Above-Threshold Ionization: From Classical Features to Quantum Effects*, volume 48 of *Advances In Atomic, Molecular, and Optical Physics*. Academic Press, 2002. 1, 49, 55, 71, 72, 74

[19] L. V. Keldysh. Ionization in the field of a strong electromagnetic wave. *Soviet Physics JETP*, 20:1307–1314, 1965. 2, 3, 49, 50, 51, 55, 71, 91

[20] R. Kopold, W. Becker, and M. Kleber. Quantum path analysis of high-order above-threshold ionization. *Optics Communications*, 179(1):39 – 50, 2000. 2, 4, 69, 70, 71, 72, 73, 74, 81, 88, 91

[21] A. Lohr, M. Kleber, R. Kopold, and W. Becker. Above-threshold ionization in the tunneling regime. *Phys. Rev. A*, 55:R4003–R4006, 1997. 2, 4, 50, 52, 54, 55, 56, 62, 64, 69, 70, 91

[22] Frank O. Ellison and Harrison Shull. Molecular Calculations. I. LCAO MO Self-Consistent Field Treatment of the Ground State of H_2O. *The Journal of Chemical Physics*, 23(12): 2348–2357, 1955. 2, 8, 9

[23] C. C. J. Roothaan. New Developments in Molecular Orbital Theory. *Rev. Mod. Phys.*, 23: 69–89, Apr 1951. 2, 5, 6, 7, 8, 15

[24] S. F. Boys, G. B. Cook, C. M. Reeves, and I. Shavitt. Automatic Fundamental Calculations of Molecular Structure. *Nature*, 178(4544):1207–1209, 1956. 2, 11

[25] R. McWeeny and K. A. Ohno. A quantum-mechanical study of the water molecule. *Proc. R. Soc. Lond.*, A255(1282):367–381, 1960. 2, 11

[26] Soe Aung, Russell M. Pitzer, and Sunney I. Chan. Approximate Hartree-Fock Wavefunctions, One-Electron Properties, and Electronic Structure of the Water Molecule. *The Journal of Chemical Physics*, 49(5):2071–2080, 1968. 2, 5, 11, 15

[27] Russell M. Pitzer and Donald P. Merrifield. Minimum Basis Wavefunctions for Water. *The Journal of Chemical Physics*, 52(9):4782–4787, 1970. 2, 5, 8, 11, 15

[28] J. W. Moskowitz and M. C. Harrison. Gaussian Wavefunctions for the $10-$Electron Systems. III. OH^-, H_2O, H_3O^+. *The Journal of Chemical Physics*, 43(10):3550–3555, 1965. 2, 11

[29] D. Neumann and J. W. Moskowitz. One-Electron Properties of Near-Hartree-Fock Wavefunctions. i. water. *The Journal of Chemical Physics*, 49(5):2056–2070, 1968. 2, 8

[30] E. L. Albasiny and J. R. A. Cooper. A one-centre S.C.F. wave function for the methane molecule. *Molecular Physics*, 4(5):353–368, 1961. 2, 9

[31] Antony F. Saturno and Robert G. Parr. A One-Center Wave Function for the Methane Molecule. *The Journal of Chemical Physics*, 33(1):22–27, 1960. 2, 9

[32] J. S. Parker, G. S. J. Armstrong, M. Boca, and K. T. Taylor. From the UV to the static-field limit: rates and scaling laws of intense-field ionization of helium. *Journal of Physics B: Atomic, Molecular and Optical Physics*, 42(13), 2009. 2

[33] J. S. Parker, K. J. Meharg, G. A. McKenna, and K. T. Taylor. Single-ionization of helium at Ti: Sapphire wavelengths: rates and scaling laws. *Journal of Physics B: Atomic, Molecular and Optical Physics*, 40(10):1729–1743, 2007. 2

[34] Armin Scrinzi, Michael Geissler, and Thomas Brabec. Ionization above the coulomb barrier. *Phys. Rev. Lett.*, 83:706–709, 1999. 2

[35] G. D. Purvis and R. J. Bartlett. A full coupled-cluster singles and doubles model: The inclusion of disconnected triples. *The Journal of Chemical Physics*, 76(4):1910–1918, 1982. 3

[36] B. Simon. Resonances in n-body quantum systems with dilatation analytic potentials and the foundations of time-dependent perturbation theory. *Ann. Math.*, 97:247–74, 1973. 3, 20

[37] U. V. Riss and H. D. Meyer. Calculation of resonance energies and widths using the complex absorbing potential method. *Journal of Physics B: Atomic, Molecular and Optical Physics*, 26(23):4503–4535, 1993. 3, 12, 14, 33, 34, 91

[38] Barry Simon. The definition of molecular resonance curves by the method of exterior complex scaling. *Physics Letters A*, 71(2):211 – 214, 1979. 3, 12, 14, 16, 20

[39] A. Scrinzi and N. Elander. A finite element implementation of exterior complex scaling for the accurate determination of resonance energies. *The Journal of Chemical Physics*, 98(5): 3866–3875, 1993. 3, 14, 20

[40] V. P. Majety and A. Scrinzi. Static field ionization rates for multi-electron atoms and small molecules. *Journal of Physics B: Atomic, Molecular and Optical Physics*, 48(24):245603, 2015. 3, 20, 25

[41] Pascal Krause, Jason A. Sonk, and H. Bernhard Schlegel. Strong field ionization rates simulated with time-dependent configuration interaction and an absorbing potential. *The Journal of Chemical Physics*, 140(17):174113, 2014. 3, 12

[42] Armin Scrinzi. Infinite-range exterior complex scaling as a perfect absorber in time-dependent problems. *Phys. Rev. A*, 81:053845, 2010. 3, 12, 14, 20, 29, 36

[43] F. He, C. Ruiz, and A. Becker. Absorbing boundaries in numerical solutions of the time-dependent Schrödinger equation on a grid using exterior complex scaling. *Phys. Rev. A*, 75:053407, 2007. 3, 20

[44] Susana Arias Laso and Marko Horbatsch. Calculation of stark resonance parameters for valence orbitals of the water molecule. *Phys. Rev. A*, 94:053413, 2016. 3, 13, 16, 17, 22, 27, 30, 46, 90, 91

[45] Susana Arias Laso and Marko Horbatsch. Stark resonance parameters for the $3a_1$ orbital of the water molecule. *Journal of Physics B: Atomic, Molecular and Optical Physics*, 50 (22):225001, 2017. 3, 13, 27, 30, 47, 90, 91

[46] W. Becker, A. Lohr, and M. Kleber. Effects of rescattering on above-threshold ionization. *Journal of Physics B: Atomic, Molecular and Optical Physics*, 27(14):L325–L332, jul 1994. 4, 55, 81

[47] G. G. Paulus, W. Becker, W. Nicklich, and H. Walther. Rescattering effects in above-threshold ionization: a classical model. *Journal of Physics B: Atomic, Molecular and OpticalPhysics*, 27(21):L703–L708, 1994. 4, 62, 81

[48] J Z Kaminski and F Ehlotzky. Relation between sidelobes and coulomb corrections in high-order above-threshold ionization. *Journal of Physics B: Atomic, Molecular and Optical Physics*, 30(1):69–76, 1997. 4, 49

[49] R. P. Feynman. Space-time approach to non-relativistic quantum mechanics. *Rev. Mod. Phys.*, 20:367 – 387, 1948. 4, 69, 72

[50] P. Salières, B. Carré, L. Le. Déroff, G. G. Paulus F. Grasbon, H. Walther, R. Kopold, W. Becker, D. B. Milosevic, A. Sanpera, and M. Lewenstein. Feynman's Path Integral Approach for Intense-Laser-Atom Interactions. *Science*, 292:902, 2001. 4, 70

[51] Roberto Moccia. One-center Basis Set SCF MO's. i. HF, CH_4, and SiH_4. *The Journal of Chemical Physics*, 40(8):2164–2176, 1964. 5, 8, 9, 10, 15, 27

[52] Ira N. Levine. *Quantum Chemistry*. Pearson, 2014. ISBN 978-0-321-80345-0. 7, 8

[53] James F. Harrison. Some One-Electron Properties of H_2O and NH_3. *The Journal of Chemical Physics*, 47(8):2990–2996, 1967. 8

[54] Thom. H. Dunning, Russell M. Pitzer, and Soe Aung. Near Hartree-Fock Calculations on the Ground State of the Water Molecule: Energies, Ionization Potentials, Geometry, Force Constants, and one-Electron Properties. *The Journal of Chemical Physics*, 57(12): 5044–5051, 1972. 8

[55] Roberto Moccia. One-center Basis Set SCF MO's. ii. NH_3, NH_4^+, PH_3, PH_4^+. *The Journal of Chemical Physics*, 40(8):2176–2185, 1964. 8, 9, 10, 15

[56] E. Clementi and A. D. McLean. SCF-LCAO-MO Wave Functions for the Bifluoride Ion. *The Journal of Chemical Physics*, 36(3):745–749, 1962. 9

[57] C. Roetti and E. Clementi. Simple basis sets for molecular wavefunctions containing atoms from $z = 2$ to $z = 54$. *The Journal of Chemical Physics*, 60(12):4725–4729, 1974. 9

[58] C. F. Bunge, J. A. Barrientos, and A. V. Bunge. Roothaan-Hartree-Fock Ground-State Atomic Wave-Functions: Slater-Type Orbital Expansions and Expectation Values for Z $=$ $2 - 54$. *Atomic Data and Nuclear Data Tables*, 53(1):113–162, 1993. 9

[59] G. P. Arrighini, M. Maestro, and R. Moccia. Electric polarizability of polyatomic molecules. *Chemical Physics Letters*, 1(5):242–245, 1967. 11

[60] N. Moiseyev. *Non-Hermitian Quantum Mechanics*. Cambridge University Press, 2011. ISBN 978-0-521-88972-8. 12, 13, 29

[61] R. Lefebvre, M. Sindelka, and N. Moiseyev. Resonance positions and lifetimes for flexible complex absorbing potentials. *Phys. Rev. A*, 72:052704, 2005. 14

[62] Ts. Tsogbayar and M. M Horbatsch. Calculation of Stark resonance parameters for the hydrogen molecular ion in a static electric field. *Journal of Physics B: Atomic, Molecular and Optical Physics*, 46(8):085004, 2013. 14

[63] Ts. Tsogbayar and M. M Horbatsch. Floquet calculations of ionization of the molecular hydrogen ion by intense laser fields in the low-frequency limit. *Journal of Physics B: Atomic, Molecular and Optical Physics*, 46(24):245005, 2013. 14, 25, 90

[64] C C Montanari and J E Miraglia. Neonization method for stopping, mean excitation energy, straggling, and for total and differential ionization cross sections of CH_4, NH_3, H_2O and FH by impact of heavy projectiles. *Journal of Physics B: Atomic, Molecular and Optical Physics*, 47(1):015201, dec 2013. 15

[65] H. Hafied, A. Eschenbrenner, C. Champion, M.F. Ruiz-López, C. Dal Cappello, I. Charpentier, and P.A. Hervieux. Electron momentum spectroscopy of the valence orbitals of the water molecule in gas and liquid phase: A comparative study. *Chemical Physics Letters*, 439(1):55–59, 2007. 15

[66] Photoelectron Spectroscopy, jan 13 2020. URL https://chem.libretexts.org/@go/page/13473. [Online; accessed 2021-12-21]. 15

[67] Richard Latter. Atomic Energy Levels for the Thomas-Fermi and Thomas-Fermi-Dirac Potential. *Phys. Rev.*, 99:510–519, 1955. 17, 27, 28

[68] J. Aguilar and J. M. Combes. A class of analytic perturbations for one-body Schrödinger Hamiltonians. *Commun. Math. Phys.*, 22(4):269–79, 1971. 20

[69] E. Baslev and J. M. Combes. Spectral Properties of Many-body Schrödinger Operators with Dilatation-analytic Interactions. *Commun. Math. Phys.*, 22(4):280–94, 1971. 20

[70] Liang Tao, W. Vanroose, B. Reps, T. N. Rescigno, and C. W. McCurdy. Long-time solution of the time-dependent Schrödinger equation for an atom in an electromagnetic field using complex coordinate contours. *Phys. Rev. A*, 80:063419, 2009. 20

[71] C. J. Joachain, M. Dörr, and N. Kylstra. High-Intensity Laser-Atom Physics. volume 42 of *Advances In Atomic, Molecular, and Optical Physics*, pages 225 – 286. Academic Press, 2000. 25, 50

[72] Patrik Pirkola and Marko Horbatsch. Partial-wave approach to the Stark resonance problem of the water molecule. *Phys. Rev. A*, 105:032814, 2022. 30, 31, 32, 33, 90

[73] Clara Illescas, L. F. Errea, L. Méndez, B. Pons, I. Rabadán, and A. Riera. Classical treatment of ion-H_2O collisions with a three-center model potential. *Phys. Rev. A*, 83: 052704, 2011. 30, 37, 90

[74] N. Rom, N. Lipkin, and N. Moiseyev. Optical potentials by the complex coordinate method. *Chemical Physics*, 151(2):199–204, 1991. 36

[75] N. Moiseyev. Derivations of universal exact complex absorption potentials by the generalized complex coordinate method. *Journal of Physics B: Atomic, Molecular and Optical Physics*, 31(7):1431–1441, 1998. 36

[76] Boris N. Plakhutin. Koopmans' theorem in the Hartree-Fock method. General formulation. *The Journal of Chemical Physics*, 148(9), 2018. 44

[77] Takao Tsuneda, Jong-Won Song, Satoshi Suzuki, and Kimihiko Hirao. On Koopmans' theorem in density functional theory. *The Journal of Chemical Physics*, 133(17), 2010. 44

[78] M. J. Nandor, M. A. Walker, L. D. Van Woerkom, and H. G. Muller. Detailed comparison of above-threshold-ionization spectra from accurate numerical integrations and high-resolution measurements. *Phys. Rev. A*, 60:R1771–R1774, 1999. 49

[79] Armin Scrinzi, Michael Geissler, and Thomas Brabec. Ionization above the coulomb barrier. *Phys. Rev. Lett.*, 83:706–709, 1999. 49

[80] C.J. Joachain, M. Dörr, and N. Kylstra. *High-Intensity Laser-Atom Physics*, volume 42 of *Advances In Atomic, Molecular, and Optical Physics*. Academic Press, 2000. 49

[81] F. H. M. Faisal. Collision of electrons with laser photons in a background potential. *Journal of Physics B: Atomic and Molecular Physics*, 6(11):L312–L315, 1973. 49

[82] Howard R. Reiss. Effect of an intense electromagnetic field on a weakly bound system. *Phys. Rev. A*, 22:1786–1813, 1980. 49

[83] G. Petite, P. Agostini, and H. G. Muller. Intensity dependence of non-perturbative above-threshold ionization spectra: experimental study. *Journal of Physics B: Atomic, Molecular and Optical Physics*, 21(24):4097–4105, 1988. 50

[84] B. Walker, B. Sheehy, L. F. DiMauro, P. Agostini, K. J. Schafer, and K. C. Kulander. Precision Measurement of Strong Field Double Ionization of Helium. *Phys. Rev. Lett.*, 73: 1227–1230, Aug 1994. 51

[85] B. Walker, B. Sheehy, K. C. Kulander, and L. F. DiMauro. Elastic Rescattering in the Strong Field Tunneling Limit. *Phys. Rev. Lett.*, 77:5031–5034, 1996. 51, 55, 80

[86] P. B. Corkum. Plasma perspective on strong field multiphoton ionization. *Phys. Rev. Lett.*, 71:1994–1997, 1993. 52

[87] M. Lewenstein, Ph. Balcou, M. Yu. Ivanov, Anne L'Huillier, and P. B. Corkum. Theory of high-harmonic generation by low-frequency laser fields. *Phys. Rev. A*, 49:2117–2132, 1994. 52, 69, 70

[88] D.B. Milošević, G. G Paulus, D. Bauer, and W. Becker. Above-threshold ionization by few-cycle pulses. *Journal of Physics B: Atomic, Molecular and Optical Physics*, 39(14): R203–R262, 2006. 52, 71, 72

[89] Zi Jian Long and Wing-Ki Liu. Keldysh theory of strong field ionization. *Can. J. Phys.*, 88:227–245, 2010. 54, 71

[90] W. Becker, A. Lohr, M. Kleber, and M. Lewenstein. A unified theory of high-harmonic generation: Application to polarization properties of the harmonics. *Phys. Rev. A*, 56: 645–656, 1997. 54

[91] M. Kleber. Exact solutions for time-dependent phenomena in quantum mechanics. *Physics Reports*, 236(6):331–393, 1994. ISSN 0370-1573. 55

[92] W. Becker, S. Long, and J. K. McIver. Short-range potential model for multiphoton detachment of the H$^-$ ion. *Phys. Rev. A*, 42:4416–4419, Oct 1990. 55

[93] S. V. Borzunov, M. V. Frolov, M. Yu. Ivanov, N. L. Manakov, S. S. Marmo, and Anthony F. Starace. Zero-range-potential model for strong-field molecular processes: Dynamic polarizability and photodetachment cross section. *Phys. Rev. A*, 88:033410, 2013. 55

[94] M. Lewenstein, K. C. Kulander, K. J. Schafer, and P. H. Bucksbaum. Rings in above-threshold ionization: A quasiclassical analysis. *Phys. Rev. A*, 51:1495–1507, 1995. 70, 72, 73

[95] W. Becker, R. R. Schlicher, and M. O. Scully. Final-state effects in above-threshold ionization. *Journal of Physics B: Atomic and Molecular Physics*, 19(22):L785–L792, nov 1986. 70

[96] R. Kopold, D. B. Milošević, and W. Becker. Rescattering Processes for Elliptical Polarization: A Quantum Trajectory Analysis. *Phys. Rev. Lett.*, 84:3831–3834, 2000. 70

[97] A. M. Dykhne. Quantum Transitions in the Adiabatic Approximation. *Soviet Physics JETP*, 11:411–415, 1960. 74

[98] D. Mathur, F. A. Rajgara, A. K. Dharmadhikari, and J. A. Dharmadhikari. Strong-field ionization of water by intense few-cycle laser pulses. *Phys. Rev. A*, 78:023414, 2008. 90

[99] M. Wilke, R. Al-Obaidi, A. Moguilevski, A. Kothe, N. Engel, J. Metje, I. Yu Kiyan, and E. F. Aziz. Laser-assisted electron scattering in strong-field ionization of dense water vapor by ultrashort laser pulses. *New Journal of Physics*, 16(083032), 2014. 90

[100] Joseph P. Farrell, Simon Petretti, Johann Förster, Brian K. McFarland, Limor S. Spector, Yulian V. Vanne, Piero Decleva, Philip H. Bucksbaum, Alejandro Saenz, and Markus Gühr. Strong field ionization to multiple electronic states in water. *Phys. Rev. Lett.*, 107:083001, 2011. 90

[101] Mirjam Falge, Volker Engel, and Manfred Lein. Vibrational-state and isotope dependence of high-order harmonic generation in water molecules. *Phys. Rev. A*, 81:023412, 2010. 90

Appendices

A Length gauge

This appendix introduces the length gauge, a commonly used gauge choice to describe laser-atom interactions.

The Hamiltonian for an electron in the presence of an external electromagnetic field described by the potentials $(\mathbf{A}, \phi)$ can be expressed as

$$H(t) = \frac{1}{2m}(\mathbf{p} - e\mathbf{A})^2 + V(\mathbf{r}) + e\phi, \tag{A.1}$$

where $\mathbf{p} = -i\hbar\nabla$, ∇ is the gradient operator, and $V(\mathbf{r})$ is the binding potential of the atom. In the presence of an electromagnetic field, the Hamiltonian is frequently decomposed as

$$H(t) = H_0 + H_I(t), \tag{A.2}$$

where the operator $H_0 = \mathbf{p}^2/2m + V(\mathbf{r})$ is known as the field-free Hamiltonian, while $H_I(t)$ describes the interaction of an otherwise free electron with the external field, and its form depends on the gauge employed. Within the long-wavelength approximation (LWA), or dipole approximation, which neglects the space dependence of the electric field and the vector potential, so that $\mathbf{E}(\mathbf{r}, t) \to \mathbf{E}(t)$ and $\mathbf{A}(\mathbf{r}, t) \to \mathbf{A}(t)$, one finds that the divergence of the vector potential vanishes $\nabla \cdot \mathbf{A} = 0$, and the interaction operator takes the form

$$H_I(t) = e\phi - \frac{e}{m}\mathbf{A} \cdot \mathbf{p} + \frac{e^2}{2m}\mathbf{A}^2 \tag{A.3}$$

A gauge transformation is defined as a change of the electromagnetic field potentials $(\mathbf{A}, \phi)$ and the wave function Ψ by the gauge function $\Lambda = \Lambda(\mathbf{r}, t)$ such that

$$\begin{aligned} \mathbf{A} \to \quad & \mathbf{A}' = \mathbf{A} + \nabla\Lambda \\ \phi \to \quad & \phi' = \phi - \frac{\partial}{\partial t}\Lambda \\ \Psi \to \quad & \Psi' = e^{-\frac{ie}{\hbar}\Lambda}\Psi \end{aligned} \tag{A.4}$$

This transformation leaves the physical fields $\mathbf{E}$ and $\mathbf{B}$ unaffected as well as the TDSE $i\hbar\frac{\partial}{\partial t}\Psi' = H(t)\Psi'$. The length gauge results from the transformation

$$\Lambda = -\mathbf{A}(t) \cdot \mathbf{r}, \tag{A.5}$$

which leads to

$$\begin{aligned} \mathbf{A}' &= 0 \\ \phi' &= \frac{\partial}{\partial t}\mathbf{A}(t) \cdot \mathbf{r} = -\mathbf{r} \cdot \mathbf{E}(t) \end{aligned} \tag{A.6}$$

for the vector and scalar potentials of the external laser field, respectively. In terms of the transformed potentials, the interaction operator takes the form $H_I = -e\mathbf{r} \cdot \mathbf{E}(t)$. Therefore, in the length gauge the TDSE becomes

$$i\hbar\frac{\partial}{\partial t}\Psi(\mathbf{r},t) = \ [H_0 - e\mathbf{r} \cdot \mathbf{E}(t)]\,\Psi(\mathbf{r},t). \tag{A.7}$$

In the case that the binding potential $V(\mathbf{r})$ is neglected, Eq. (A.7) takes the form

$$i\hbar\frac{\partial}{\partial t}\Psi(\mathbf{r},t) = \ \left[-\frac{1}{2m}\nabla^2 - e\mathbf{r} \cdot \mathbf{E}(t)\right]\Psi(\mathbf{r},t), \tag{A.8}$$

that corresponds to the TDSE for a free electron in a laser field. The solution of the TDSE (A.8) is the Volkov wave function $\Psi^V(\mathbf{r},t)$, which represents a plane wave describing an electron in a strong laser field.